Realization of a Fully Integrated Electronic-Photonic Sensor-Receiver Array for Endoscopic Ultrasound

Panagiotis Zarkos
Vladimir Stojanovic, Ed.

Electrical Engineering and Computer Sciences
University of California, Berkeley

Technical Report No. UCB/EECS-2023-35
http://www2.eecs.berkeley.edu/Pubs/TechRpts/2023/EECS-2023-35.html

May 1, 2023

Realization of a Fully Integrated Electronic-Photonic Sensor-Receiver Array for Endoscopic Ultrasound

by

Panagiotis Zarkos

A dissertation submitted in partial satisfaction of the

requirements for the degree of

Doctor of Philosophy

in

Engineering - Electrical Engineering and Computer Sciences

in the

Graduate Division

of the

University of California, Berkeley

Committee in charge:

Professor Vladimir Stojanović, Chair
Professor Ming Wu
Professor Costas Grigoropoulos

Fall 2021

Realization of a Fully Integrated Electronic-Photonic Sensor-Receiver Array for Endoscopic Ultrasound

Abstract

Realization of a Fully Integrated Electronic-Photonic Sensor-Receiver Array for Endoscopic Ultrasound

by

Panagiotis Zarkos

Doctor of Philosophy in Engineering - Electrical Engineering and Computer Sciences

University of California, Berkeley

Professor Vladimir Stojanović, Chair

Ultrasound imaging remains an indispensable tool in numerous medical disciplines ranging from oncology to cardiology and from dermatology to ophthalmology. Imagers employing piezoelectric and capacitive micromachined transducers have long been the golden standard when it comes to traditional ultrasonography procedures such as abdominal, pelvic or obstetric scans. However, when used in endoscopic, intravascular, and catheterized applications, traditional receiver implementations have demonstrated serious shortcomings in terms of power dissipation and achieved form factor.

The focus of this thesis is on the development and realization of an electronic-photonic ultrasound receiver system capable of tackling modern miniaturized endoscopic probe specifications. It begins with an overview of the existing electrical and optical ultrasound imaging technologies, which spotlights the need for an alternative approach to endoscopic ultrasound sensing and proposes a electronic-photonic array system based on micro-ring resonator (MRR) sensors as a promising candidate. Subsequently, the operating principle of MRR ultrasound sensing is presented, accompanied by theoretical analysis and finite element model (FEM) simulations of the transduction mechanisms. The developed theory is backed by proof-of-concept experimental results. The initial analysis is followed by the design and fabrication of a first-of-its-kind ultrasound receiver array on a silicon photonic chip with highly sensitive, micro-scale optical MRR sensors in its core. Such a system can be ultra-low power and size, ensuring safe operation inside the human body without sacrificing key system attributes, such as image resolution and system bandwidth. Configured in 2-D beamforming arrays of thousands of elements, these optical sensors, can perform real-time, 3-D imaging and pave the way towards miniaturized optical ultrasonic reception probes with form factors below 5mm^3, compliant to modern endoscopic probe specifications. After presenting measurement results of this electronic-photonic system-on-chip (EPSoC) prototype, the thesis discusses architectures that will further enhance the overall system sensitivity through the use of coherent detection and higher quality factor MRRs.

Η ζωή μας μια φορά μάς δίνεται.
Άπαξ, που λένε. Σαν μια μοναδική ευκαιρία.
Τουλάχιστον, μ'αυτήν την αυτόνομη μορφή της,
δεν πρόκειται να ξαναϋπάρξουμε ποτέ.
Και μεις τί την κάνουμε, ρε;
Αντί να τη ζήσουμε; Τί την κάνουμε;

Την σέρνουμε από δω και από κει δολοφονώντας την·
οργανωμένη κοινωνία, οργανωμένες ανθρώπινες σχέσεις.
Μα αφού είναι οργανωμένες, πώς είναι σχέσεις;
Σχέση σημαίνει συνάντηση, σημαίνει έκπληξη,
σημαίνει γέννα συναισθήματος.
Πώς να οργανώσεις τα συναισθήματα;

Έτσι, μ' αυτήν την κωλοεφεύρεση που τη λένε ρολόι,
σπρώχνουμε τις ώρες και τις μέρες μας,
σα να είναι βάρος. Και μάς είναι βάρος.
Γιατί δε ζούμε... κατάλαβες;

[Χρόνης Μίσσιος]

Contents

List of Figures

List of Tables

Acknowledgements

I would first like to thank my advisor, Professor Vladimir Stojanović. Not only has he suggested a most intriguing PhD topic and provided invaluable technical guidance on it, but more importantly, he has shown great patience and unweathering support, especially during my initial research efforts. Through his advice I have learned to divide and conquer problems in a way that reveals the true engineering challenges, and I have grown both scientifically and personally. His positive attitude, dedication, and perseverance in the pursuit of his goals and beliefs have always motivated me to keep pushing and they have in part "willed" this first-of-its-kind system to work. Being surrounded by his radiant personality and working with him for the past six and a half years has been a true privilege.

Many thanks also go to my undergraduate advisor, Prof. Paul Sotiriadis who has helped me develop a strong circuit intuition, exposed me to research from an undergraduate level, provided me the opportunity to teach as an undergraduate student, and enabled my quest for a graduate career in the U.S. Additionally, I would like to express my gratitude to Dr. Iason Vassiliou for his technical guidance in my diploma thesis, his support of my graduate school applications, and for handy tips into the Berkeley grad school life.

I would also like to thank Professors Ming Wu, Costas Grigoropoulos, and Ali Niknejad for serving in my dissertation and qualifying exam committees, and for their very helpful and valuable feedback.

During my PhD career, I have been extremely lucky to be part of the Integrated Systems Group family. Embarking on journeys to build complex silicon-photonics systems, most of which have previously existed purely as vague ideas in Vladimir's head the entire group has been armed with infinite amounts of scientific optimism and creative foolishness. I would like to deeply thank each member of ISG for nurturing a culture of community, camaraderie and work ethic that has allowed us to fulfill our unrealistic goals. More specifically, I would like to thank: Sidney Buchbinder for being the most self-less lab mate one could wish for, always offering remarkable insights, vast knowledge, and almost single-handedly managing the entire group infrastructure, Christos Adamopoulos for countless technical discussions and for co-designing the sensing unit of our graduation chip, Sajjad Moazeni for introducing me to the groups' digital flow, Taehwan Kim for multiple PLL and phase noise discussions, Pavan Bhargava for his unparalleled background in diverse aspects of silicon photonic systems, Nandish Mehta for sharing his analog circuit design intuition, Krishna Settaluri for his passionate grad-life advice, Bozhi Yin, and Daniel Kramnik for their fresh perspective and

zeal, Rozhan Rabbani for her kindness, Erik Anderson for his cool demeanor, and Sunjin Choi for his enthusiasm. Of course, my testing comrades could not be missing from this list: I would like to particularly thank Olivia Hsu for the initial push in the proof-of-concept measurements, Sarika Madhvapathy for her help with the measurements for VLSI and the bravery to carry the project forward into the future, and Jake Whinnery for the design and 3-D printing of the water tank.

At this point, I would like to thank Professor Gireeja Ranade, for presenting me with the opportunity to teach EE 16A, the Intro to Electrical Engineering course as an instructor for a full semester, and for her great mentoring during that period. Her commitment to student well-being, attention to detail, and passion for teaching have set a remarkable example for me. Teaching at Berkeley has helped me evolve as a researcher and as a person and has been a life-altering experience. I would like to take a moment and thank the people that have taught with me for offering such diverse perspectives and for their will to self-sacrifice: Urmita Sikder, Grace Kuo, Moses Won, Seiya Ono, Sam Chaim-Weismann, Leyla Kabuli, Amanda Jackson, Sarika Madhvapathy, Miyuki Weldon, Raghav Gupta, Dahlia Saba, and many more.

Also, many thanks should go to the people that tirelessly worked to ensure the Berkeley Wireless Research Center run smoothly on an every-day basis during my time there: Candy Corpus, James Dunn, Jessica Bravo, Erin Hancock, Jeff Lee, Fred Burghard and so many more.

Additionally, I would like to acknowledge the Onassis Foundation for financially supporting me through the final year of my PhD.

On a more personal level, there are multiple people that have made life easier, exciting, and special during all these years in the Bay Area. I would like to thank Katerina Papadopoulou, for making me feel like a sister has got my back from the first moment I landed in Berkeley, as well as showing me all the ropes and cool places in the area; Fotis Iliopoulos for being a beacon of logic, wisdom and positive energy, and for sharing my passion for chess, Georgios Patsakis for having a heart of gold, always cheering me up or accompanying me in a midnight run; Georgios Moschidis for his valuable advice and encouragement, for being a role model, and my partner in crime during the last year in Berkeley; and Leo Cunha for being the best roommate I could ask for and a true friend, listening to numerous problems and complains over the years. Many other people have supported me in various ways throughout these long six and a half years and I would like to mention here: Vrettos Moulos, Evangelos Vrettos, Christos Bakalis, and Stavros Karagiannopoulos. Especially and separately, I wish to thank Anna Giannakou for teaching me in practice that there is more to graduate student life than endless work: travelling and exploring with her is a part of my grad-school time that I cherish. Also, I want to thank her for believing in me in times I did not, for caring about me, and for propelling me forwards through multiple hardships; she will always have my love and appreciation.

To my beloved friends across the ocean who have kept encouraging me non-stop, I am forever indebted, for they have been my compass, reminding me to remain true to myself and not drift astray in the havoc of research assignments, instilling in me moral values,

and helping me shape an attitude towards life that is far more important than any type of academic achievement. I feel very proud and privileged for their friendship, and extremely comforted in the knowledge that they will always have my back. Even though I could write multiple pages for each of them, etiquette and common courtesy dictate that I keep it short. Specifically, I wish to thank 4 people whose friendship spans over two entire decades: Iason Bassiakos for the correspondence both written and electronic – his inherent kindness, interest and compassion have always managed to strengthen me whenever I was disheartened; Alexis Koukias for maintaining and sharing the healthiest life perspective and attitude, and for bringing me back to order and balance at the most crucial times; Iasonas Gousetis for being my mate in the hopeless search of happiness and romance, and for lately reflecting many of my deepest thoughts through his powerful lyrics; Konstantinos Anagnostopoulos for assisting me to put my scattered thoughts in order with his infallible logic and for checking in on me the most frequently of all. Furthermore, I wish to thank Ahmed Mohammed for his glowing smile, Nikos Giatras for his limitless energy and humor, George Koutsoukos for his sharpness of mind and wishes, Angeliki Zeri for her genuine empathy, Angeliki Choriati for being the only one that actually visited, and Tasos Hariatis for being the best, most loyal center in a team I almost coached. Each, and every one of them has been truly special. Last, but not least, I want to thank Argyro Plevri for she has helped me much more than I have let her know during the last semester of this journey. Her unique gaze combined with her tender yet passionate character have filled me with joy and have greatly motivated me to wrap up this chapter of my life so that I can start a new one.

Closing this rather long acknowledgements section, I wish to thank my family. My uncle Spyros for introducing me to the world of chess, physics, and logic, and my aunt Olga for surrounding my summers with her warm personality and smile. Lastly, I want to thank my parents who have time and time again sacrificed multiple aspects of their personal life and happiness to ensure that I get the highest quality of education: my father George, for his faith in me, for caring and supporting me every step of the way and my mother Katerina for her constant anxiety, her thoughtfulness, and her boundless, unconditional love. This thesis is dedicated to them.

Chapter 1

Introduction

Heart disease and cancer are the leading causes of death, tolling for more than a million deaths in the US alone in 2017 [1]. Being low-cost and minimally invasive, high quality ultrasound imaging systems have been an indispensable tool in both cardiology and oncology. They are heavily used in the timely diagnosis and assessment of both heart diseases and numerous tumors, with very successful and frequent application in stenting operations [2] and breast tumor detection [3, 4], the second leading cause of death for women worldwide [5]. Additionally, during the outbreak of the COVID-19 pandemic, point-of-care lung ultrasound has resurfaced as a viable means of monitoring patients in self-isolation [6, 7, 8].

As we enter the era of personalized treatment in medicine, the need to engineer portable diagnostic systems that can enable easily accessible, high fidelity multi-organ screening at a low cost closely follows. The next generation of ultrasonic point-of-care (POC) diagnostic devices includes a variety of systems, from catheterized ultrasound sensors that monitor the cardiac and vascular functions to compact, high resolution, photoacoustic mammoscopes and imagers. A state-of-the-art point of care ultrasound imaging device [9, 10] is shown in action in Fig. 1.1a, while Fig. 1.1b shows a photoacoustic image of the human intestine, and Fig. 1.1c illustrates one of the most common endoscopic ultrasound applications, transesophageal echocardiography.

1.1 Motivation and Research Vision

Looking specifically into endoscopes targeting intravascular and catheterized types of applications there still is an unmet need for real-time, high resolution, volumetric ultrasonic images that would greatly enhance the physician's comprehension of the patient's physiology in both interventional and diagnostic settings. Intravascular ultrasound (IVUS)-guided stent placement [13], and transesophageal echocardiography (TEE) [14], constitute characteristic paradigms in which 3-D endoscopic ultrasound imaging can aid during both, the time of surgery, and the first steps of diagnosis or therapy of cardiovascular diseases. At the same time endoscopes based on traditional ultrasonic imagers employing piezoelectric

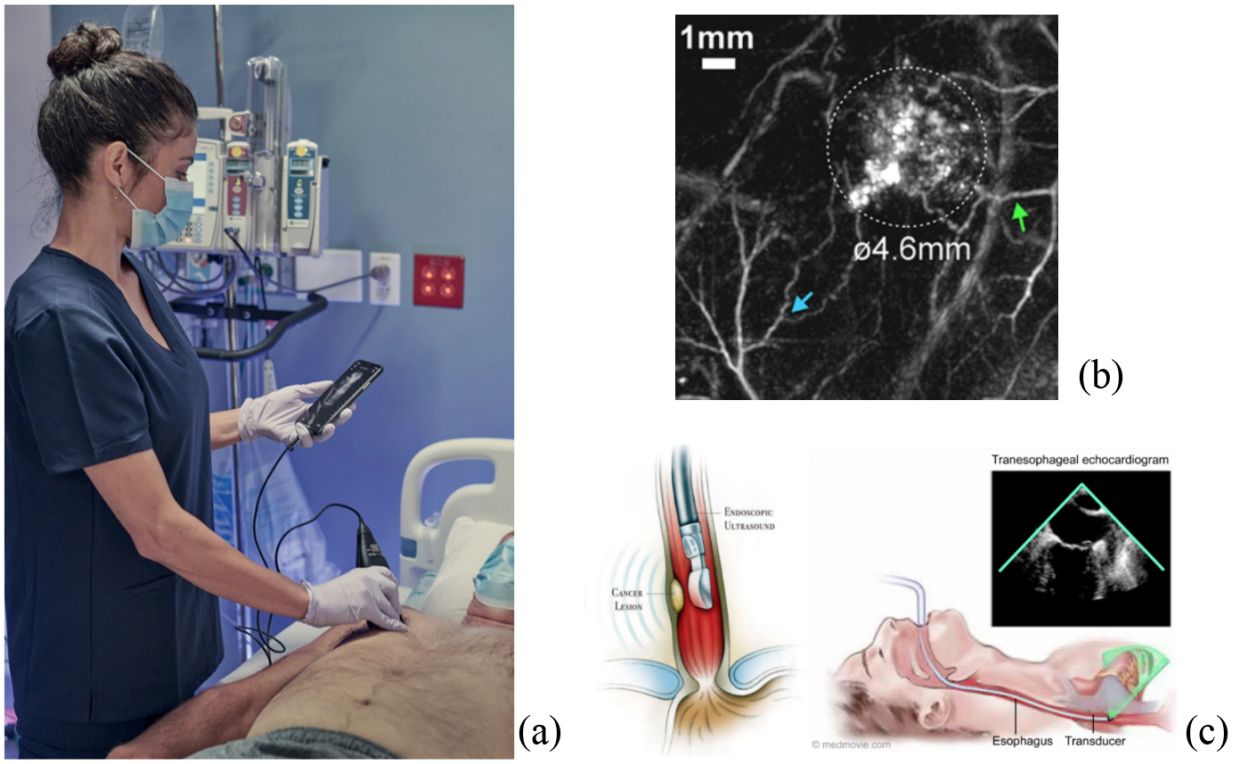

Figure 1.1: (a) POC Ultrasound: Handheld ultrasound imager [10], (b) Photoacoustic Ultrasound: Image of human intestinal tumor and surrounding vasculature [11], (c) Endoscopic Ultrasound: Transesophageal echocardiography [12].

,

and capacitive micromachined transducers (PMUTs and CMUTs) have demonstrated serious shortcomings in terms of power dissipation, achieved form factor, as will be explained in detail in Chapter 2.

Thus, new, alternative approaches to ultrasound sensing are being sought, with optical transducers being among the most promising candidates. The high sensitivity and low quiescent power consumption of both interferometric [15, 16, 17] and MRR based [18, 19, 20] sensors make these optical devices ideally suited for 3-D endoscopes, where power and area minimization are crucial. Choosing MRRs over interferometers primarily due to their scalability to large arrays, compact form-factor and capability of efficient resonant wavelength control, this research focuses on building an ultrasonic receiver with a beamforming matrix of optical MRR transducers in its core.

This first of its kind photonic imaging system-on-a-chip utilizes an advanced CMOS SOI process (GlobalFoundries 45nm SOI CMOS), where millions of transistors are monolithically integrated close to hundreds of photonic devices. Close co-integration of photonics and

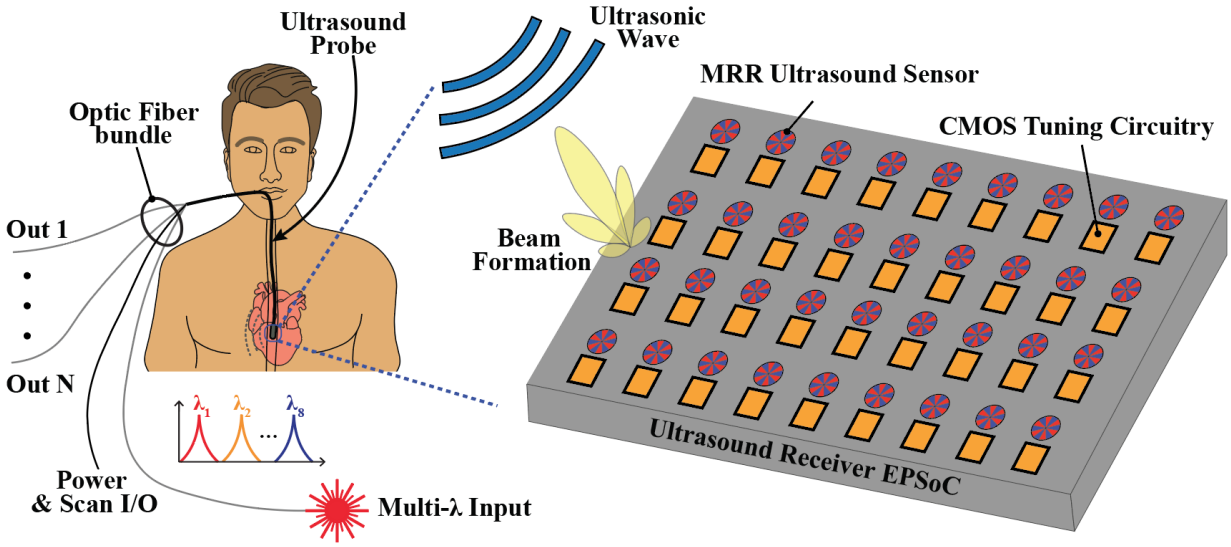

Figure 1.2: Fully integrated ultrasound beamforming sensor EPSoC

,

circuits enables energy efficient tuning of the MRR resonant wavelength, making sure that: a) dense 2-D arrays can operate in a wavelength division multiplexing (WDM) scheme using compact and cheap fixed, multi-λ lasers as optical input, instead of bulky and expensive tunable lasers, and b) the Food & Drug Administration (FDA) safety regulation limits regarding probe heat-up are observed [21]. Apart from enabling realization of dense 2-D beamforming sensor arrays, the monolithic integration of electronics and photonics allows the implementation of receiver EPSoCs, with photodetectors (PDs) and signal conditioning CMOS circuitry placed on a single die, making for a compact ultrasound imaging system like the one shown in Fig. 1.2. Successful demonstration of such a system would pave the way towards a portable and compact ultrasonic probe, that would be on par with the emerging POC diagnostic standards, and a vital tool in the treatment of very important diseases.

1.2 Thesis Organization and Contributions

Having presented the motivation behind optical ultrasound imaging in this introductory chapter, the rest of this thesis details the modeling, analysis, design and experiments involved in building an electronic-photonic system-on-chip (EPSoC) targeting ultrasound receivers meeting specifications of modern POC applications.

Chapter 2 enumerates the existing solutions to endoscopic ultrasound imaging providing background on the state-of-the-art approaches and their shortcomings. Optical counterparts are then presented as a promising alternative, with the needs of endoscopic applications for

small footprint, low power consumption, and potential for scalability to large arrays leading to MRRs as a natural sensor choice among optical solutions.

Chapter 3 outlines the principle of operation of MRR based sensing, enumerating the transduction mechanisms that simultaneously occur when a pressure wave impinges on the MRR surface. Theoretical analysis of these phenomena is accompanied by finite element model (FEM) simulations and validated by experimental results. Parts of this work appear in:

- [22] P. Zarkos, O. Hsu, and V. Stojanović. "Ring resonator based ultrasound detection in a zero-change advanced CMOS-SOI process". In:*CLEO: QELS Fundamental Science.* JW2A–78. Optical Society of America. 2019.

Realizing large biomedical integrated systems on-chip requires rigorous derivation of the application driven specifications with noise, dynamic range, power and area, being of particular importance in endoscopic ultrasound imaging. Chapter 4 presents the design choices and methodology followed in the prototyping of the first generation of ultrasound receiver EPSoCs. Analyses of both analog and digital circuit design as well as electronic-photonic top level integration are discussed. A more general overview of multi-parametric biosensing system design is showcased in:

- [23] C. Adamopoulos, P. Zarkos et al. "Lab-on-Chip for Everyone: Introducing an Electronic-Photonic Platform for Multiparametric Biosensing Using Standard CMOS Processes". In: IEEE Open Journal of the Solid-State Circuits Society (2021).

Prototype design methodology is followed-up by measurement results of silicon-photonic dies fabricated in GlobalFoundries 45nm SOI CMOS. Chapter 5 presents the experimental setup, verification of both electrical blocks and optical devices, as well as optical ultrasound sensing results. These measurement results are also partially published in:

- [24] P. Zarkos et al. "Fully Integrated Electronic-Photonic Ultrasound Receiver Array for Endoscopic Imaging Applications in a Zero-Change 45nm CMOS-SOI Process". In: *2021 Symposium on VLSI Circuits.* IEEE. 2021, pp. 1–2.,

- [25] P. Zarkos et al. "Monolithically Integrated Electronic-Photonic Ultrasound Receiver Using Microring Resonator". In: *CLEO: Science and Innovations.* Optical Society of America. 2021, STh1H–2.,

- [26] P. Zarkos et al. "Fully Integrated Electronic-Photonic Ultrasound Receiver Array for Endoscopic Applications in a Zero-Change 45nm CMOS-SOI Process". In: *IEEE Journal of Solid State Circuits* 2022, in press.

In the first implementation of this ultrasound receiver EPSoC, mature sensor and photodetector ring variants combined with intensity detection schemes were employed. The moderate quality factors of these stable devices resulted in a system which, despite the impressively low power and area, had inferior sensitivity compared to state-of-the-art PMUT

and CMUT counterparts. Nonetheless, test rings with high quality factors, as well as phase detection sensing schemes were implemented on the same SoC. Chapter 6 shows characterization data of high-Q rings and coherent sensing architectures, illustrating the design directions that can make the second generation of ultrasound EPSoCs comparable to the state-of-the-art in terms of sensitivity while retaining the power and area superiority that comes with MRR based optical sensing.

Chapter 2

Background

2.1 Conventional Ultrasound Imaging Technologies

The traditional approach to building ultrasound imaging systems has been to employ a piezoelectric crystal or a capacitive micromachined membrane to perform the transduction from acoustic pressure to electrical signal [27, 28, 29]. With piezoelectric crystals making their first appearance in medicine in the 1950s [30], and capacitive micromachined membranes following in the 1990s [31] (using a similar working principle), both technologies have reached a high maturity level and have provided reliable images over the years for a variety of applications, such as obstetric, abdominal, and pelvic imaging, where no need for a miniaturized, low-power system is required. In this subsection, we explore their use in real-time, 3-D endoscopic and POC ultrasound imaging settings and highlight the shortcomings of the state-of-the-art implementations based on PMUTs and CMUTs. These shortcomings become even more evident in these modern applications, which come with rather aggressive power and area minimization specifications.

2.1.1 State-of-the-art: PMUT and CMUT Implementations

Capturing real-time volumetric images, requires ultrasound endoscopes to evolve from linear 1-D transducer arrays, that were previously used to acquire 2-D scans, to densely packed 2-D transducer matrices. Additionally, improving the signal-to-noise ratio (SNR) and directivity of a beamforming array dictates increasing the number of elements in the array to a point that modern ultrasound probes targeting POC applications consist of 10^3 to 10^4 sensor elements. The upper limit to this number is set by safety regulations for the maximum size of the probe head, while the lower bound is obtained from the $\frac{\lambda}{2}$ pitch that ensures avoiding formation of grating lobes. For example, an imaging system operating at 5MHz, $\frac{\lambda}{2} = 150\mu m$, with a maximum receiver die size of 5mm [33] requires at least 32×32 sensors to avoid side lobes appearing during beamforming. A higher axial resolution requires the frequency to increase further, lowering the sensing element pitch and consequently scaling up the number

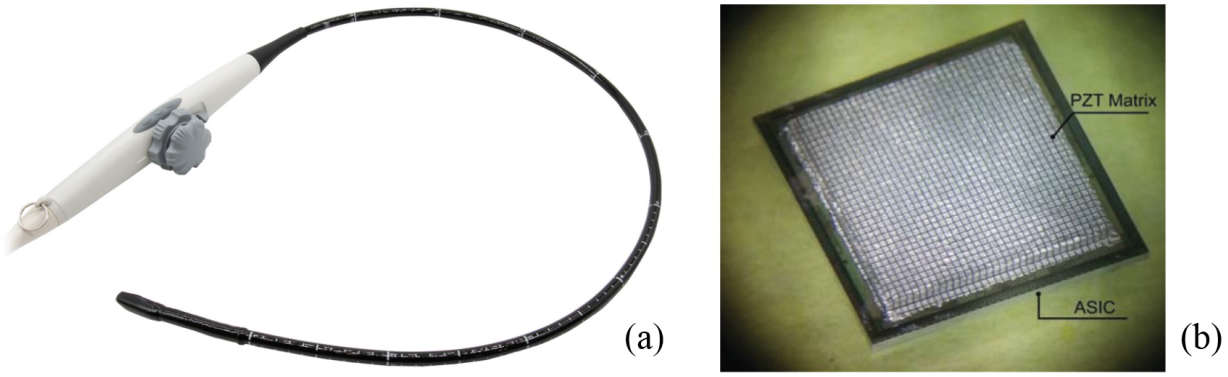

Figure 2.1: (a) Commercially available, PMUT-based volumetric endoscope (Siemens), and (b) PMUT transducer array with 3-D integrated receiver ASIC [32].

of elements. Fig. 2.1a depicts a commercially available endoscopic PMUT based probe, while a PMUT transducer array with co-integrated ASIC is shown in Fig. 2.1b.

Attempting to accommodate the large number of channels that need to fit in the endoscopic probe tube (which has to remain $< 5 - 7$mm in diameter [33]), state-of-the-art approaches have proposed sub-array beamforming to locally reduce the number of I/O channels [34, 35]. In doing so, they give-up some amount of lateral resolution, limit the available beamforming algorithms and further increase power consumption by adding digital logic on-chip to control the sub-array beamforming. The lowest power dissipation reported to date is 0.27mW/element, which sets an upper bound of ~ 1850 elements assuming the power dissipation needs to be kept below 0.5W for endoscopic applications [21]. Alternative approaches have attempted on-chip, in-probe element-wise digitization [36], dissipating 1.54mW/element. Time-division multiplexing [37, 38], and switching schemes with row-column parallel addressed elements [39, 40], have also been proposed to allow multiple elements to share a single cable. Neither of the latter two approaches has been widely adopted however, since both require extra hardware to be integrated on the probe head, be that time-multiplexers or row-column selection logic, hence increasing both power and area consumption. In addition, switching schemes suffer from the appearance of edge waves due to truncation at the element ends. Suggested solutions include apodization integrated in layout of the CMUT cells [40], calling for further increase of the system complexity and transducer matrix fabrication.

A summary of the area, power, and sensitivity performance of state-of-the-art designs employing PMUT or CMUT sensors in conjunction with different cable reduction strategies is tabulated in Table 2.1. There, we also introduce the quantities of noise equivalent pressure density (NEP_{den}), and signal-to-noise and distortion ratio (SNDR). Integrating NEP_{den} over the bandwidth (BW) of interest, yields the total noise equivalent pressure (NEP). NEP and NEP_{den} are interchangeably used in literature, while NEP can also be found as: NEP = N/S,

Table 2.1: Comparison of conventional ultrasound sensing systems

Reference	JSSC '17 [41]	JSSC '17 [32]	JSSC '16 [42]
Process	28nm FD-SOI	180nm LV	180nm LV
Transducer	CMUT	PMUT	CMUT
Integration Method	Flip-Chip	3D Direct	Flip-Chip
Cable Reduction Method	Direct Digitization	Subarray BF	Col/Row Multiplexing
Operating Freq. (MHz)	5	5	5
BW (MHz)	10	6	10
FoV (degrees)	74	180	74
Sensor Pitch (μm)	250	150	250
# of Elements	16	864	256
Power / element (mW)	17.5	0.27	1.4
Area / element (mm^2)	0.0625	0.0225	0.0625
Sensitivity (mV/kPa)	5.75	10	123
NEP_{den} ($mPa/\sqrt{Hz}$)	36.6	2	2.3
SNDR / element (dB)	58.9	49.8	> 40

where N is the integrated input referred electronic noise, and S the sensitivity of the PMUT or CMUT, measured in [V] and [V/Pa] respectively.

2.1.2 Shortcomings of Existing Technology

Based on the discussion above, as the transducer count is expected to keep scaling for modern ultrasound applications such as transesophageal echocardiography (TEE) and intra-vascular ultrasound (IVUS) imaging, traditional approaches will have trouble complying with the regulations regarding both power consumption and probe size, for the following reasons:

- Piezoelectric transducers are designed to optimally operate by choosing the crystal thickness to be half the wavelength of the desired center frequency. Thus, high operating frequencies require very thin crystals, resulting in reliability and fabrication issues. Additionally, PMUTs suffer from an inherent sensitivity-bandwidth trade-off, since lowering element size which is required in order to target higher frequencies also leads to reduced sensitivity.
- A large number of micro-coax cables needed to transfer each elements' received signal to the signal processing unit will be very hard to fit in a sufficiently small probe tube diameter, and the power required to transmit the received signals becomes prohibitive.
- A dedicated, low-noise, pitch-matched analog front-end circuit that picks up the electrical signal needs to be integrated directly underneath the sensing element in the

array. As the operating frequencies increase above 5MHz and elements scale to fit the $\frac{\lambda}{2}$ pitch it will be challenging to fit the sensing circuits under each sensing element and also comply with the overall array power limit.

Finally, it has to be noted that solving the power consumption problem by remoting the receiver circuitry from the probe-head is not a viable option since fanning out all transducer outputs on micro-coax cables will suffer from signal integrity, crosstalk and significant cable loss which will further increase dynamic range requirement of the AFE [43]. Additionally, the overall number of sensing elements will have to be significantly decreased due to fan-out congestion.

2.2 A Promising Alternative: Optical Ultrasound Imaging

Realizing the challenges faced by traditional piezoelectric and capacitive sensors, targeting the next-generation of ultrasound probes, some research groups have proposed the use of optical sensors as a promising alternative [16, 44, 20]. In fact, attempts to build compact ultrasound sensors based on optical techniques date back to the 1970s [45]. A comprehensive review of optical ultrasound sensing for a variety of applications can be found in [46].

Implementations using optical transducers can eliminate the electrical cabling, replacing micro-coax cables with much thinner optic fibers. Furthermore, optical detectors are inherently immune to electric interference, thus alleviating the aforementioned cross-talk issue of PMUTs and CMUTs, while cable loss is no longer an issue since optic fibers typically have < 0.5dB/km loss. At the same time, optical transducers operate with very low quiescent power consumption, and can escape the sensitivity-bandwidth trade-off inherent in CMUT and PMUT transducers, making ideal candidates for multi-modal imaging systems, where varying central frequencies can be used for various imaging modalities.

Interferometric devices with very high sensitivity, based on thin polymer films serving as Fabry-Perot (FP) cavities [15, 47, 17, 44, 48, 16], fiber Bragg gratings [49, 50], plasmonic detection [51], as well as optical MEMS [52] have been proposed. Refractometric methods based on beam deflection [53], polarization-dependent reflection [54, 55], and Schlieren metrology [56] have also been proposed as the interest towards all-optical ultrasound devices has been growing in light of the aforementioned limitations of conventional PMUT and CMUT based imaging. Microring resonators (MRRs) [57, 20, 18] are another class of optical ultrasound transducers that has been gaining popularity.

In this section, the state-of-the-art optical ultrasound implementations are presented, and the use of MRRs as a natural choice for large 2-D arrays of endoscopic imagers is justified.

2.2.1 Interferometric Sensors

A variety of interferometric devices has been proposed for ultrasound sensing [15, 47, 17, 44, 48, 16, 49, 50]. The working principle of these sensors relies on ultrasonic pressure waves to modulate the interference condition of the sensor, either by perturbing directly the optical path length of an FP cavity [15, 47, 17, 44, 48, 16], or by inducing local variations in the coupling coefficient of a Bragg grating [49, 50], depending on the sensor in question.

In the case of FP interferometers, formed by polymer films deposited at the tip of a fiber, as shown in Fig. 2.2a, light reflected from both surfaces of the cavity is detected as the read-out signal, so following [15] we can write:

$$I_0 = I_1 + I_2 + 2\sqrt{I_1 I_2}\cos\Phi, \tag{2.1}$$

where I_0, I_1, and I_2, represent intensities of the superimposed waves, and the reflections from the front and back sides of the cavity, respectively, and Φ the total phase difference between the reflected beams. Breaking Φ down to a constant phase term ϕ, and a small-signal ultrasound induced phase change $\delta\phi$, such that $\Phi = \phi + \delta\phi$, Eq. 2.1 becomes:

$$I_0 = I_1 + I_2 + 2\sqrt{I_1 I_2}\Big(\cos\phi\cos(\delta\phi) - \sin\phi\sin(\delta\phi)\Big) \approx I_1 + I_2 - 2\sqrt{I_1 I_2}\delta\phi, \tag{2.2}$$

where small phase changes, and quadrature bias (i.e. $\phi = 90°$ to ensure maximum sensitivity) have been assumed. The phase shift is related to the ultrasound induced perturbation of optical path length of the FP cavity through the following equation:

$$\delta\phi = \frac{4\pi n_{eff}}{\lambda} dl, \tag{2.3}$$

where n_{eff} is the refractive index in the cavity, dl is the optical path length change due to acoustic pressure, and λ is the input light wavelength. By integrating the net stress across the polymer film, the sensitivity and frequency response of the sensor can be obtained. Single element sensors based on this principle achieve moderate sensitivities, with NEP on the order of ∼300Pa and high bandwidths ranging from 10 to 40 MHz depending on the element size [58], but require a rather complicated scanning and interrogation setup. This configuration also enables very tight integration of multiple sensors on the edge of the probe tip. For example, in [16] a probe with 3.2mm outer diameter, and an unprecedented number of 50,000 elements (fiber cores) has been demonstrated. However, that implementation suffers from long scanning waiting time since each element is sequentially addressed, limited directivity and field-of-view (FOV), and relatively low element sensitivity ($\text{NEP}_{\text{den}} = 281\text{Pa}/\sqrt{\text{Hz}}$, over a 20MHz BW) compared to what has been demonstrated with MRR sensors over similar bandwidths ($\text{NEP}_{\text{den}} = 1.3\text{mPa}/\sqrt{\text{Hz}}$, over a 26MHz BW in [20]). It also requires a high-precision alignment mechanism for accurate coupling into each fiber core, making it rather impractical for adaptation in POC-type systems.

Fiber Bragg gratings with π phase shift jumps on the other hand [49, 50], exhibit a sharp transmission resonance in the middle of their reflecting band as detailed in [59] using the

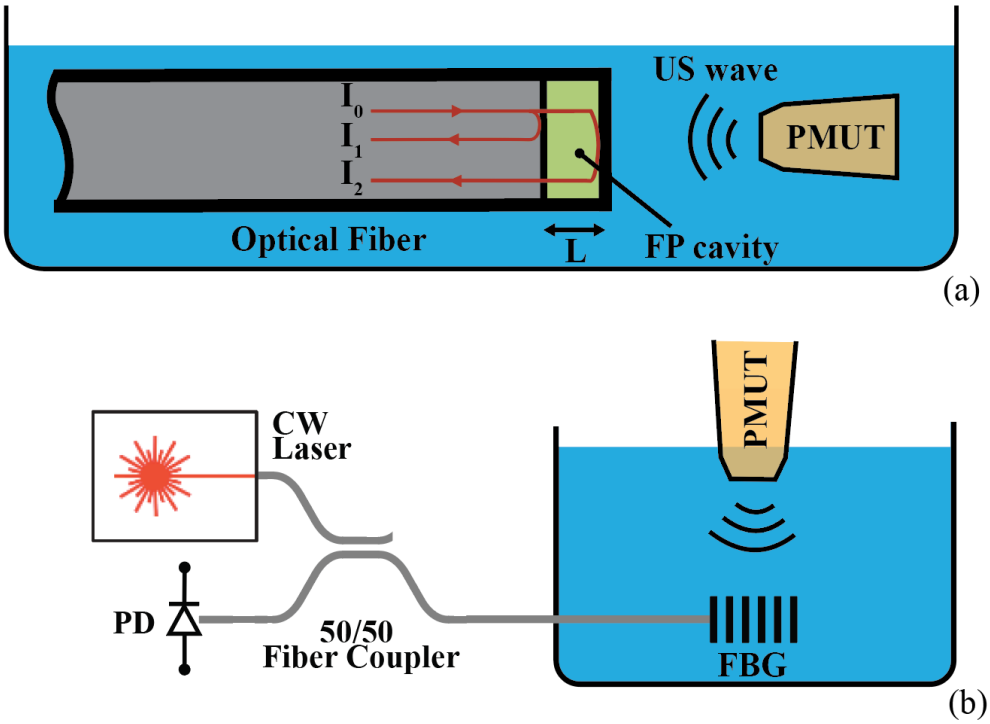

Figure 2.2: Optical sensing configurations for (a) Fabry-Perot interferometer and (b) Fiber Bragg grating

transfer-matrix method:

$$r_g = \frac{2k}{\kappa}\left[\left(\frac{\gamma}{\kappa\tanh(\gamma L/2)} - \frac{ik}{\kappa}\right)^2 - 1\right]^{-1}, \tag{2.4}$$

where k is the wavenumber detuning, κ is the coupling coefficient, $\gamma = \sqrt{\kappa^2 - k^2}$, and L is the grating length. The detuning wavenumber is defined as: $k = 2\pi(\lambda - 2n_{eff}\Lambda)/\lambda^2$, where λ is the input light wavelength, n_{eff} is the fiber refractive index, and Λ is the grating period. Under the assumption that $\kappa L >> 1$ the field in the grating can be approximated as follows [49]:

$$|u(z)| = \sqrt{1 - |r_g(k)|^2}e^{\kappa L/2 - \kappa|z - L/2|}, \tag{2.5}$$

with z ranging between 0 and L, and standing for the direction parallel to the grating. Eq. 2.5 implies that if there is a linear relationship between the coupling coefficient, κ, and the applied pressure, any ultrasound induced changes in κ, will result in exponential change in the transmitted (and reflected) field, making for highly sensitive detectors. The simplest configuration of such a sensor is shown in Fig. 2.2b, where the reflection spectrum is captured using an external PD. Moderate to high sensitivities with NEP = 100Pa, and high

bandwidths up to $\sim$ 70MHz have been reported [50]. However, the relatively large sensor size in the direction of the grating, $\sim 270\mu$m [50] long, makes them rather hard to array and hence inappropriate for use in 3-D endoscopic imaging applications. Miniaturized versions based on optical waveguide Bragg gratings that have been presented in SOI platforms [60], still have a lot of ground to cover since their size ($\sim 0.5 \times 30\mu$m) is comparable to that of MRRs, while the element sensitivity is much lower.

Other interferometric approaches, such as the optical MEMS [52] and plasmonic detection [51] are not going to be mentioned in such detail, since the relatively large footprints, low sensitivities, and complicated configurations they employ do not lend themselves well to endoscopic imaging frameworks.

2.2.2 Refractometric Sensors

Refractometric sensing techniques are classified as intensity [54, 55], phase [61, 56], or beam deflection [53] based. Even though, especially beam deflectometry has demonstrated remarkable sensitivity, with NEP_{den} down to 2.76mPa/$\sqrt{\text{Hz}}$, over a 17MHz of bandwidth [53], the complex, expensive, and area inefficient optical setups of refractometric sensors constitute their use in POC endoscopic applications prohibitive. They should be mentioned though as promising candidates for photoacoustic tomography due to the rather high bandwidths they achieve ($\sim$ 100MHz [55, 56]). For completeness, their sensing principles will be briefly described below, while the interested reader is referred to [54, 55, 61, 55, 53].

Intensity based systems, rely on the different acousto-optic coefficients of two media at the interface of which an incoming light beam propagates. Insonifying this interface results in a change in the reflection coefficient and thus a change in the intensity of the reflected beam which is the sensed quantity.

Phase sensitive refractometric systems also use the acousto-optic effect. The refractive index change induced by pressure modulates the phase of a collimated beam which is then processed by an optical Fourier plane. The spatial filtering provided by the Fourier plane converts phase to intensity modulation yielding a map of the acoustic field that can subsequently be sensed by a camera.

Finally, beam deflectometry is the most sensitive refractometric sensing method and relies on the interaction between the sounds waves and the E/M field of a beam propagating across the acoustic field. It has been found that sound waves can cause beam deflection, which can be sensed with a position sensitive photodetector, with sufficient aperture.

2.2.3 MRR Sensors

One of the most popular optical ultrasound sensing solutions is the microring resonator (MRR) whose typical spectrum has the Lorentzian shape shown in Fig. 2.3. This resonant structure, formed by a circular waveguide coupled onto a straight waveguide, can be used as an ultrasound sensor as long as incoming ultrasound waves sufficiently modulate the resonant wavelength. By parking a laser on the resonance flank, λ_{in}, we can see this modulation

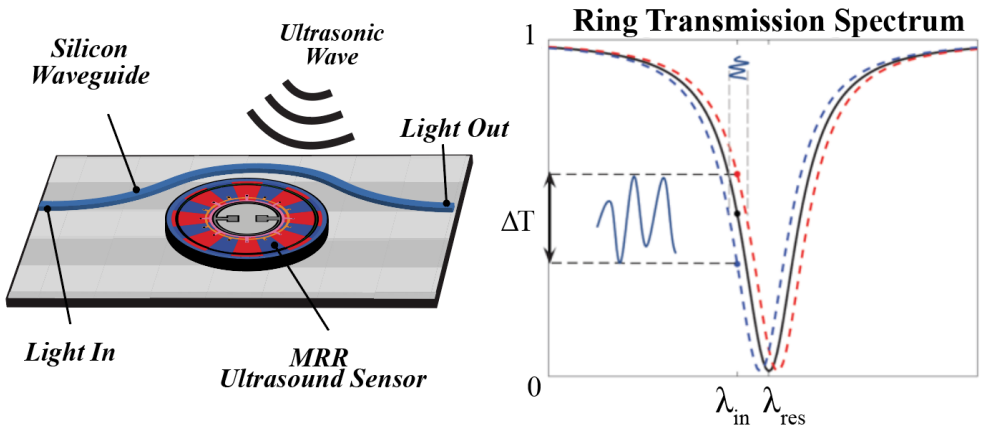

Figure 2.3: Principle of operation of MRR based ultrasound detection, showing an MRR illustration (left) and a typical MRR transmission spectrum (right)

directly translating to a change in the transmitted optical power at the thru port of the resonator. This power fluctuation can then be read out electrically using a photodetector and a transimpedance amplifier (TIA). MRR based ultrasound sensing is presented in detail in Chapter 3.

The high achievable quality factors of MRRs in the 45nm SOI platform (Q up to $2 \cdot 10^5$, [62]) guarantee high detector sensitivity, while the small footprint (down to 10µm diame-

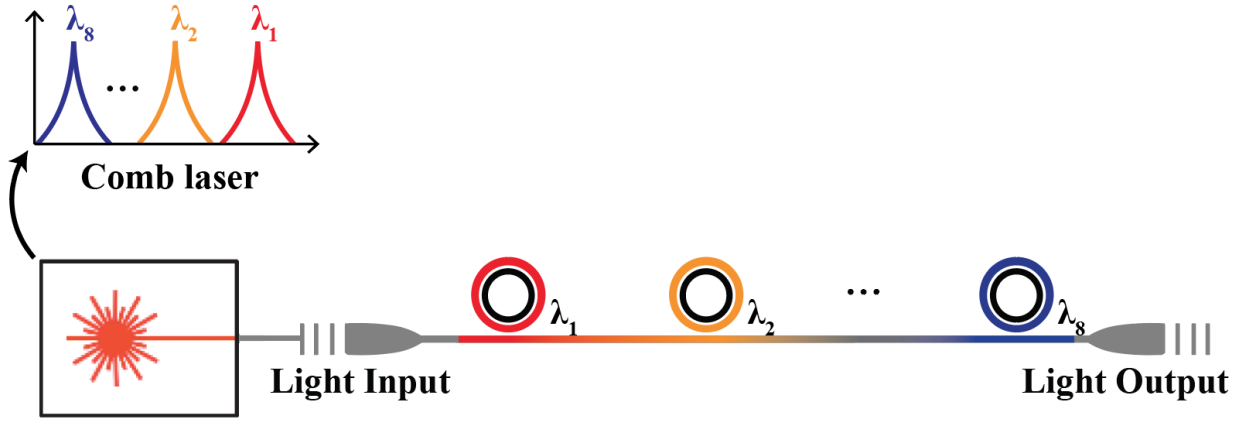

Figure 2.4: Towards a 2-D optical MRR-based ultrasound receiver: A ring row consisting of multiple MRRs coupled onto the same silicon waveguide and interrogated by a comb laser input in a WDM fashion. Arraying multiple such rows in parallel, can form a dense 2-D matrix.

Table 2.2: Comparison of optical ultrasound sensors

Reference	APL '14 [50]	App. Opt. '08 [58]	JSTQE '08 [68]
Transducer	Fiber-Bragg	Fabry-Perot	MRR
Material	Silica	PET/Parylene C	Polystyrene
Operating Freq. (MHz)	18	20	25
BW (MHz)	20	40	30
Power / element (mW)	-	10	**0.32**
Area / element (mm^2)	0.027	0.018	**0.0004**
Q-factor	$1.4 \cdot 10^5$	$2.8 \cdot 10^3$	$\mathbf{1.2 \cdot 10^6}$
$NEP_{den}(mPa/\sqrt{Hz})$	25	78	**5.61**

ter) makes them ideally suited for system miniaturization. Furthermore, MRR ultrasound sensors require ultra-low optical power on the order of $10 - 100\mu W$ to be interrogated, only half of which is dissipated in the ring, thus contributing to probe heat-up, assuming $\sim$ 3dB extinction at the point of maximum sensitivity. Additionally, wavelength division multiplexing (WDM) can be used to interrogate multiple rings coupled onto the same waveguide, effectively reducing the number of required I/O fibers up to 16$\times$ or more (depending on the number of optical modes we can couple onto a single waveguide) with zero power and area overhead. This scheme will also enable us to build large 2D arrays with MRRs arranged in multiple parallel WDM ring rows, like the one shown in Fig. 2.4, where a separate optical mode of an input comb laser can be used to interrogate each ring in the row.

State-of-the-art optical approaches include polymer MRRs developed in a custom process [63, 64], as well as silicon-photonic MRRs fabricated using standard SOI silicon photonic processes [65]. The first approach demonstrated unprecedented detector bandwidth of 300MHz, but failed to show reliable simultaneous operation of multiple receivers [66]. The second one reported superb sensitivity but very small bandwidth [19]. This contrast is due to the different transduction mechanisms simultaneously shifting the ring resonance. The first work relies on waveguide deformation to modulate the refractive index and consequently the resonant wavelength, while the second relies on ring circumference elongation. These transduction mechanisms and the sensor operating principle will be explained in detail in Chapter 3. Our analysis has shown that ring circumference elongation, despite its potential for high sensitivity, comes with the drawback of an inherent sensitivity-bandwidth trade-off, similar to the one experienced by PMUTs and CMUTs, since it originates in a mechanical resonance of the membrane where the ring is placed. Sensors that achieve high bandwidth without giving up sensitivity are preferable, as they can target multiple different applications and provide detailed, high resolution images of many physiological traits such as the anatomy of tissue and microvasculature or even metabolic processes [67].

A summary of the performance of all the aforementioned optical sensing techniques is tabulated in Table 2.2. From this Table and the discussion above, it is clear that MRR

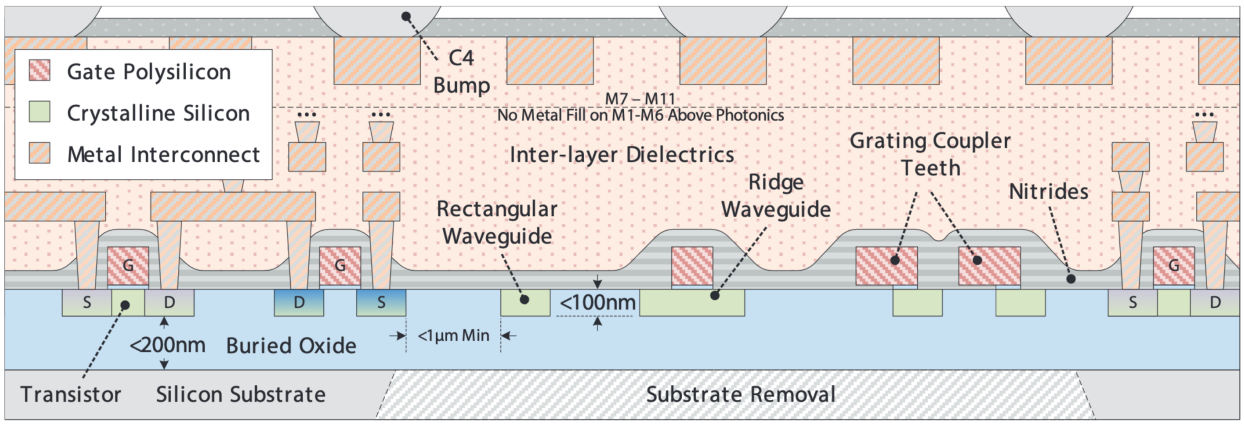

Figure 2.5: 45nm SOI CMOS process cross-section with relevant devices, from [70]

ultrasound sensors are an ideal candidate for use in POC and endoscopic types of applications, since they combine minimal sensing element size and power consumption with high scalability of their interrogation scheme.

2.2.4 Challenges and Innovations

2.2.4.1 Multi-MRR 2-D Arrays

Moving from 2-D to 3-D imaging systems requires multi-element, compact 2-D sensor arrays at the tip of the probe to perform beamforming. Despite their high-sensitivity and ultra-low form-factor [69, 20, 66], currently available MRR-based sensing platforms fail to meet key requirements of next-generation endoscopic ultrasound imagers that would enable scalability and miniaturization of the system. First, they lack a robust way to tune and lock the resonant wavelength of these devices. Given that MRR based sensors rely on matching the wavelength of the incoming laser to the flank of the Lorentzian shaped resonant spectrum, not being capable to reliably tune the resonance, necessitates the use of expensive, bulky tunable lasers, instead of low-cost fixed-wavelength light sources, and prohibits real-time simultaneous interrogation of all the sensor elements in the array. Second, the passive nature of current platforms cannot provide a compact readout processing system, thus hindering the development of highly portable Lab-on-Chip (LoC) systems. These limitations result in systems that still heavily rely on complex optics and external readout equipment for precise optical scanning and highly sensitive readout processing, such as the one presented in [20, 16].

In this thesis, we will address these challenges by introducing a fully integrated electronic-photonic biosensing platform in a high volume advanced CMOS-SOI process to implement a first of its kind Electronic-Photonic System-on-Chip (EPSoC). A cross-section of our "zero-change" GF45nm platform [71] is illustrated in Fig. 2.5. Taking advantage of co-integration

of planar MRRs with on-chip electronics, we eliminate the need for a tunable laser and external readout equipment by shifting the requirements of resonance tuning and readout processing to the electronic domain. At the same time, by combining the inherent sensitivity of MRRs as biosensing devices and integrating multiple rings into a chip-scale array-based architecture, we enable highly scalable 2-D sensor arrays with true real-time simultaneous interrogation capability, combined with one of the lowest power consumption and highest sensor densities and reported in literature [24].

In summary, we will attempt to overcome the challenges posed by modern endoscopic ultrasound specifications through the following research avenues:

- Investigation of the use of micro-ring resonators as ultrasound sensors in a "waveguide deformation" mode, where the sensitivity-bandwidth trade-off of traditional ultrasound transducers is mitigated;
- Remoting the receiver electronics from the probe-head, which can significantly increase the SNR under a given power envelope inside the body, since more power can be externally dissipated to lower TIA noise, without contributing to probe heat-up;
- Replacing bulky tunable lasers and complicated read-out frameworks common in optical implementations with a fixed wavelength multiple channel comb laser that will reduce system complexity and cost, while being compatible with LoC standards;
- Realization of an electronic-photonic receiver array based on energy efficient, ultra-compact, and highly sensitive micro-ring resonators using an automated photonic layout generation framework, the Berkeley Photonics Generator (BPG) [72];
- WDM interrogation of multiple MRRs grouped in a ring row, which will allow probe tube wiring minimization; this will be enabled through the design of compact thermal resonance tuning control loops co-integrated with the sensors;
- Utilization of the two previous concepts to implement a dense beamforming receiver array with sensors that have 10μm diameter and can be tightly packed to target high frequency ultrasound applications, providing superior resolution;

2.2.4.2 Transmit Functionality and an All-Optical Ultrasound Probe

Since the MRR based receivers lack transmit functionality the focus is placed on the ultrasound receive path in this thesis. However, a small dedicated PMUT transmitter array could be co-packaged with our receiver array to implement TX functionality, similarly to what was proposed in [73]. This would constitute a complete ultrasound imaging system where the small PMUT would perform efficient, omnidirectional ultrasound generation and 3-D images of the echos would be reconstructed using a dense MRR-based beamforming array.

At the same time, the photonic nature of the sensing element would make the proposed system a viable candidate for use in emerging multi-modal ultrasound receivers where photoacoustically generated ultrasound is combined with traditional time-of-flight ultrasonic

echo. Such a system would provide a mixture of absorption contrast and structural contrast information, giving the physician more insight. Such an all-optical approach to compact photoacoustic and multi-modal ultrasound imaging would eliminate the electrical signalling connections and interfaces traditional sensors need. In fact, implementations of multi-modal TX-RX optical ultrasound have also been reported in literature [74]. In that work, a dichroic filter is used to either generate ultrasound photoacoustically and reconstructing pulse-echo images, or allow a laser excitation to generate a photoacoustic response from the tissue under examination. Such implementations are also compatible and can conceivably be co-packaged with our EPSoC solution.

Chapter 3

Ring Resonator Based Ultrasound Sensing

In this chapter we first introduce the microring resonator (MRR) by deriving fundamental quantities describing its behavior, along with a generic sensitivity optimization analysis. Subsequently, we present the sensor's operating principle pertinent to ultrasound and define useful metrics to quantify and analyze the MRR sensitivity. An extensive theoretical analysis of the transduction phenomena that occur is also provided, backed by finite element model (FEM) simulation. Finally, preliminary experimental results are shown, verifying the analysis and proving the MRR-based ultrasound sensing concept.

3.1 Microring Resonator Fundamentals

3.1.1 Spectral Characteristics

MRRs are comprised of a bus waveguide coupled to a circular waveguide, as illustrated in Fig. 3.1a. When the wavelength of the input light is such that the phase shift accumulated around the ring is an integer multiple of 2π, the ring is said to be on resonance. In this case, destructive interference occurs at the thru-port of the ring, and the power circulating inside the ring is maximized [69]. At off-resonant wavelengths, more power is transmitted to the thru port, resulting in the Lorentzian shaped transmission spectrum of Fig. 3.1b, where fundamental spectral characteristics of the ring transfer function such as the full width at half maximum ($FWHM$), free spectral range (FSR), and extinction ratio (ER), are indicated.

MRRs used in this work are coupled to a single waveguide, in what is known as an all-pass filter (APF) or notch filter configuration. Other topologies, such as racetrack ring resonators (where the ring shape across the coupling region is elongated), add-drop MRRs (where the ring is coupled to two waveguides), and double-ring (or multi-ring) filters, have also been used for ultrasound sensing [19, 75, 76].

When considering an all-pass ring, the magnitude of the transfer function from the input

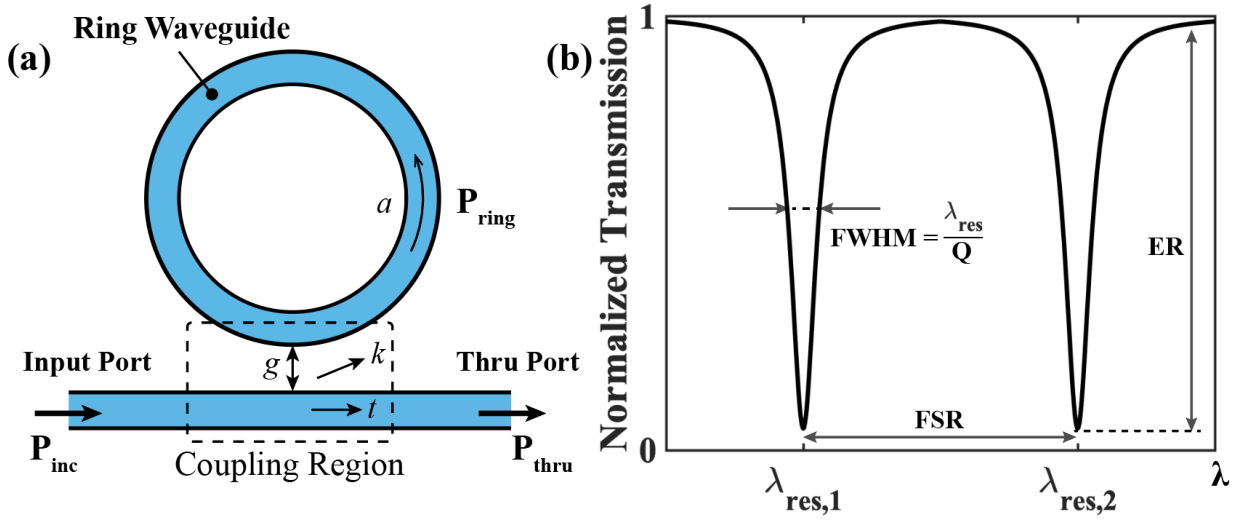

Figure 3.1: (a) Structure of a micro-ring resonator (MRR). (b) Lorentzian spectrum of the ring, with the λ_{res}, $FWHM$, FSR, and ER labeled. On resonance, most of the optical power circulates inside the MRR waveguide.

to the thru port can be derived under the assumption of lossless coupling and unidirectional mode excitation as [77, 78]:

$$T = \frac{P_{thru}}{P_{inc}} = \frac{a^2 + t^2 - 2at\cos\phi}{1 + (ta)^2 - 2ta\cos\phi}, \tag{3.1}$$

where t is the self-coupling coefficient, ϕ is the round-trip phase-shift, and a is the single-pass amplitude transmission, given by $a = \exp(-\alpha L)$, $\alpha[\text{cm}^{-1}]$ being the power attenuation coefficient and L the round-trip length of the MRR. It should be noted that the lossless coupling assumption implies: $t^2 + k^2 = 1$, where k is the cross-coupling coefficient.

It can be seen from Eq. 3.1, that the transmission on resonance (where $\phi = 0$) goes to zero when $t = a$, a condition known as critical coupling. When $t < a$ the ring is said to be overcoupled, and when $t > a$ the ring is said to be undercoupled. The extinction ratio, ER, is defined as the maximum (off-resonance) over the minimum (on-resonance) transmission, and is maximized at critical coupling.

The resonator full width at half maximum ($FWHM$), also known as 3dB bandwidth, can be found through manipulation of Eq. 3.1. [78]:

$$FWHM = \frac{(1 - ta)\lambda_{res}}{\pi n_g L\sqrt{ta}}, \tag{3.2}$$

where n_g is the group index, introduced to account for first order wavelength dependence of the refractive index, $n_g = n_{eff} - \lambda\frac{\partial n_{eff}}{\partial\lambda}$.

Given that resonance occurs when the round-trip phase is equal to an integer multiple of 2π, the resonant wavelength can also be derived using the propagation coefficient $\beta = kn_{eff} = \frac{2\pi}{\lambda}n_{eff}$, where k is the wavenumber, λ the input light wavelength, and n_{eff} the refractive index of the waveguide.

$$\begin{aligned} \phi = 2\pi m \Rightarrow \beta L = 2\pi m \\ \Rightarrow \lambda_{res} = \frac{n_{eff}L}{m}. \end{aligned} \tag{3.3}$$

The resonator quality factor, defined as the ratio of the energy stored over the energy lost per cycle serves as a measure of the Lorentzian sharpness with respect to the resonant wavelength, and consequently as a measure of the sensor's sensitivity. For all-pass MRRs it is:

$$Q = \frac{\lambda_{res}}{FWHM} = \frac{\pi n_g L\sqrt{ta}}{(1-ta)\lambda_{res}} \tag{3.4}$$

Another important spectral characteristic of MRRs, especially when considered for use in WDM implementations, is the distance between adjacent resonances, known as free spectral range (FSR). Given that two adjacent resonances occur for wavelengths that incur an additional 2π round-trip phase shift, and accounting for dispersion, the $FSR = \delta\lambda$ can be calculated as follows [78]:

$$\begin{aligned} \delta\phi = 2\pi \Rightarrow \delta(\beta L) = 2\pi \\ \Rightarrow L\delta\lambda\frac{\partial\beta}{\partial\lambda} = -2\pi \\ \Rightarrow FSR = \delta\lambda = -\frac{2\pi}{L}\left(\frac{\partial\beta}{\partial\lambda}\right)^{-1}\Big|_{\lambda_{res}} = \frac{\lambda_{res}^2}{n_g L}, \end{aligned} \tag{3.5}$$

To derive Eq. 3.5 the resonant wavelength expression (Eq. 3.3) was combined with the partial derivative of the propagation coefficient with respect to wavelength which can be expressed in terms of the group index to account for dispersion:

$$\frac{\partial\beta}{\partial\lambda} = -\frac{2\pi}{\lambda^2}n_{eff} + \frac{2\pi}{\lambda}\frac{\partial n_{eff}}{\partial\lambda} = -\frac{k}{\lambda}n_g. \tag{3.6}$$

With respect to sensing applications, MRRs with high quality factors are desirable to maximize sensitivity. At the same time, a well-known trade-off between Q-factor and optical bandwidth exists, as indicated by Eq. 3.4. To quantify this trade-off consider an O-band MRR with $Q = 80,000$, for which the optical bandwidth will be $\lambda_{res}/Q = 162.5\text{pm} \approx 3\text{GHz}$, assuming $\lambda_{res} = 1300\text{nm}$. Such optical bandwidths can easily accommodate both traditional endoscopic applications which require BW of ∼10s of MHz, and μm scale resolution photoacoustic applications with BW of∼100s of MHz, without giving up sensitivity. O-band MRRs with $Q = 80,000$ have actually been designed in the course of this thesis and will be presented in Chapter 6, while passive rings with up to $2 \cdot 10^5$ have been previously measured

in our "zero-change" monolithic platform [62]. Finally, when building an MRR WDM row, the microring FSR needs to fit all channels of the interrogating fixed-wavelength laser comb in order to avoid inter-symbol type interference between ring sensors of the same row. In our experiments, comb laser diodes with 80GHz (or equivalently 0.45nm) channel spacing are used with rings of $FSR \approx 18$nm meaning that up to 40 channels can be incorporated in a single WDM ring row without any ISI concern.

3.1.2 Sensitivity Optimization

Maximizing the sensitivity of an MRR sensor is equivalent to maximizing the slope of the power transmission spectrum. Taking the derivative of Eq. 3.1 with respect to the detuning angle, ϕ_{det} (which is defined as the offset from on resonance round trip phase shift $\phi = 2\pi m$),

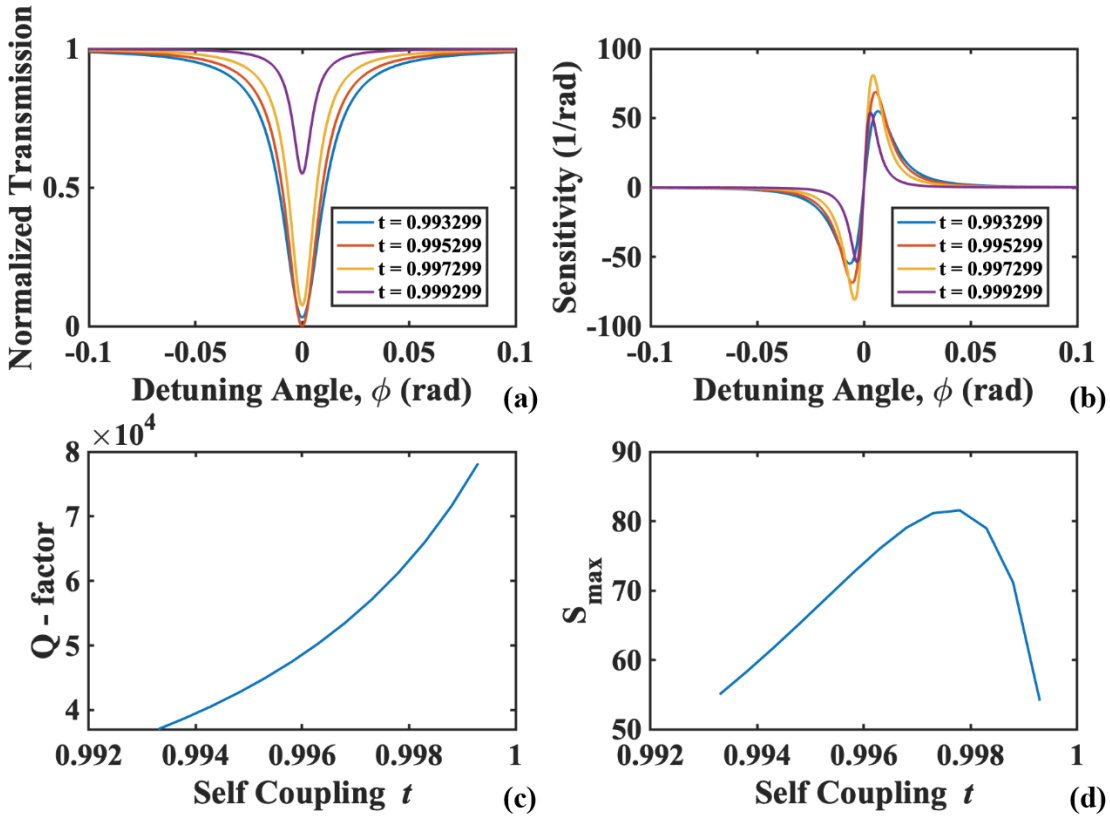

Figure 3.2: (a) Lorentzian transfer functions for undercoupled, critically coupled and over-coupled MRRs, for a single-pass amplitude transmission $a = 0.9553$. (b) Derivatives of the Lorentzian spectra in (a), (c) Q-factors vs self-coupling coefficient, and (d) Maximum sensivity vs self-coupling coefficient for a given loss coefficient and ring size.

we get:

$$S_{max} = \max\left(\frac{\partial T}{\partial \phi_{det}}\right) = \max\left(\frac{2ta\big(1-t^2-a^2+(ta)^2\big)\sin\phi_{det}}{\big(1+(ta)^2-2ta\cos\phi_{det}\big)^2}\right) \tag{3.7}$$

As pointed out in [79], if the Q-factor of the resonator is considered constant, the maximal slope of the resonator is obtained at critical coupling, where $ER = 1$. However, at design time, and assuming that device doping is fixed, there is no capability of fine-tuning both the intrinsic power attenuation coefficient, a, and the self-coupling parameter t in order to keep the quality factor of the device fixed. On the other hand, it is plausible to modify the coupling gap, g, for a given a, thus only changing the coupling coefficients, t, and k. Fig. 3.2 a, b illustrates Lorentzian transfer functions as well as their derivatives (sensitivity curves) as a function of detuning angle for various values of coupling coefficients. The Q-factors and maximum sensitivity as a function of the self-coupling coefficient, t are also plotted in Fig. 3.2 c, d. The parameters used to obtain these plots, through Eqs 3.1, 3.4, and 3.7 were $\alpha = 13$dB/cm, and $r = 5\mu$m for the ring diameter, corresponding to 0.04dB round-trip loss. The group index is $n_g = 3.89$, and $n_{eff}(\lambda) = 2.57 - 0.85(\lambda - 1.55)$ (λ in [μm]) [80]. These parameters will be assumed the same across this manuscript, unless otherwise stated. In agreement with [79], maximum sensitivity occurs at half-critical coupling (i.e. in the undercoupled region) where:

$$\frac{1-t}{1-a} = \frac{1}{2} \tag{3.8}$$

It should be noted that an additional knob for sensitivity optimization is lowering the intrinsic loss to increase the Q-factor before selecting a coupling gap, as is done in Chapter 6.

3.2 Sensing Principle

MRR-based sensors detect the modulation of their resonant wavelength induced from the quantity being sensed, which in our case is ultrasonic pressure. Key for this modulation is the change in the optical mode confinement, which in turn results in a change of the effective index of refraction, Δn_{eff}, as illustrated in Fig. 3.3 a. In ultrasound sensing, the impinging pressure waves primarily deform the waveguide height (Δh), leading to a less confined optical mode, thus lowering the effective index [22]. This perturbation causes a change of both the phase and amplitude of the transmitted optical field, which needs to be converted to an electrical signal for post-processing and image rendering. This is often done using a photodetector (PD) and a transimpedance amplifier (TIA), as shown in Fig 3.3 b. In the following, the transduction steps and the corresponding sensitivities are presented as the sensed signal moves from the acoustic to the optical and finally to the electrical domain.

3.2.1 Intrinsic Sensitivity

In traditional ultrasound sensors based on CMUT and PMUT devices, sensitivity is commonly defined as the output voltage amplitude per unit of applied pressure [V/Pa]. However,

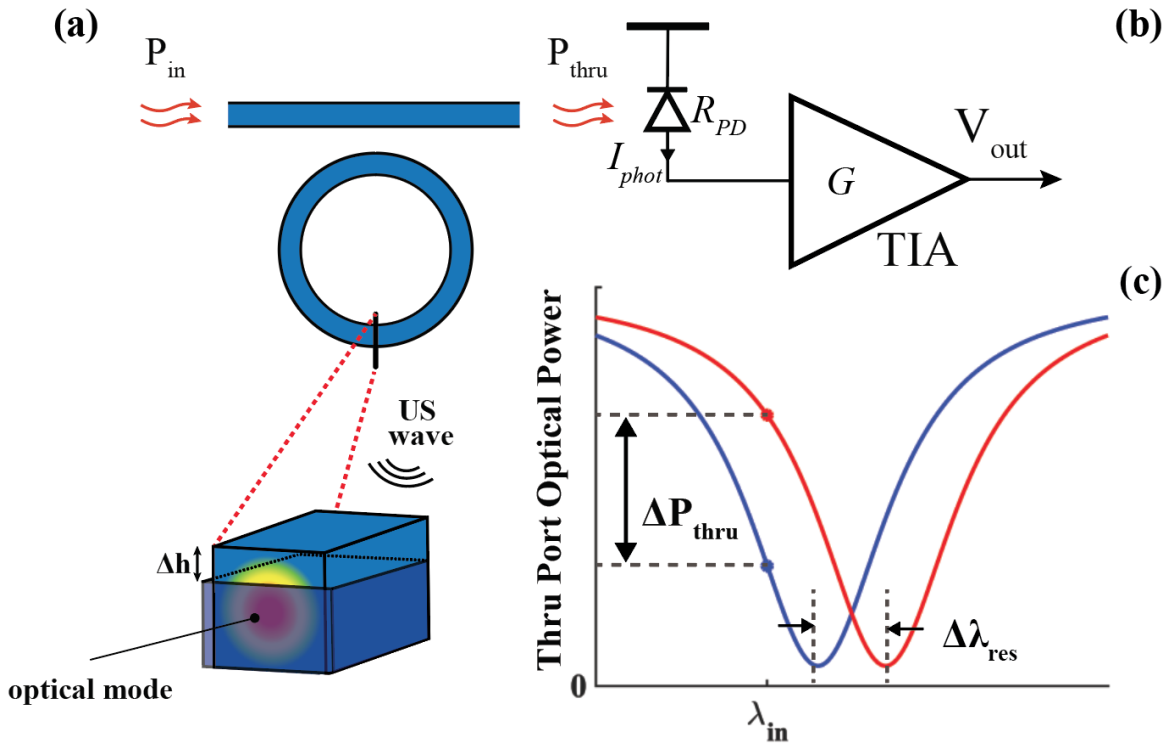

Figure 3.3: Principle of operation in MRR-based ultrasound sensing: (a) Ultrasound pressure alters the confinement of the optical mode propagating in the Si waveguide, inducing a change in the effective index, Δn_{eff}. (b) A photodetector and a TIA convert the optical signal to the electronic domain. (c) Δn_{eff} results in a resonant shift of the ring, $\Delta\lambda_{res}$. Operating at fixed wavelength, λ_{in}, the shift in resonance induces a fluctuation in the transmitted optical power, ΔP_{thru}.

in optical MRR based ultrasound sensors additional transduction steps occur. Given that the immediate effect of an ultrasound wave is to induce a shift in the resonant wavelength of the sensor, it is rather useful to introduce an intermediate sensitivity metric. Defining the *intrinsic sensitivity*, S_{int}, of an MRR-based ultrasound sensor as the change of the resonant wavelength due to an applied pressure P_{app}, we can manipulate (3.3) to get:

$$S_{int} = \frac{\partial\lambda_{res}}{\partial P_{app}} = \frac{L}{m}\left(\frac{\partial n_{eff}}{\partial P_{app}} + \frac{\partial n_{eff}}{\partial\lambda_{res}}\frac{\partial\lambda_{res}}{\partial P_{app}}\right) + \frac{n_{eff}}{m}\frac{\partial L}{\partial P_{app}}$$
$$\Rightarrow \frac{\partial\lambda_{res}}{\partial P_{app}}\left(1 - \frac{L}{m}\frac{\partial n_{eff}}{\partial\lambda_{res}}\right) = \frac{L}{m}\frac{\partial n_{eff}}{\partial P_{app}} + \frac{n_{eff}}{m}\frac{\partial L}{\partial P_{app}},$$

where L is the MRR circumference, m the resonance order, and n_{eff} the effective index of refraction. Using Eq. 3.3 and $n_g = n_{eff} - \lambda_{res}\frac{\partial n_{eff}}{\partial \lambda_{res}}$, we can write:

$$1 - \frac{L}{m}\frac{\partial n_{eff}}{\partial \lambda_{res}} = 1 - \frac{\lambda_{res}}{n_{eff}}\frac{n_{eff} - n_g}{\lambda_{res}} = \frac{n_g}{n_{eff}}.$$

So finally we get:

$$S_{int} = \frac{\partial \lambda_{res}}{\partial P_{app}} = \frac{n_{eff}}{n_g}\Big(\frac{L}{m}\frac{\partial n_{eff}}{\partial P_{app}} + \frac{n_{eff}}{m}\frac{\partial L}{\partial P_{app}}\Big) = \frac{n_{eff}}{n_g}\Big(\frac{\lambda_{res}}{n_{eff}}\frac{\partial n_{eff}}{\partial P_{app}} + \frac{\lambda_{res}}{L}\frac{\partial L}{\partial P_{app}}\Big). \quad (3.9)$$

Intrinsic sensitivity can be optimized through photonic and/or MEMS design, as was done in [20], where the small air gaps engineered between the slab and rib parts of the waveguide amplified the interaction of the ultrasonic waves with the evanescent optical field. Nevertheless, for a given device type (e.g. typical APF MRRs), S_{int} depends mostly on the material properties of the given fabrication process, and is hence a fundamental indicator of the suitability of that process for ultrasound sensing.

3.2.2 Electronic - Photonic Sensitivity

With the MRR biased at a fixed input wavelength, λ_{in}, any shift of the ring resonance results in a fluctuation of the amplitude of the circulating and transmitted fields in the circular and bus waveguides respectively, as shown in Fig. 3.3 c. In sensing schemes where the sensed quantity is the varying intensity of the transmitted optical field, we can define the *photonic sensitivity*, S_{phot}, as the amount of change in the transmitted optical power per induced resonant shift:

$$S_{phot} = \frac{\partial P_{thru}}{\partial \lambda_{res}} \approx P_{thru}\frac{1}{FWHM} = P_{thru}\frac{Q}{\lambda_{res}}, \quad (3.10)$$

where P_{thru} is the transmitted optical power, Q is the quality factor of the micro-ring resonator, and we have assumed full extinction (i.e. critical coupling) and operation around a linear region close to the maximum slope point. The full extinction assumption is valid even for optimally biased slightly undercoupled rings, which still exhibit high ER, as shown in Fig. 3.2a. As intuitively expected, resonators with lower losses and hence higher quality factors will have proportionately higher photonic sensitivity.

Finally, in order to process the sensor information encoded in the amplitude of the circulating or transmitted field, this power fluctuation is converted into the electrical domain using a photodetector with responsivity R_{PD}, and a transimpedance amplifier (TIA) with gain R_{TIA}, as shown in Fig. 3.3b.

The *total sensitivity*, S_{tot} of this transduction chain can be written as:

$$S_{tot} = \frac{\partial V_{out}}{\partial P_{app}} = \frac{\partial \lambda_{res}}{\partial P_{app}}\frac{\partial P_{thru}}{\partial \lambda_{res}}R_{PD}G \approx S_{int}S_{phot}R_{PD}G. \quad (3.11)$$

This sensitivity analysis combined with the noise limitations will determine the system's limit of detection, LoD, or else the noise equivalent pressure, NEP, as will be shown in Chapter 4.

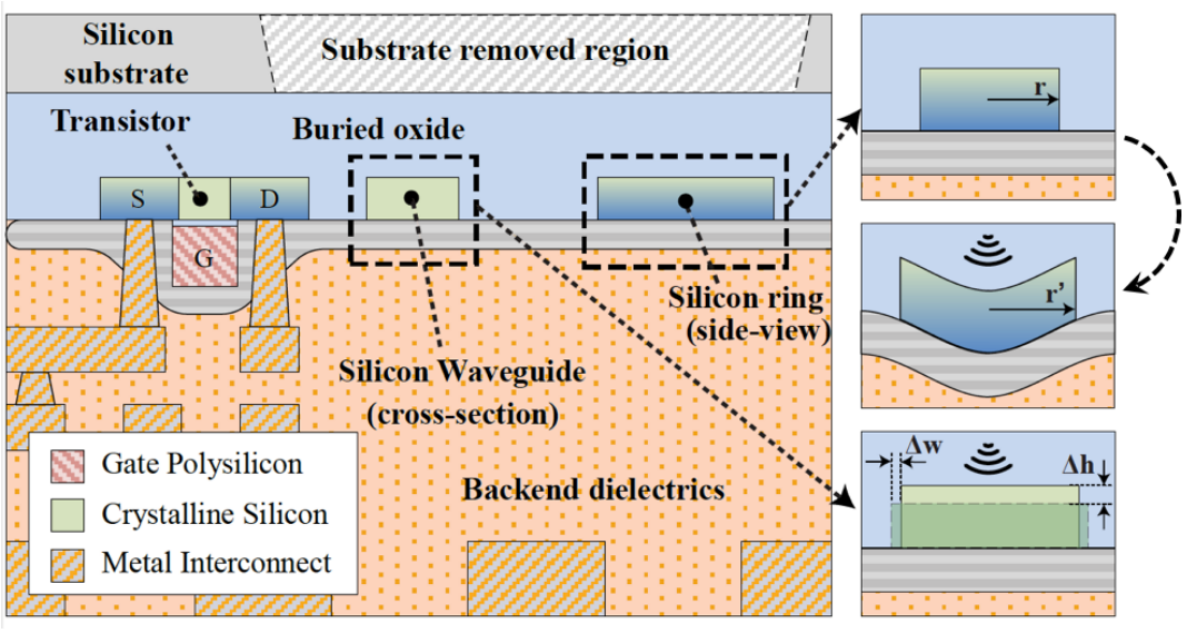

Figure 3.4: Zero-change 45nm CMOS-SOI process cross-section with insets showing the effect of a pressure wave causing ring elongation in side-view (top and middle right), and waveguide deformation in cross-section (bottom right)

3.3 Ultrasonic Transduction Mechanisms

Moving towards the implementation of an optical ultrasound receiver array based on MRRs, our first step was to develop theoretical understanding of the ultrasonically induced resonant shift. Given that closed formula expressions of the exact phenomenon were not always tractable, we also turned to finite element model (FEM) simulations to develop intuition on the observed phenomena and form theoretical expectations that would help us guide our design process.

Identifying the transduction mechanisms that take place when an ultrasonic pressure wave impinges upon the MRR we recognized three physical phenomena simultaneously shifting the MRR resonance under insonification: a) waveguide deformation, b) ring circumference elongation, and c) opto-elastic refractive index change. Decoupling them and understanding which of the three dominates the response of the sensor is crucial for the realization of a large integrated sensor array system based on MRRs. The first two of these phenomena are animated in the cross section of the 45nm zero-change platform in which we intend to build this electronic-photonic system, in Fig. 3.4.

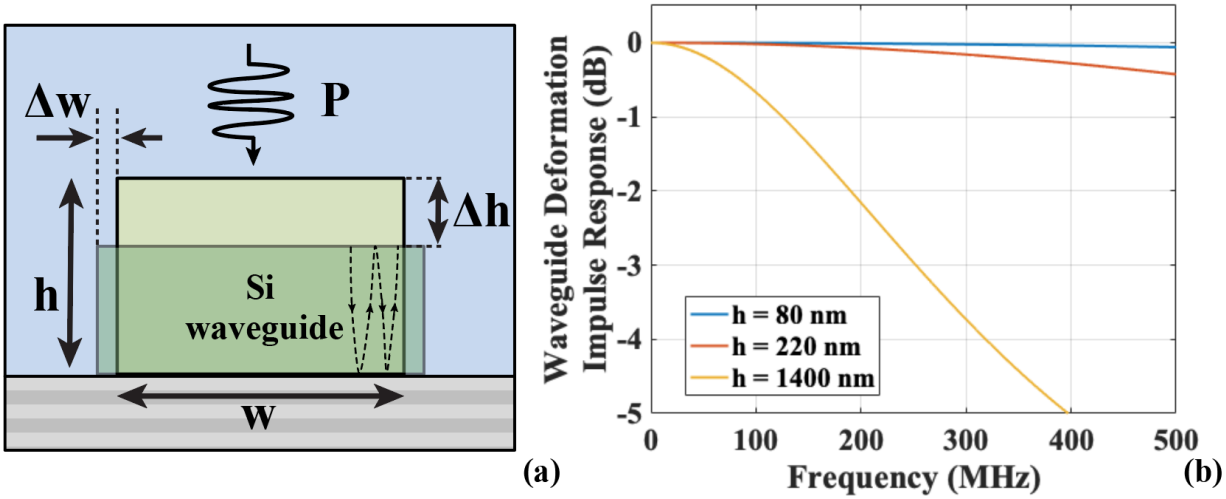

Figure 3.5: Waveguide Deformation: (a) Illustration of waveguide deformation under impinging ultrasonic pressure wave, (b) Impulse response of waveguides of various thicknesses and materials, demonstrating the advantage of 45nm CMOS-SOI (h = 80nm) over other established Si-Ph processes (h = 220nm), and custom MEMS processes with polymer MRRs (h = 1400nm).

3.3.1 Theoretical Analysis

3.3.1.1 Waveguide Deformation

Waveguide deformation can be modeled as pure modulation of the waveguide thickness. More pressure results in a more compressed waveguide as shown in Fig. 3.5. Consequently, the optical mode is less confined and the refractive index drops, leading to a decrease of the resonant wavelength (also known as a blue shift), as expected from Eq. 3.9.

A theoretical estimation of the frequency response, $P_I(k)$ of this phenomenon can be obtained, if we integrate the mean stress distribution, P_T, along the height of the waveguide, following the procedure outlined in [81] for the purpose of Fabry-Perot interferometers based on polymer films:

$$P_I(k) = \frac{1}{h}\int_0^h P_T(y,k)\,dh, \tag{3.12}$$

where k is the acoustic wavenumber, h is the waveguide height, and y the direction of incidence of the acoustic wave (which is perpendicular to the light propagation direction).

To estimate $P_T(y,k)$ we can assume that the incoming longitudinal pressure wave and it's reflections off of the silicon - buried oxide (BOX), and silicon - nitride layer interfaces

form a standing wave inside the waveguide, as shown in Fig. 3.5 a, so that we can write:

$$P_T(y,k) = T\sum_{i=0}^{\infty}\Big((R_1R_2)^i e^{i(\omega t - k(2hi-y))} + R_1^{i+1}R_2^i e^{i(\omega t - k(2hi+y))}\Big), \tag{3.13}$$

where T is the transmission coefficient of the incident pressure wave, R_1, R_2, are the reflection coefficients at the silicon - BOX, and silicon - nitride layer interfaces respectively, ω is the acoustic angular frequency, t represents time, and i is the reflection order. These reflections occur due to acoustic impedance mismatch between the different materials and their coefficients can be derived as:

$$R_1 = \frac{Z_2 - Z_0}{Z_2 + Z_0}, \quad R_2 = \frac{Z_1 - Z_0}{Z_1 + Z_0}, \tag{3.14}$$

where Z_0, Z_1, Z_2 are the acoustic impedances of silicon, nitride layer, and BOX respectively.

Evaluating this infinite series sum and plugging it into the integral of Eq. 3.12 we get the frequency response of the waveguide to a normal stress excitation as:

$$P_T(k) = \frac{T\sqrt{2}}{kh}\sqrt{\frac{(R_1^2+1) + 4R_1\cos(kh)\sin^2(kh/2) - (1+R_1^2)\cos(kh)}{1 - 2R_1R_2\cos(2kh) + (R_1R_2)^2}} \tag{3.15}$$

This response is plotted in Fig. 3.5 using reflection coefficients $Z_0 = 19.7$MRayl, $Z_1 = 21.8$MRayl, $Z_2 = 13.2$MRayl from [82]. Different values of waveguide thickness corresponding to our monolithic platform and other commercially available silicon photonics processes [19] are used, while the response of a custom polymer ring process [64, 63, 83] that has previously been used for MRR ultrasound sensing is also shown. It can be seen in Fig. 3.5 that the small waveguide thickness of our platform can provide superior bandwidth compared to previously demonstrated solutions.

It is worth mentioning that in the above derivations of the frequency response (Eq. 3.12) and mean stress distribution (Eq. 3.13), the lateral dimension of the waveguide are assumed much larger than the thickness such that no radial resonant modes are excited. This assumption is not entirely true in our technology since $w = 480$nm, and $h \approx 80$nm, so deviations of the measured frequency characteristics of the sensor from the developed theory could be expected.

3.3.1.2 Ring Elongation

Ring elongation is shown again in Fig. 3.6a. As illustrated, when a round film is stressed its perimeter will expand, causing the overall round-trip length to increase; hence an increase in the resonant wavelength (red-shift) is expected. This indicates that it will be fighting the effect of waveguide deformation and optimization of the ring's sensitivity to ultrasound dictates minimizing one over the other.

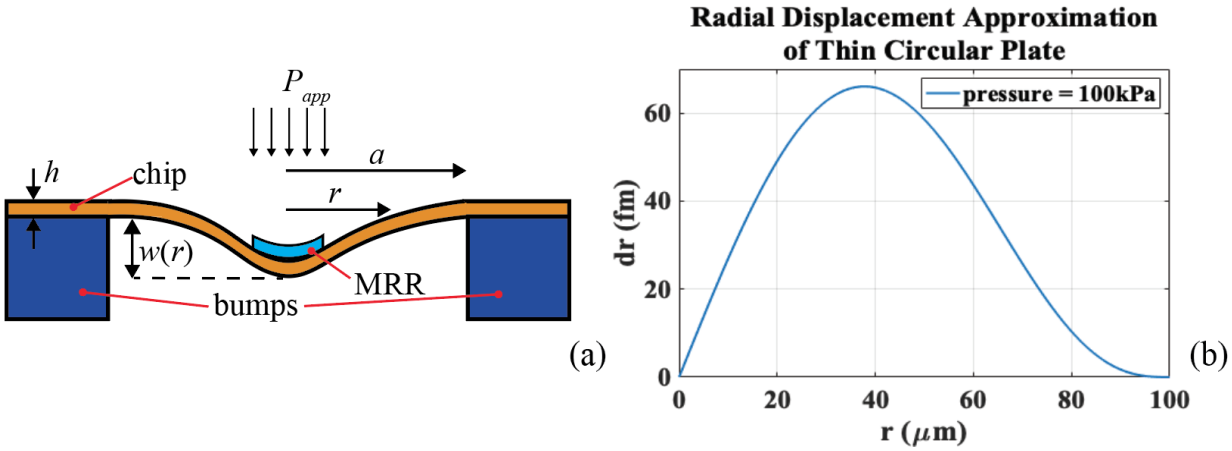

Figure 3.6: Ring Elongation: (a) Cross-sectional representation of a displaced thin film (die) clamped on the side (dimensions not drawn to scale), (b) Radial displacement as a function of the radial distance from the disk center under a uniform, 100kPa load.

To analytically evaluate the ring elongation effect we need to solve the Kirchhoff-Love isotropic plate equation, which in Cartesian coordinates is:

$$P_{app} = D\left(\frac{\partial^4 z}{\partial x^4} + 2\frac{\partial^2 z}{\partial x^2}\frac{\partial^2 z}{\partial y^2} + \frac{\partial^4 z}{\partial y^4}\right), \tag{3.16}$$

where P_{app} is the applied pressure, and D is the flexural rigidity of the plate given by:

$$D = \frac{Eh^3}{12(1-\nu^2)}, \tag{3.17}$$

where E is Young's Modulus of silicon, h the thickness of the plate, and ν Poisson's ratio.

The simplest model available to provide some analytical design intuition is that of a thin circular plate under uniform normal stress, undergoing small deflections. The plate is assumed clamped on the sides and thin (thickness $<$ 10×sensor pitch), both of which are reasonable in our application, where the post-substrate release die thickness is ∼12µm, the sensor pitch $>$ 150µm, and the die will be flip chip attached on a board and clamped via adhesive epoxy. Under these approximations and after transforming to cylindrical coordinates, a closed form solution for the axial displacement of the plate, $w(r)$, (also illustrated in Fig. 3.6a), and it's derivative, $\phi(r)$, can be found, [84, 85]:

$$w(r) = -\frac{P_{app}}{64D}(\alpha^2 - r^2)^2, \quad \phi(r) = \frac{dw}{dr} = \frac{P_{app}r}{16D}(a^2 - r^2), \tag{3.18}$$

where r is the radial distance from the center of the plate, and α is the plate radius, both of which are shown in Fig. 3.6 a. Subsequently, the radial displacement, dr, can be calculated

as:

$$dr = -w(r)\phi(r) \tag{3.19}$$

The radial displacement as a function of the radial distance for a 100μm radius plate, with an assumed effective $E = 50$GPa, $\nu = 0.17$ under a uniform, 100kPa load is plotted in Fig. 3.6 b. It can be seen that a displacement of ≈10fm occurs at 5μm away from the center of the unit element (a standard MRR diameter is 10μm). Plugging that displacement in Eq. 3.9 yields an elongation contribution to the intrinsic sensitivity of:

$$S_{int,el} = \frac{\partial \lambda_{res,el}}{\partial P_{app}} \frac{n_{eff}}{n_g} \Big(\frac{\lambda_{res}}{L} \frac{\partial L}{\partial P_{app}} \Big) \approx 3fm/MPa. \tag{3.20}$$

3.3.1.3 Opto-Elastic Effect

Any material under stress undergoes a change of its effective index of refraction, according to the optoelastic (or photoelastic) effect. It is commonly used in wafer warping testing, but has also been employed to detect ultrasound using the induced birefringence on a optical fiber with an embedded Fabry-Perot interferometer [54].

The photoelastic effect can be better understood through the relative dielectric impermeability tensor, and following the derivation of [86]:

$$\mathbf{B} = \epsilon_r^{-1} = \begin{bmatrix} B_{11} & B_{12} & B_{13} \\ B_{21} & B_{22} & B_{23} \\ B_{31} & B_{32} & B_{33} \end{bmatrix}, \tag{3.21}$$

which in symmetrical structures can be abbreviated as $\mathbf{B} = [B_{11}, B_{22}, B_{33}, B_{23}, B_{13}, B_{12}]^T$, while for isotropic materials it is $B_{ii} = n_{eff,i}^{-2}$.

Dielectric impermeability is used here since it changes linearly with the abbreviated strain tensor $\mathbf{S}$:

$$\Delta \mathbf{B} = \mathbf{p}\mathbf{S}, \tag{3.22}$$

where $\mathbf{p}$ is the photoelastic tensor, and is also rather simple for isotropic solids, thus yielding:

$$\begin{bmatrix} \Delta B_{11} \\ \Delta B_{22} \\ \Delta B_{33} \\ \Delta B_{23} \\ \Delta B_{13} \\ \Delta B_{12} \end{bmatrix} = \begin{bmatrix} p_{11} & p_{12} & p_{12} & 0 & 0 & 0 \\ p_{12} & p_{11} & p_{12} & 0 & 0 & 0 \\ p_{12} & p_{12} & p_{11} & 0 & 0 & 0 \\ 0 & 0 & 0 & p_{44} & 0 & 0 \\ 0 & 0 & 0 & 0 & p_{44} & 0 \\ 0 & 0 & 0 & 0 & 0 & p_{44} \end{bmatrix} \begin{bmatrix} \Delta S_{11} \\ \Delta S_{22} \\ \Delta S_{33} \\ \Delta S_{23} \\ \Delta S_{13} \\ \Delta S_{12} \end{bmatrix} \tag{3.23}$$

Also, we can write:

$$\Delta \mathbf{B_{ii}} = \frac{1}{(n_{eff,i} + \Delta n_{eff,i})^2} - \frac{1}{n_{eff,i}^2} \tag{3.24}$$

Combining Eqs. 3.23, 3.24, and making a binomial approximation on the first term of the RHS of Eq. 3.24 we obtain:

$$\begin{aligned}
\Delta n_{eff,1} &\approx -\frac{1}{2} n_{eff,1}^3 \big(p_{11} S_{11} + p_{12}(S_{22} + S_{33})\big), \\
\Delta n_{eff,2} &\approx -\frac{1}{2} n_{eff,2}^3 \big(p_{11} S_{22} + p_{12}(S_{11} + S_{33})\big), \\
\Delta n_{eff,3} &\approx -\frac{1}{2} n_{eff,3}^3 \big(p_{11} S_{33} + p_{12}(S_{11} + S_{33})\big),
\end{aligned} \tag{3.25}$$

where $n_{eff,1}$, $n_{eff,2}$, $n_{eff,3}$ are the unperturbed (not stressed) indices of refraction in the x, y, and z directions. The small changes approximation is justified, for two reasons: a) the moderate to low pressure amplitudes in our application in conjunction with the relatively high Young's modulus in silicon will lead to small strains, and b) the reported photoelastic coefficients of silicon are low.

Assuming light propagates in the z-direction of the silicon waveguide and we only apply a normal stress component in the y-direction, we can calculate $S_{11} = S_{33} = \nu \frac{P_{app}}{E}$, where ν is Poisson's ratio. Using $E = 140$GPa, and $\nu = 0.265$ in silicon and photoelastic coefficient values of $p_{11} = -0.09$, $p_{12} = 0.016$, from [87], we get $\Delta n_{eff,1} = \Delta n_{eff,3} = 2.7^{-12}$RIU/Pa for a 100kPa applied pressure wave. Converting that to intrinsic sensitivity through Eq. 3.9 we get:

$$S_{int,ph-el} = \frac{\partial \lambda_{res,ph-el}}{\partial P_{app}} = \frac{\lambda_{res}}{n_g} \frac{\partial n_{eff}}{\partial P_{app}} = 0.9 \frac{\text{fm}}{\text{kPa}}. \tag{3.26}$$

Similar conclusions regarding the minor impact of the opto-elastic effect on ultrasound sensing compared to waveguide deformation have been reached for polymer MRR platforms [88].

3.3.2 FEM Simulation

Previously in Section 3.3.1.2 we extracted a closed form solution for the ring elongation solving Eq. 3.16 for a thin circular plate. In reality though, our system is much more complicated and we would like to validate that indeed ring elongation is negligible, since it will be countering the primary wideband phenomenon of waveguide elongation. To this end, we setup an FEM simulation that takes into account more details of our sensor geometry and process technology. In that direction, our simulated unit cell consists of the BOX, the silicon waveguide, the nitrides, and the 12 metal layer stack-up which is 12.5um thick. To reduce the number of mesh points and get a reasonable simulation runtime, the unit cell area was set to a 250μm wide square, with the corners (where chip bumps will be located) treated as clamp positions. To get an impulse response, we simulated the effect of an incoming broadband Blackman wavelet centered at 80MHz with 100% fractional bandwidth, and 100kPa peak amplitude in OnScale. The results shown in Fig. 3.7 indicate that this effect is extremely narrowband with resonant peaks of 800kHz FWHM, and that the amplitude of this phenomenon is rather small, on the order of 10fm/100kPa, in good agreement with the

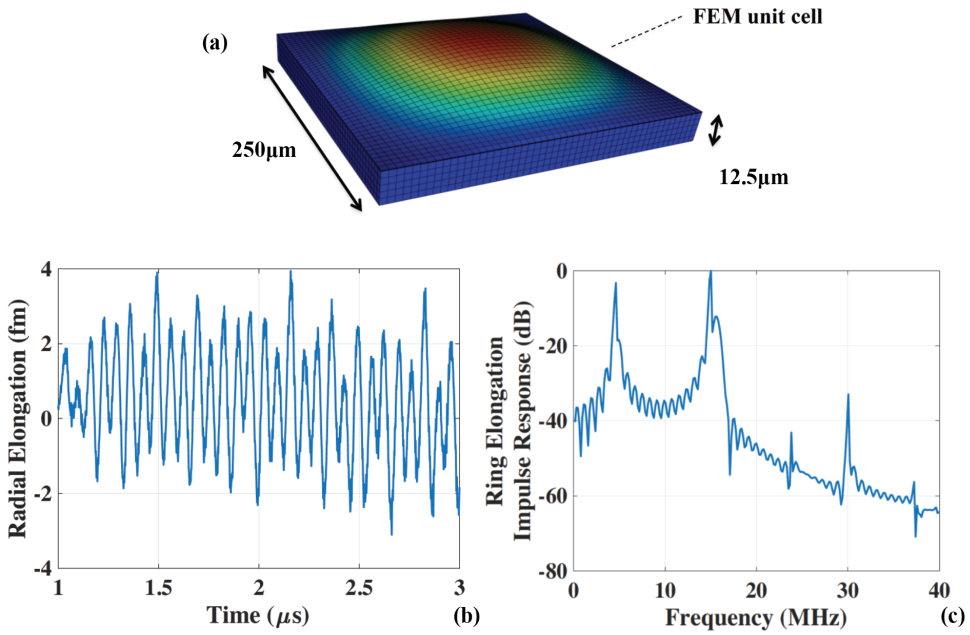

Figure 3.7: FEM simulations of Ring Elongation: (a) Unit element used in FEM simulations of waveguide deformation, (b) Time-Domain response of the unit cell, showing the radial elongation under a wideband 100kPa excitation, and (c) Frequency Domain response to the same excitation as in (b)

analytical solution, of a thin circular silicon plate. It should be noted that when interpreting these FEM results we assumed that the ring has a 10µm diameter and lies at the center of the element (which would account for the largest elongation).

3.4 Proof of Concept Measurements

To validate the theoretical analysis and expectations, and prove that ultrasound detection is possible in our 45nm CMOS SOI process, we used the experimental setup shown in Fig. 3.8. A piezoelectic transducer insonified the chip that was interrogated with a tunable CW laser source. Optical fibers were pigtailed onto the chip to avoid loss of coupling due to vibrations of the incoming pressure waves that could potentially interfere with the measurement. Finally, the output was read-out using a photo-detector with a TIA and an oscilloscope. Ring resonator banks from a photonic processor chip [89] were used in this proof-of-concept experiment.

Attempting to determine which of the transduction effects dominates the ring response and quantify the intrinsic sensitivity of our platform we first calibrated the PMUT with a

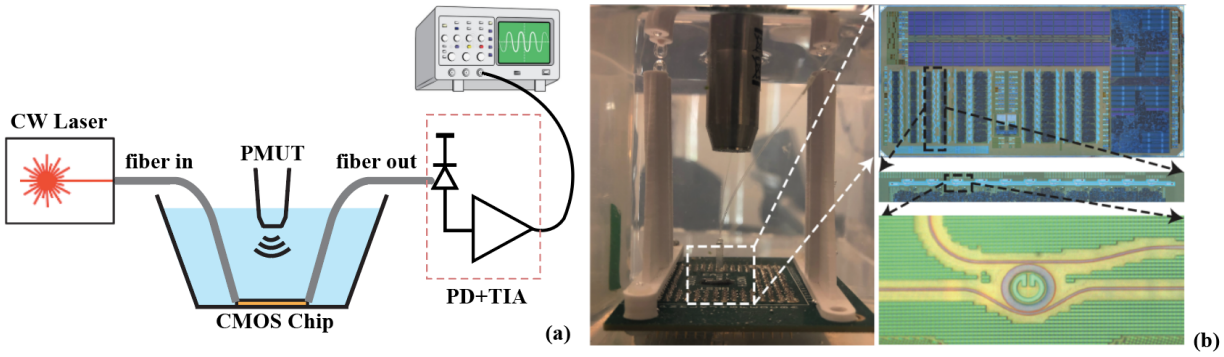

Figure 3.8: Experimental Setup: (a) Graphic representation of our experimental setup. (b) Zoom-in picture of the CMOS-SOI silicon photonic chip and the PMUT with insets presenting the die photo (top) and zoom-ins into the ring row tested (middle) as well as a single resonator disk (bottom).

commercial hydrophone placed at exactly the same distance as the CMOS chip in Fig. 3.9. Then we used the setup presented in Fig. 3.9 to detect PMUT generated ultrasound with an MRR. The hydrophone had positive polarity, meaning that a positive pressure would cause a positive voltage change at its output. At the same time, if a blue shift was observed in the ring response, this would indicate that a positive pressure would reduce the optical power and hence cause a negative voltage change at output of the TIA. Comparing the two received waveforms we observed that maximum correlation occurred between the inverted chip signal and the hydrophone signal, which is indication that a blue shift actually occurs and that the waveguide deformation effect is indeed dominant. This finding is encouraging since our analysis demonstrated that this effect is much more wideband [22] and in agreement with work done by other groups on MRR based ultrasound imaging [18]. To validate that the received signal was due to a resonant wavelength shift rather than vibrations of the input/output fibers we moved the laser off resonance and observed that the reception went to zero.

To identify the suitability of this platform for ultrasound sensing we used its intrinsic sensitivity to ultrasound as the induced resonant shift per applied pressure: $(\frac{\partial \lambda_{res}}{\partial P})$, as defined in Eq. 3.9. Given that traditional ultrasonic devices use PMUT sensors which output a voltage, transducer sensitivity is usually referred to in [V/Pa]. However, in optical MRR based ultrasound sensors there is one extra transduction step, so sensitivity can be broken down according to Eq. 3.11, which is repeated here for convenience:

$$S_{tot} = \frac{\partial V_{out}}{\partial P_{app}} = \frac{\partial \lambda_{res}}{\partial P_{app}} \frac{\partial T}{\partial \lambda_{res}} P_{opt} R_{PD} R_{TIA},$$

where V_{out} is the output voltage signal, P_{app} is the applied pressure, λ_{res} is the resonant

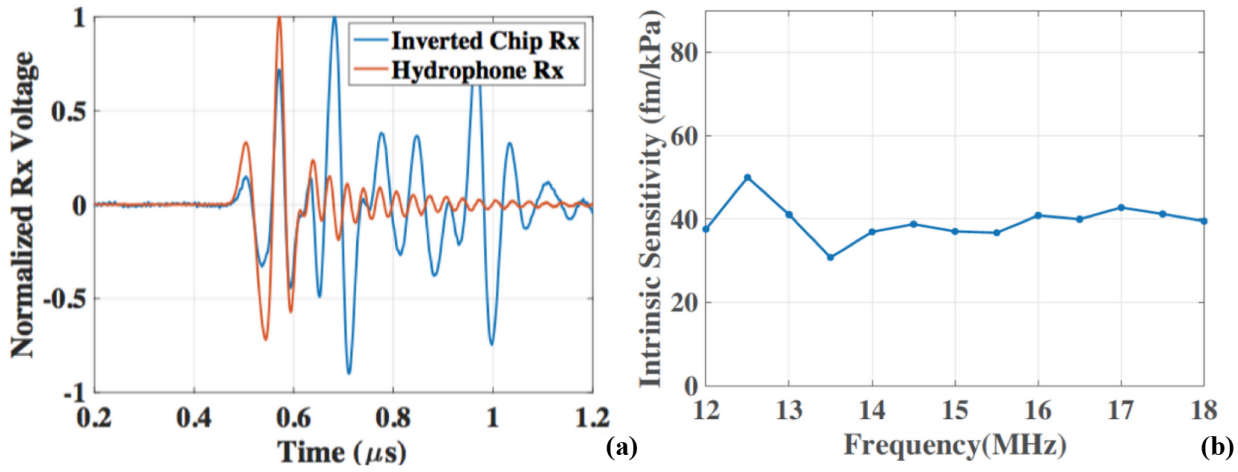

Figure 3.9: Experimental Results: (a) Frequency sweep of the chip response, (b) Received time-domain signals of hydrophone and chip (inverted)

wavelength, T is the normalized E-field amplitude of the optical wave at the MRR thru port, P_{opt} is the input laser power, and R_{PD}, R_{TIA} are the photodetector responsivity, and TIA gain respectively.

The piezo transducer used in this experiment was centered at 15MHz, with a fractional bandwidth of 40% and was calibrated over a 6MHz bandwidth using the same hydrophone as in the time-domain experiment. Measuring an optical transmission slope of $\partial T/\partial\lambda_{res} = 0.2\mu$W/pm, a combined PD-TIA gain of $R_{PD}R_{TIA} = 1.6$V/mW and an average response of $S = 12.6$mV/MPa, we calculated an average intrinsic sensitivity of $S_i = 39.6$fm/kPa, over the 6MHz bandwidth, a result comparable to another optical work with ultra-high bandwidth, using polymer MRRs [64]. This result verifies this platform is well-suited for ultrasound sensing and confirms the wide bandwidth expectation of the theoretical analysis.

The low [V/Pa] sensitivity recorded in this preliminary experiment is not a concern and has already been dramatically increased in the first ultrasound receiver EPSoC, which is presented in Chapters 4, 5, and is performing comparably to commercial hydrophone with measured sensitivity in the [mV/kPa] range. This improvement has primarily come from the use of next-generation grating couplers with sub-4dB loss [90], and integrated on-chip analog front-end with a high gain TIA [25].

3.5 Chapter Summary

Analytical expressions of the most important spectral characteristics for APF MRRs have been provided in Section 3.1 of this chapter, combined with a rudimentary sensitivity analysis. This analysis reached the conclusion that in realistic ring design, where the intrinsic

Q-factor of the MRR is set by the loss (assuming a certain technology and doping levels are selected), sensitivity is maximized when the ring is slightly undercoupled (half-critical coupling). The analysis performed can also be found in [79].

The MRR ultrasound sensing principle was subsequently introduced in Section 3.2. Useful sensitivity metrics (S_{int}, S_{phot}), relevant specifically to MRR-based ultrasound sensing that will be used throughout the manuscript were defined.

Section 3.3 presented an extensive theoretical analysis of the transduction mechanisms that induce the sensed resonant shift. This analysis concluded that when designing an array system with large number of MRRs we should attempt to maximize the resonant shift with respect to waveguide deformation if we wish to get high bandwidth. At the same time, counter-intuitive as this may sound, it will be important to keep the chip as clamped as possible, to maximize the sensitivity, since the ring elongation effect will be competing with the waveguide deformation.

Lastly, experimental evidence backing the theoretical and simulated results, and validating the suitability of our "zero-change" CMOS-SOI process for ultrasound sensing were provided in Section 3.4.

Chapter 4

Realization of Electronic-Photonic Ultrasound Receiver Array

Power and area minimization without loss of image quality constitutes the main pain-point of modern endoscopic ultrasound imaging systems based on conventional sensing techniques as discussed in Chapter 2. In order to acquire high resolution volumetric images, next-generation ultrasound imaging systems need to integrate thousands of sensing elements in dense 2-D arrays of piezoelectric or capacitive micromachined ultrasound transducers (PMUTs and CMUTs) inside the device's probe-head. The size of these next-generation endoscopic probes is limited by safety regulations to 1cm^3 for the probe-head and $5-7$mm for the probe tube diameter [33]. At the same time, to avoid formation of grating lobes the sensor pitch should be limited to $< \lambda/2$, which for 5MHz ultrasonic signals is 150μm. Combining these conditions translates to arrays with ∼1000 elements, which are practically impossible to fan-out electrically using micro-coax cables while complying with the aforementioned probe diameter limit. Attempting to reduce the number of channels locally requires co-integration of the sensors with pitch-matched, low-noise ASICs, operating under a tight power and area envelope.

Moving ultrasound sensing to the photonic domain offers an efficient, elegant solution to these challenges. Implementations based on optical sensors can eliminate the electrical cabling, replacing micro-coax cables with much thinner optic fibers, while consuming minimal power [20, 16]. Microring resonator sensors are an ideal candidate for endoscopic applications since they combine all the advantages of optical ultrasound sensing with compact footprints (down to 10μm), ease of scalability to large 2-D arrays, and competitive sensitivity [23, 24]. However, as mentioned in Chapter 2, a robust and efficient resonance tuning mechanism is essential for their use in a real-time phased array, an aspect lacking from MRR-based ultrasound imaging systems presented to-date.

In this chapter, we introduce the design methodology of a first-of-its-kind Electronic-Photonic System-on-Chip (EPSoC) that achieves real-time simultaneous interrogation of multiple MRR sensors arrayed in a 2-D matrix. This is primarily enabled by utilizing a fully integrated electronic-photonic biosensing platform in a high volume advanced CMOS-

SOI process. Our proof-of-concept EPSoC prototype is fabricated in the GlobalFoundries 45nm SOI CMOS technology node, which allows monolithic integration of photonic devices (waveguides and planar MRRs) with high-performance CMOS circuits on the same chip. This tight co-integration of photonics and electronics results in efficient and robust thermal control of the MRR resonant wavelength. To fully exploit this unique capability we introduce a dual-chip sensing receiver architecture, which enables ultra-low power and area operation, while maintaining a very low overall system form-factor, compatible with the specifications of modern endoscopes [33]. This first EPSoC prototype can flexibly be configured as a sensing or as a receiver chip and it supports an 8×4 sensor array, with each sensing unit including a variable gain signal conditioning stage, followed by a successive approximation register (SAR) analog-to-digital converter (ADC), while on-chip serialization and CML output driver stages have also been implemented.

The remainder of this chapter is organized as follows: Section 4.1 outlines the target specifications of next-generation ultrasound endoscopes, while Section 4.2 presents the system architecture that enables our EPSoC to meet these specifications. Section 4.3 analyzes the circuit design choices and implementation details of both the analog front-end and the digital back-end. Section 4.4 describes the procedure of automatically generating the photonic top level layout using the Berkeley Photonics Generator (BPG) [72, 91], as well as the strategy followed to co-integrate the CMOS sensing element with the photonic devices into an EPSoC. Finally, Section 4.5 summarizes the chapter.

4.1 System Specifications

- **Power Consumption:** Ultrasound imaging probes intended for endoscopic purposes need to abide by a 1W total power consumption limit [21]. Assuming that 50% of this power budget is allocated for transmit and 50% for receive, dense 2-D array probes with $\sim$ 1000 sensing elements need to ensure the power consumption is maintained **below 0.5mW per receiver**. It should be noted that only one such work employing PMUTs as sensors has so far been reported to the best of the author's knowledge [32].

- **Area:** Given that the upper area limit of the whole area is set by practical constraints of the application to 0.5mm^2, the element pitch will determine two system attributes: a) the total number of sensors integrated in the probe-head, and b) the maximum ultrasonic frequency and that can be sensed without spacial aliasing (i.e. grating lobes). Having more sensors per unit area is extremely beneficial for the array signal-to-noise ratio (SNR). As it will be analyzed in Section 4.3 most of the noise sources have a white profile, meaning that the overall array SNR will improve as a factor $\sqrt{N}$, where N is the number of sensors. On the other hand, increasing the frequency of ultrasound improves the axial resolution and provides more structural details of the imaged object. This improvement of the non-aliased field-of-view (FOV) over frequency, with reducing

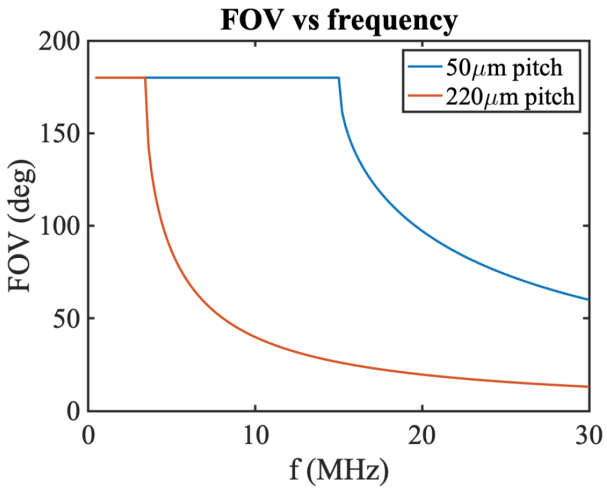

Figure 4.1: Field of view vs frequency for sensor pitch values of 220µm and 50µm.

sensor pitch is plotted in Fig. 4.1, and calculated using:

$$FOV = 2sin^{-1}\Big(\frac{\lambda}{2d}\Big), \tag{4.1}$$

where d is the sensor pitch.

Additionally, the inherent sensitivity - bandwidth trade-off in PMUT and CMUT sensors has problematic implications for systems based on these conventional transducers. First, the benefit of improved SNR that comes with size scaling and increased sensor count will be offset by sensitivity degradation. Second, the co-integrated receiver circuit design will face even more aggressive pitch matching and power constraints. This further underlines the superiority of a system based on miniaturized optical sensors.

- **Noise Equivalent Pressure (NEP):**

  The integrated noise equivalent pressure of a system can be calculated as a function of the sensitivity S and the integrated noise N over the bandwidth of the system (which should be equal to the bandwidth of the signal of interest to filter out high frequency noise), where both S and N are estimated at the same port of the transduction chain (input or output). Here we refer the current noise density at the input of the TIA, $\overline{i_n^2}$ back to pressure through the intrinsic and photonic sensitivities:

$$\text{NEP[kPa]} = \frac{N}{S} = \frac{\sqrt{\overline{i_n^2} \cdot BW}\text{[A]}}{S_{int}\text{[fm/kPa]} \cdot S_{phot}\text{[mW/fm]} \cdot R_{PD}\text{[A/mW]}} \tag{4.2}$$

  Taking into account that the endoscopic ultrasound pressure amplitudes range is approximately (10kPa, 2-3MPa), while the photoacoustically generated pressures range

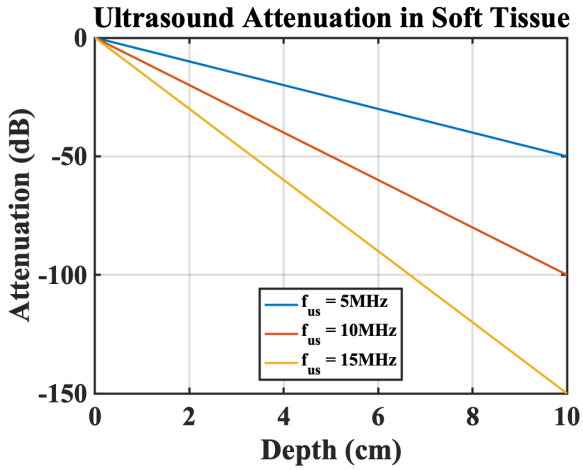

Figure 4.2: Attenuation of ultrasound amplitude in tissue over distance for various excitation ultrasound frequencies.

is about (10Pa, 1-2kPa) [92] we set the target NEP to 2kPa such that we are able to potentially target both endoscopic and photoacoustic pressures. A low NEP can enable detection of high frequency photoacoustic signals that are quickly attenuated in the body, and also provide great absorption based contrast or pulse-echo images from deeper in the body. In both cases though it needs to be combined with a sufficiently high dynamic range (DR) to produce a useful image [43].

- **Dynamic Range (DR):** As it propagates through tissue, ultrasound is attenuated due to both scattering and absorption. Absorption, which is the dominant loss mechanism has an attenuation coefficient in soft tissues is ∼1dB/cm/MHz [93], implying that the signal strength reaching the detector will be depth dependent. This depth dependent attenuation is plotted in Fig. 4.2 for ultrasonic signals of 5, 10 and 15MHz. At the same time, the typical dynamic range of pulse-echo ultrasound experiments is about 80dB, 40dB of which originate from this depth dependent attenuation, assuming an imaging depth of 4cm (which corresponds to 8cm ultrasound propagation distance accounting for round trip loss). Thus, the electrical DR of the front-end (DR at maximum gain setting plus 24dB of gain programmability) will be designed for ∼40dB. At the same time, a current mirror DAC will offer an additional 30dB of input DR, as will be discussed in Section 4.3.

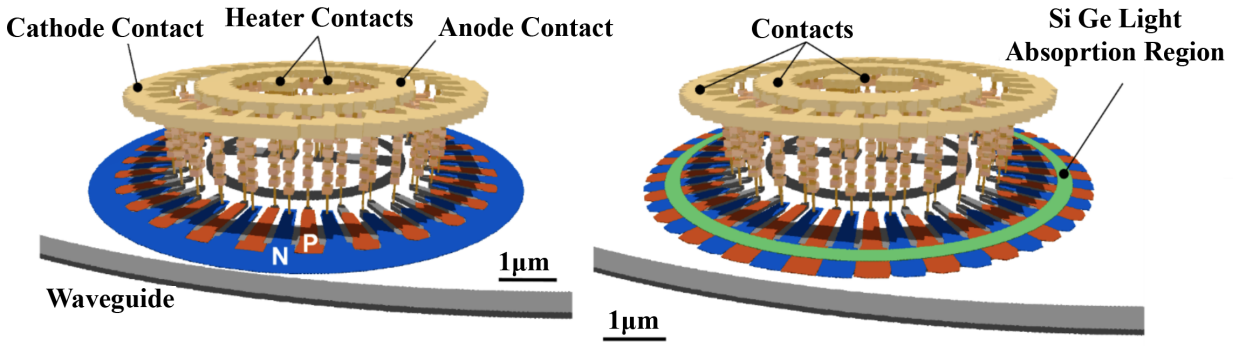

Figure 4.3: 3-D renderings of spoked-rings in our "zero-change" 45nm monolithic platform: sensor MRR (left) and PD MRR with responsivity enhancement SiGe absorption region (right), from [94]. Embedded heater contacts as well as anode and cathode contacts are also labeled.

4.2 System Architecture

4.2.1 Remoted Optical Ultrasound

Substituting PMUT and CMUT transducers measuring > 150µm pitch with 10µm diameter MRRs yields large sensing area benefits. Moreover, replacing the complex, per pixel pitch-matched, and 3-D integrated receiver front-end, with digital logic that precisely tunes the MRR resonance and is co-integrated with the sensors on a single die, significantly reduces system complexity, while keeping the sensing unit area minimal. Efficient active tuning of the ring resonance [70, 23] is enabled by heaters embedded in the internal cavity of the MRR. 3-D renderings of the layouts of the 10µm diameter sensor and PD MRR designs in our technology are shown in Fig. 4.3, indicating the heater, anode and cathode contacts. Taking advantage of the strong thermo-optic effect in silicon, and the monolithic integration of electronics and photonics these heaters achieve a record-low tuning efficiency of 0.68pm/µW. This is a key system attribute that ensures sensing unit power consumption will be kept well within the safety limits.

Using MRRs as ultrasound transducers also offers the advantage of encoding the sensing information in the optical rather than the electrical domain, which in turn enables us to use optic fibers instead of the much thicker micro-coax cables for I/O. Thus, the electrical cabling can be limited to only a few power and scan signals, alleviating the wiring congestion in the probe tube. Apart from eliminating the need for pitch matched front-end design, remoting the receiver allows the power consumption specification to be relaxed for this part of the system. However, in order to build a self-contained system that can be used in a portable device setting, miniaturization of the receiver is also important. A dedicated receiver chip that can simultaneously receive and process the information from multiple optical channels

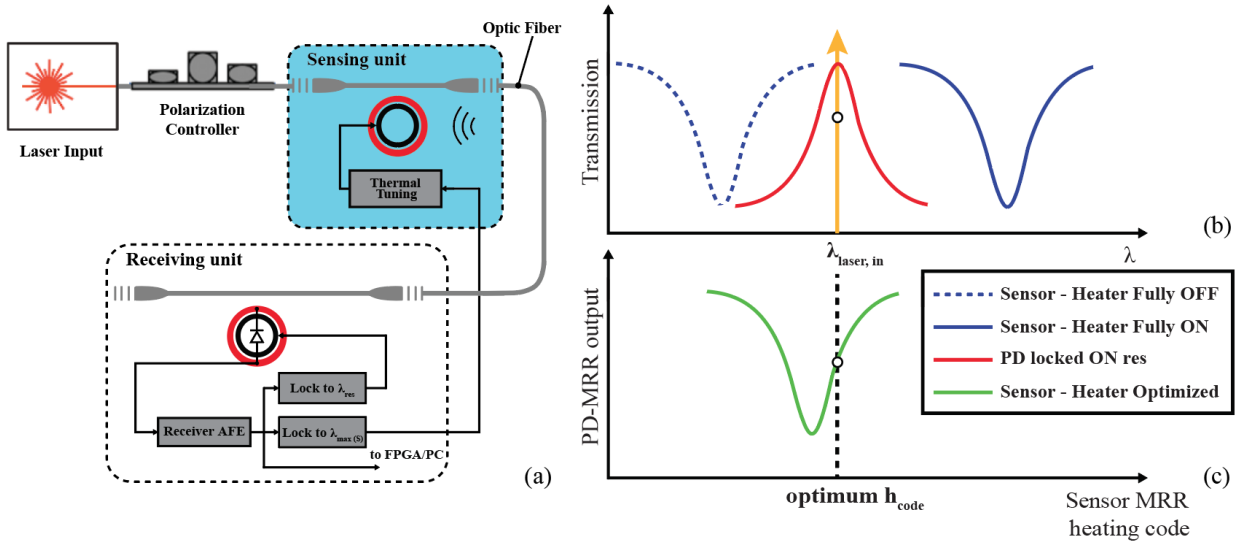

Figure 4.4: (a) Schematic diagram of remoted optical ultrasound sensing scheme, and optimization of PD and sense MRR heater codes for remote ultrasound sensing. (b), (c) After an initial calibration step, the heating code of the sensor ring is set such that it is biased on the stable side of the ring Lorentzian. The PD ring's resonance is locked onto λ_{in}, such that the circulating power in the ring, and thus the responsivity is maximized.

(which in the case of 3-D endoscopes can be $>$ 1000) would enable a much simplified PoC system, compared to having a discrete receiver and ADC per sensing channel.

Towards that end, we implemented a complete receiver unit in our zero-change platform. It consists of a photodetector MRR (PD-MRR) with an additional SiGe doping layer employed to enhance responsivity [95], in close proximity to the control, signal conditioning, digitization and serialization circuitry, all contained in a $190 \times 220\mu m^2$ area. Even though this work focuses on endoscopic ultrasound applications operating in the 5MHz range, the low input parasitics that come with monolithic integration, ensure that the front-end has sufficient bandwidth ($>$ 20MHz) even for photoacoustic types of applications, potentially permitting this platform to be used for multi-modal imaging purposes in the future.

The described remoted optical ultrasound sensing scheme is illustrated in Fig. 4.4 (a) for a single sensor-receiver pair. Initially, the ***PD-MRR*** resonance is matched to the wavelength of the incoming laser light, using a digitally controlled thermal tuning locking loop. This ensures maximum PD-MRR responsivity since most of the available optical power circulates in the ring when on resonance. Subsequently, the heater code of the ***sensor MRR*** is swept and its Lorentzian is captured using the ***PD-MRR***, as shown in Fig. 4.4 (b). To maximize this sensing scheme's sensitivity the heater code of the ***sensor MRR*** is selected such that its maximum slope point is aligned to the wavelength of the input laser light, as shown in

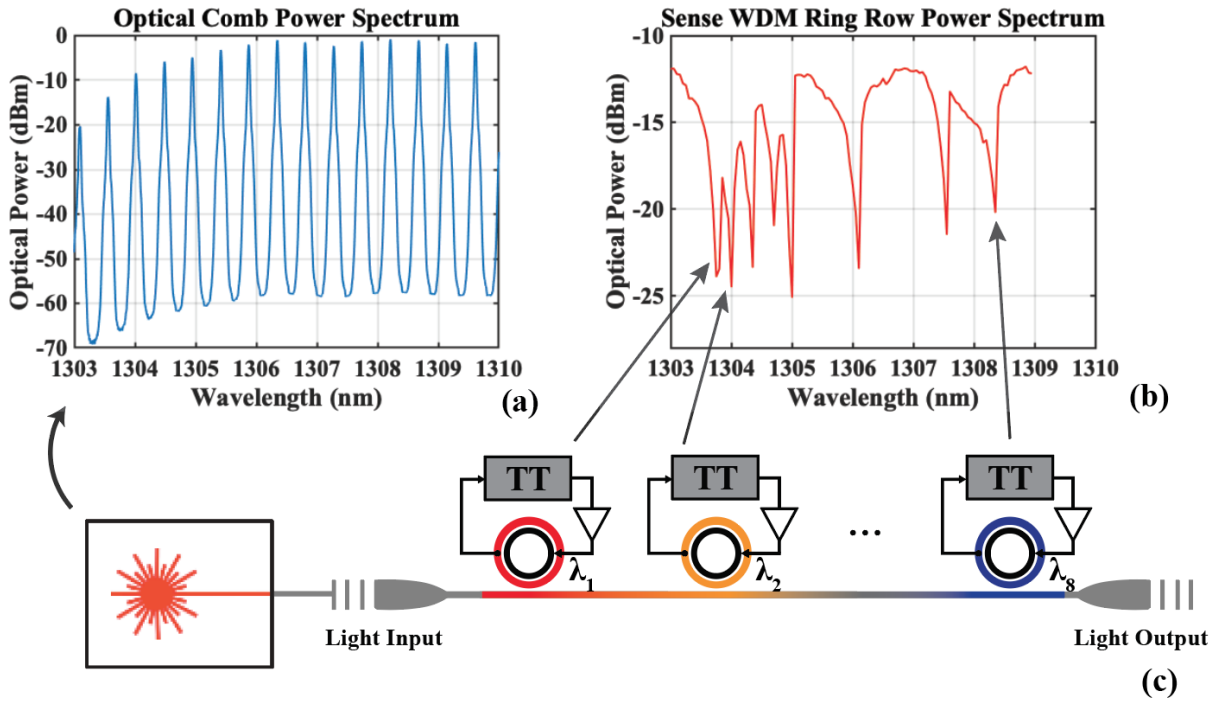

Figure 4.5: Illustration of the need for active resonance tuning for WDM interrogation. Measured optical power spectrum of: (a) the available comb laser, (b) an on-chip sensor WDM ring row. (c) Schematic representation of a WDM ring row consisting of multiple MRRs coupled onto the same silicon waveguide and interrogated by a comb laser input.

Fig. 4.4 (c). This concept can be extended to multiple sensor-PD MRR pairs in an array as illustrated in the following section.

4.2.2 WDM Interrogation & Dual-Chip 2-D Beamformer

Apart from remoting the power and area hungry receiver circuitry, combining optical MRR-based transducers with active resonance tuning offers the capability of simultaneously interrogating multiple MRRs coupled onto the same waveguide in a WDM fashion using a fixed wavelength multiple channel comb laser, as presented in Fig. 4.5. This translates to a reduction of fiber channel count for I/O proportional to the number of optical modes available on the comb laser with zero power and area overhead. In our first generation EPSoC, 8 MRRs are coupled onto the same waveguide. Simple 8-channel integrated multi-wavelength laser diodes have recently been reported [96] and could be used with this EPSoC, further simplifying the overall system and minimizing its form factor, while $>$ 16-λ combs are also available [97], leading to a further fiber-count reduction. The concept of WDM interrogation of multiple MRRs coupled onto the same waveguide is shown in Fig. 4.5. Note that

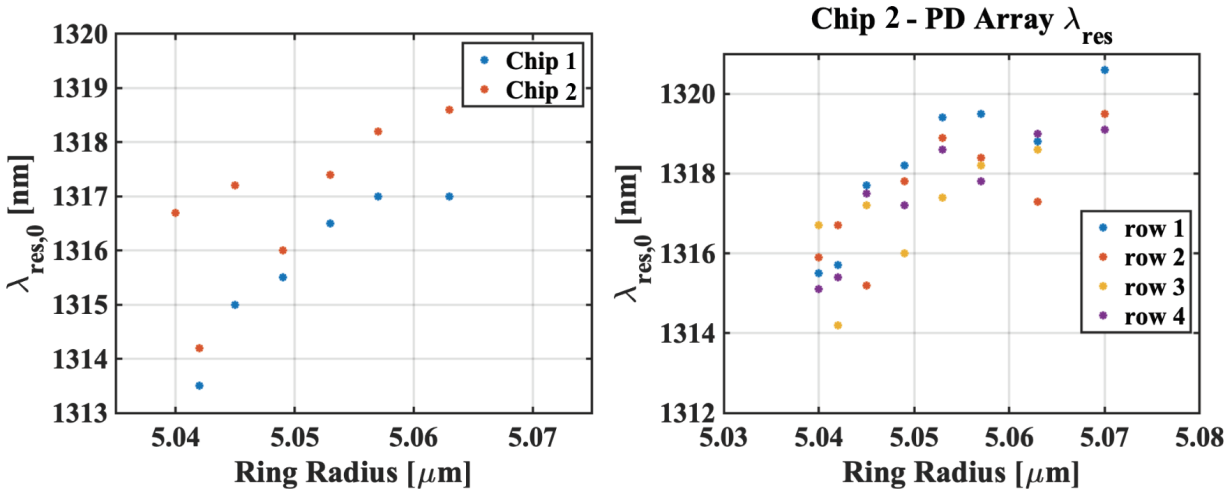

Figure 4.6: Need for active resonance tuning: variations in the unheated resonant wavelengths, $l_{res,0}$ of rings in the same locations on different chips (left), and between rings with the identical drawn radius on different WDM rows of the same chip (right).

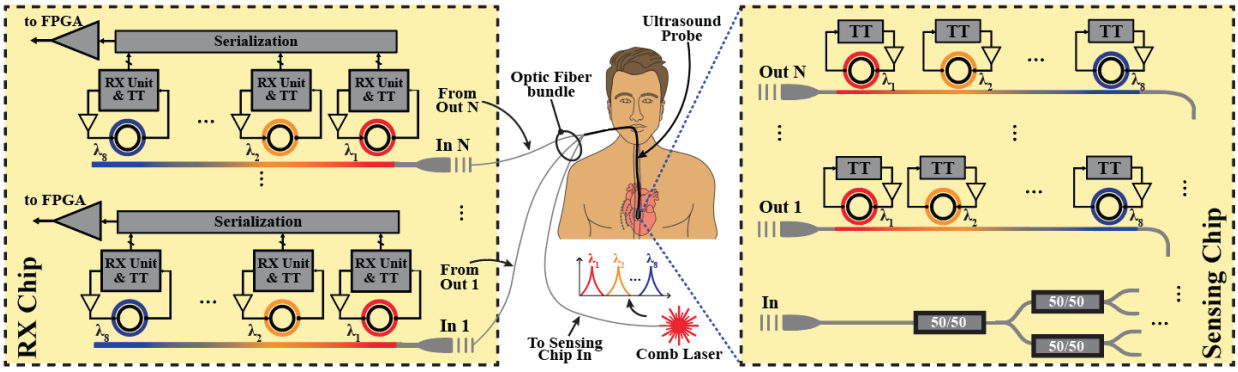

Figure 4.7: Dual-chip system architecture illustrating the remoted optical ultrasound beamforming array concept for power and area minimization.

the remoted optical ultrasound sensing described in Section 4.2.1 is compatible with WDM sensing, simply by applying the locking algorithm to multiple MRRs at the same time.

The necessity for an active thermal tuning mechanism is underlined in Fig. 4.6, where the exact location of the native, untuned resonant wavelengths, $\lambda_{res,0}$, is shown to vary significantly even among devices with the same drawn characteristics due to process variations. This is more pronounced across different chips but occurs even for rings on different locations on the same chip.

The original goal of implementing a dense 2-D MRR sensor matrix can finally be achieved by arraying multiple identical WDM ring rows in parallel on a sensor EPSoC. Utilizing an area efficient multi-mode interferometric (MMI) splitter tree, the comb laser input is distributed into the WDM row replicas. Splitting the optical power on chip further reduces the cable count, allowing us to interrogate the entire 2-D array with a single input fiber. The conceived system architecture implemented on this EPSoC is shown in Fig. 4.7. A sensor chip containing only an MMI splitter tree, high quality factor (and consequently high sensitivity) sense MRRs and thermal tuning circuitry will be placed at the probe tip, where power and area minimization are critical, while a receiver chip with PD-MRRs, analog receivers, digital tuning control logic, and serialization, will recover the ultrasound signal and send it to an FPGA that will perform beamforming and image processing.

To prove the remoted ultrasound concept in a single tape-out, the implemented prototype EPSoC is designed to be configured either as a sensing or as a receiving chip. Also, in order to enable monitoring and debugging of the tuning loops of the sensor MRRs and to streamline the design process, the same mixed-signal block is used to interface with both the sense and PD MRRs constraining the pitch to 220μm. This should be sufficient to enable a 180° field of view (FOV) at 3.6MHz and up to 85° FOV at 5MHz, without the formation of grating lobes, as shown in Fig 4.1. However, the sensing area that will eventually be required is $< 0.01\text{mm}^2$ per sensing element, as proved by the performed experiments. This translates to a much higher sensor density and an FOV of 180° up to 15MHz, assuming a sensor pitch of 50μm.

Quantifying the integration density that an optical sensor approach offers, fiber assemblies with 61 channels packaged in 330μm × 280μm area have been reported [98]. Combined with a high input power comb laser we can use an MMI splitter tree to split a single input into 60 ring rows on-chip. Assuming 16 MRRs per WDM row, 960 sensors can be simultaneously interrogated with a 2.8mm diameter fiber bundle. This is in stark contrast to the high-density micro-coax cable counterpart where only 192 cables can fit in a 7.5mm diameter bundled cable [32, 99].

4.3 Electrical Sensing Unit Design

Fig. 4.8 shows the schematic of a receiver unit quad. It consists of a dedicated mixed-signal block for each sensor, with a TIA, followed by a pre-amplifier and a 9-b successive approximation register (SAR) ADC that digitizes the received ultrasound signal at 50MSa/sec. The outputs of 4 blocks are then serialized and transmitted to an FPGA for post-processing using a current mode logic (CML) output stage that ensures sufficient signal swing.

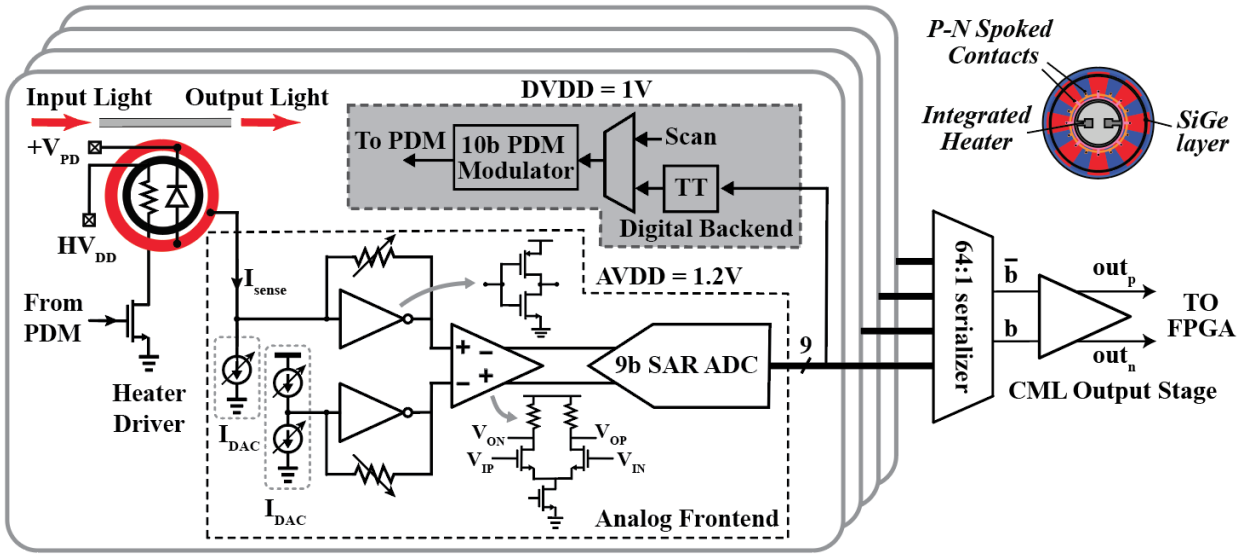

Figure 4.8: Schematic diagram of the receiver unit quad illustrating the various circuit sub-blocks.

4.3.1 Analog Front-End

4.3.1.1 Transimpedance Amplifier (TIA) and Preamplifier

A resistive feedback TIA shown in Fig. 4.9 is used in the core of this amplifier to convert the sensor input signal from the current to the voltage domain for further processing. This stage needs to provide high DR as explained in Section 4.1, while ensuring a low noise operation, such that the target NEP specification is met. Alternative TIA topologies such

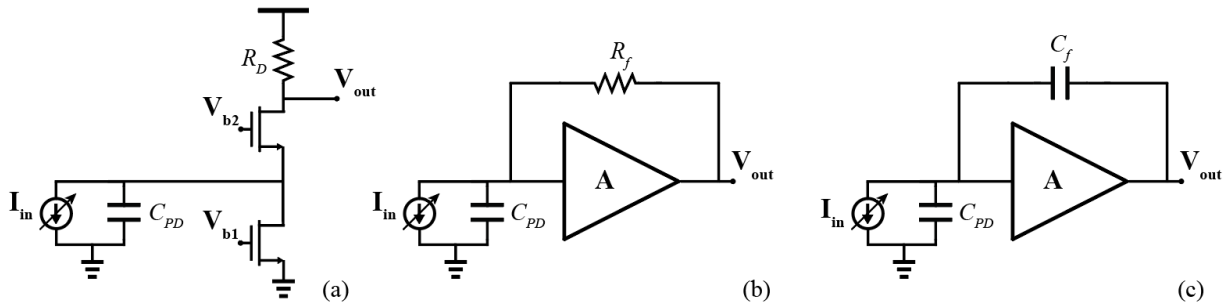

Figure 4.9: Schematic diagram of (a) common-gate, (b) resistive, and (c) capacitive feedback TIA topologies.

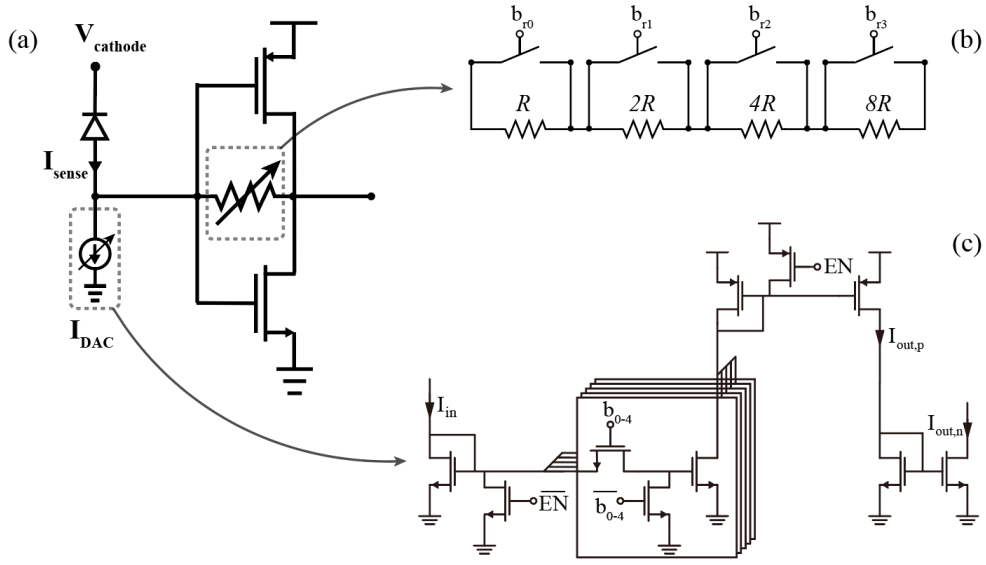

Figure 4.10: (a) Schematic diagram of the inverter based TIA with call-outs of: (b) Programmable resistive feedback network, and (c) Bleeder I_{DAC}s adjusting the bias point.

as the common-gate [100, 101] or capacitive feedback TIA [102, 103] have been proposed in literature, and are also shown in Fig 4.9. The common-gate TIA is known to escape the gain-BW trade-off and has been shown to achieve very low NF. However, this topology comes with limited headroom, which also implies that the aforementioned NF is achieved for relatively low DR values. On the other hand, as analyzed in [41] the capacitive feedback TIA has the best NF, especially for high DR values at the expense of additional area due to the use of large feedback capacitors. Lastly, the resistive feedback TIA constituted the best solution when moderately high DR and competitive noise performance need to be combined with a reasonable analog front-end (AFE) area. Since this first prototype will include a receiver unit abutted to both the sensor and the receiver sites, and our DR specification will be somewhat relaxed by having a programmable gain and bleeder current DACs we chose to not sacrifice any more area, and use a resistive feedback TIA topology.

The exact TIA implementation, shown in Fig. 4.10, has a single inverter cell in its core, which gives the additional benefit of design simplicity, area minimization, and current efficiency. Gain programmability is achieved with a 4-bit binary-weighted resistive network, which offers 24dB of extra DR, in 6dB gain steps. The resistor values ranged from 50kΩ to 800kΩ, which ensures that we will be able to detect the target NEP of 2kPa using the highest gain setting, and that resistor thermal noise is negligible, even for the lowest gain setting.

To cancel the strong background photocurrent, I_{sense}, of the PD-MRR, current digital-

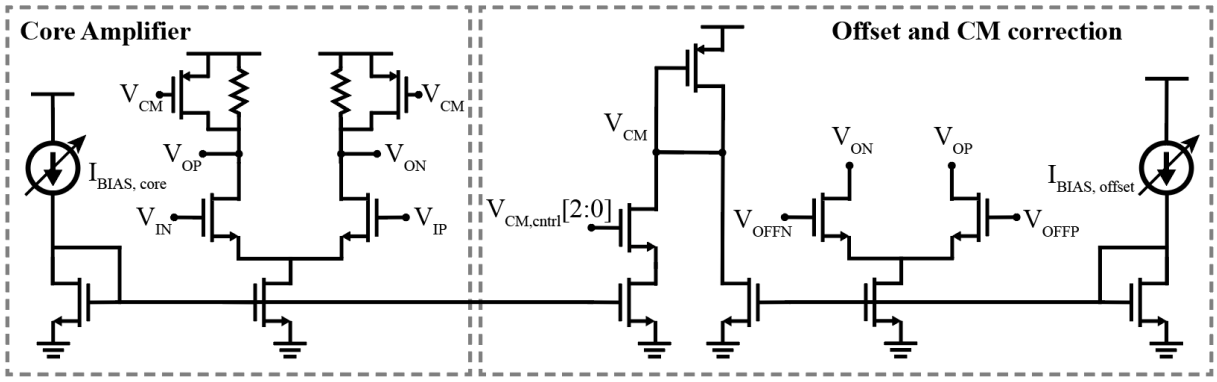

Figure 4.11: Schematic diagram of the preamplifier circuit with CM control and offset correction circuitry also shown.

to-analog-converters (I_{DAC}s), have been connected to the input node of the TIA. Two 5-b pull I_{DAC}s have been added, to do fine and coarse bias adjustment respectively. The I_{DAC}s have been automatically generated using the Berkeley Analog Generator (BAG) framework [104] and their schematic is also shown in Fig. 4.10. They have a global enable and the output can be configured to be push or pull ($I_{out,n}$ or $I_{out,p}$) by specifying the corresponding parameter in the layout generation code. The fine I_{DAC} has a minimum step of $\sim$ 120nA ensuring that we will able to fine tune the output common-mode voltage with a step < 0.1V for the highest gain setting ($800\text{k}\Omega \cdot 120\text{nA}$). The coarse I_{DAC} has a minimum step of 4μA, and can be used to switch between different modes of operation. This switching is done by adjusting the input optical power, and consequently S_{phot}, so that stronger or weaker signals can be detected. In such scenarios, the value of the background current that needs to be cancelled should be accordingly adjusted. This 5-b coarse tuning offers an additional 30dB of DR to the TIA input.

A pseudo-differential replica of the TIA is implemented in order to suppress supply noise and enhance the circuit power supply rejection ratio (PSRR). To bias the replica two 3-b push-pull I_{DAC}s following a design similar to the one shown in Fig. 4.10. A fully differential preamplifier performs single-ended to differential conversion and adds another 6dB of gain to the overall amplification chain. The preamp is depicted in Fig. 4.11. Its core consists of a resistively loaded differential pair, while common-mode (CM) control and offset correction blocks are also implemented. Output CM control is performed by a diode-connected device controlling the gates of PMOS bleeders, and has 8 settings (3-b programmability) to ensure the common mode input to the ADC is at the correct voltage level. A single-bit offset correction is done through NMOS bleeders with their drains connected directly to the amplifier output. The preamplifier output is then fed into an 9-bit SAR ADC, which was also implemented using BAG and Laygo [105], and whose design was ported to 45nm GF

process from [106]. The number of ADC bits was selected such that the quantization noise does not dominate the noise budget. With 9 bits the input referred quantization noise will be comparable to the worst case thermal noise from the feedback resistor, while the theoretical SNDR will be ∼56dB, well above the specified DR of ∼40dB.

4.3.1.2 Noise Analysis

The main noise contributors in our resistive feedback TIA front-end will be shot noise, thermal noise from the bleeder $\mathrm{I_{DAC}}$s and the feedback resistor, input referred noise of the TIA, as well as quantization noise from the ADC. These are mathematically described as:

$$\overline{i^2_{n,shot}}(f) = 2qI_{PD} = 2qR_{PD}P_{circ}, \tag{4.3}$$

$$\overline{i^2_{n,th,\mathrm{I_{DAC}}}}(f) = 4kT\gamma g_{m,eff}, ^* \tag{4.4}$$

$$\overline{i^2_{n,th,R_f}}(f) = \frac{4kT}{R_f}, \tag{4.5}$$

$$\overline{i^2_{n,th,MOS}} = \frac{4kT\gamma}{g_{m,in}}(2\pi C_{in})^2 = \frac{4kT\gamma}{g_{m,in}}\big(2\pi(C_{PD}+C_g)\big)^2, \tag{4.6}$$

$$\overline{i^2_{n,q}}(f) = \frac{\Delta^2}{12R_fG_{preamp}}, \tag{4.7}$$

where $q = 1.6 \cdot 10^{-19}$C is the unit charge, I_{PD} is the photodetector current, R_{PD} is the photodetector responsivity, P_{circ} the optical power circulating in the PD-ring, k Boltzmann's constant, T the temperature, γ the MOSFET white noise parameter, $g_{m,eff}$ the "effective" $\mathrm{I_{DAC}}$ transistor transconductance, R_f the TIA feedback resistor, $g_{m,in}$ the transconductance of the input pair, C_{PD}, C_g the PD and inverter gate capacitances respectively, Δ the ADC input step, and G_{preamp} the preamplifier gain.

At the same time, the sensor input signal, I_{sense}, can be written as:

$$I_{sense} = S_{int}S_{phot}R_{PD}P_{app} = S_{int}P_{opt}\frac{Q}{\lambda_{res}}R_{PD}P_{app}, \tag{4.8}$$

and the SNR will be:

$$SNR = \frac{\left(\frac{1}{2\sqrt{2}}I_{sense,pp}\right)^2}{I^2_{n,tot}\cdot BW} = \frac{\left(\frac{1}{2\sqrt{2}}S_{int}P_{circ}\frac{Q}{\lambda_{res}}P_{app,pp}\right)^2}{\left(2qR_{PD}P_{circ} + 4kT\gamma g_{m,eff} + \frac{4kT}{R_f} + \frac{\Delta^2}{12R_fG_{preamp}}\right)\cdot BW}, \tag{4.9}$$

$^*g_{m,eff}$ represents an "effective" transconductance, used to lump the thermal noise of all the transistors of the $\mathrm{I_{DAC}}$s in one parameter, extracted through simulation.

Table 4.1: Typical and Simulated Front-End Parameters

Parameter	Value
P_{opt}	100μW
P_{circ}	50μW
R_{PD}	0.5A/W
C_{PD}	30fF
C_g	$<$ 1fF
γ	2/3
$g_{m,eff}$	1.7mS
R_f	(50-800) kΩ
f_{us}	5MHz
BW	(3-7) MHz (80% fractional)
S_{int}	40fm/kPa
Q-factor	10^4
P_{app}	2kPa

where we have added the noise variances to get the total noise, since the noise sources are uncorrelated. The value of the input referred noise of the TIA gate transistors, $\overline{i^2_{n,th,MOS}}$, can be neglected since in our case where C_{PD} is rather small due to the monolithic integration. Also note that in the estimate of I_{sense}, we have used the power incident upon the ring to estimate the slope of the Lorentzian, whereas to find the background DC photocurrent in Eq. 4.3, we will be assuming that the ring is biased at -3dB extinction.

Expected parameter values for input optical power, and PD responsivity, and capacitance, along with simulated ones for transistor parameters (γ, g_m) are tabulated in Table 4.1. Using

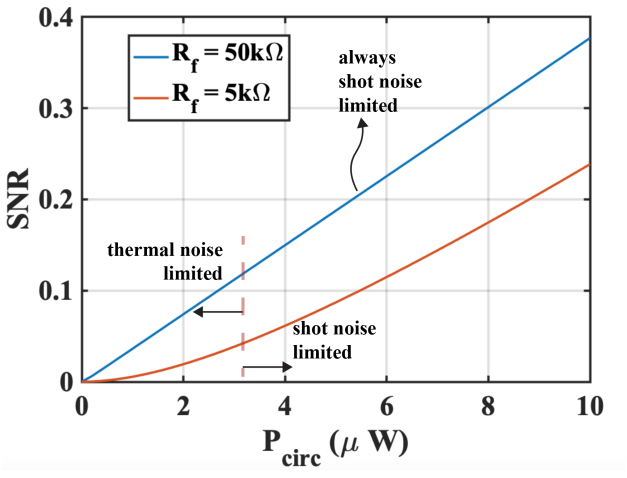

Figure 4.12: SNR vs P_{circ}, indicating shot and thermal noise limited regimes.

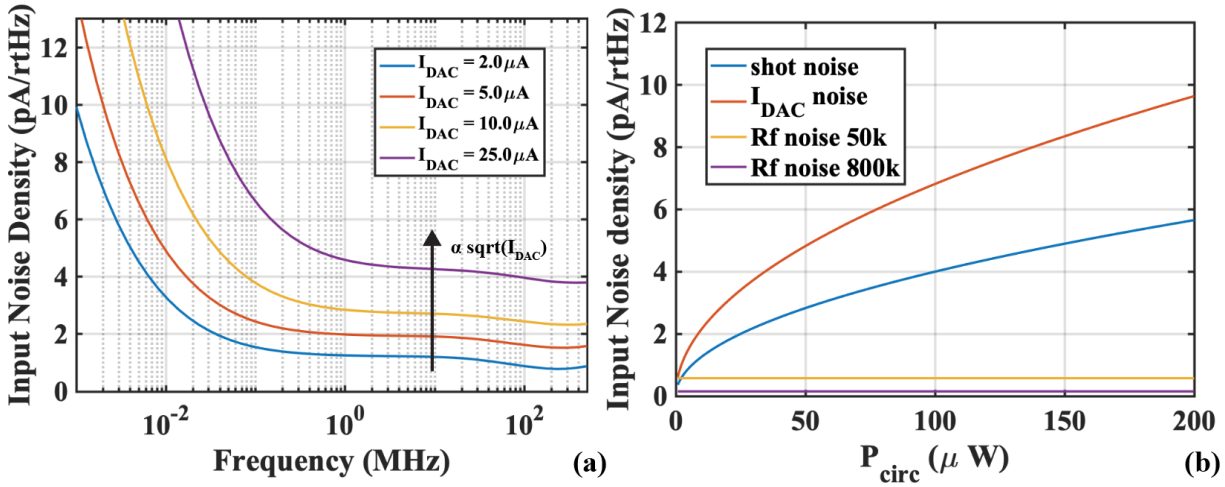

Figure 4.13: (a) Noise simulations for various I_{DAC} settings, (b) Input noise densities vs P_{circ} for different noise sources (right).

those we plot the SNR from Eq. 4.9, in Fig. 4.12, for $R_f = 50k\Omega$, $R_f = 5k\Omega$. There, it can be seen that for the R_f value range of our system (R_f = 50-800kΩ), we will always be shot-noise limited, even for very low optical power levels when the signal is still buried in noise (SNR < 1). Looking at the $R_f = 5k\Omega$ curve it can be seen that for low P_{circ}, when thermal noise is dominant the SNR increases quadratically with P_{circ}, while once the shot-noise starts being significant we have $SNR \propto P_{circ}$. This trend will hit a diminishing returns plateau once the $S_{phot} = P_{circ}Q/\lambda_{res}$ stops increasing linearly with optical power due to self-heating as will be shown experimentally in Chapter 5, implying the existence of an optimal P_{circ} point.

Noise simulations of the TIA and preamplifier, run while sweeping the I_{DAC} settings are presented in Fig. 4.13 (a), for the highest R_f setting (800kΩ), which will be used to detect the minimum incoming signal (i.e. the input corresponding to the NEP). Extracting the γ, and g_m parameters for the bleeder and inverter transistors from this simulation, we plotted the various noise contributions as a function of the power circulating in the ring P_{circ}, assuming $R_{PD} = 0.5$A/W, in Fig. 4.13 (b). This shows that our design is in the shot-noise limited regime; since the bleeder I_{DAC} needs to cancel the photocurrent, the corresponding noise follows a similar trend vs P_{circ}, and can therefore be considered "shot-noise", even though it is white in nature. Indeed the input noise density floor increases proportionally to $\sqrt{I_{DAC}}$, indicating that the thermal noise contribution is negligible.

Fig. 4.14 shows a pie chart of the noise contributions using the parameters from Table 4.1. The total noise, integrated over the BW of interest (80% fractional around 5MHz) is $\sqrt{\overline{\mathbf{I^2_{n,tot}}}} \simeq \mathbf{10.36nA}$. At the same time, using Eq. 4.8, and P_{app} = 2kPa, we obtain

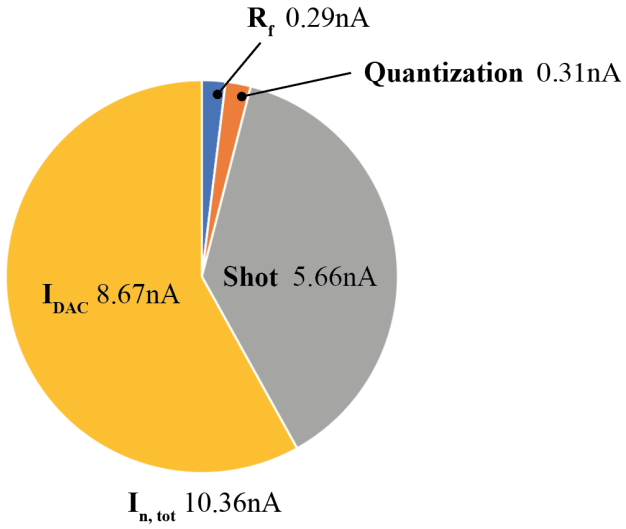

Figure 4.14: Breakdown of the integrated noise contribution of various sources, acquired using the values from Table 4.1, and $R_f = 800\text{k}\Omega$. The total integrated noise is acquired by summing the variances.

$\mathbf{I_{sense} = 30.8nA}$, indicating that our design should meet the target NEP specification.

Finally, to calculate the theoretically expected electronic DR we need to find the maximum current that does not saturate the ADC. The simulated full-scale range of the ADC is 0.6V, which can be referred back to the TIA input using the minimum $R_f G_{preamp}$ setting as: $I_{sat} = 0.6V/(2 \cdot 50\text{k}\Omega) = 6\mu\text{A}$. Hence, the DR_{el} is:

$$\text{DR}_{\text{el}} = 20\log\left(\frac{\frac{1}{2\sqrt{2}}I_{sat}}{\sqrt{\overline{I_{n,tot}^2}}}\right) = 46.2\text{dB}. \tag{4.10}$$

However, the sensor dynamic range will be limited by the ring linear region, which is $\sim FWHM$. That is because at high pressure levels we can reduce the incident optical power to the ring to ensure that we don't saturate the ring given that we have the necessary I_{DAC} resolution to properly cancel out the background current at the minimum gain setting. The sensor DR is defined as the maximum pressure that does not saturate the ring Lorentzian over the minimum detectable pressure. Given that $\text{NEP} = \sqrt{\overline{I_{n,tot}^2}}/(R_{PD}S_{phot}S_{int}) = 935\text{Pa}$, and that $P_{app,max} = FWHM/S_{int} = \frac{130\text{pm}}{40\text{fm/kPa}} = 3.25\text{MPa}$, we can write:

$$\text{DR} = 20\log\left(\frac{P_{app,max}}{\text{NEP}}\right) = \frac{P_{opt}R_{PD}}{\sqrt{\overline{I_{n,tot}^2}}} \simeq 73.7\text{dB}. \tag{4.11}$$

Even though it does not meet the 80dB requirement of pulse-echo ultrasound systems, it is expected to be adequate for a first implementation. Eq. 4.11 shows that the DR can be

improved by increasing the optical power incident upon the ring or by using more efficient photodetectors to lower the total input current noise, and consequently the NEP.

4.3.2 Digital Back-End

4.3.2.1 Tuning Controller

As mentioned in Chapter 2, a reliable tuning mechanism of the ring resonance is necessary to compensate both for process and temperature variations. It is of use for both the remoted ultrasound sensor-receiver scheme which requires alignment of the sensor to the photodetector MRR, and the WDM 2-D array interrogation which requires precise alignment of each MRR in the array onto a separate optical mode of the comb laser input. In this EPSoC we actively tune the resonance by wrapping a feedback loop around the ring.

A diagram describing this feedback loop is presented in Fig. 4.15. Initially, a PD that is embedded in the ring design with spoke shaped interdigitated P and N doped regions picks up a signal that is proportional to the power circulating in the ring. When the ring is off-resonance the power circulating in it is minimal and thus the PD signal will be low, while at on-resonant wavelengths this signal starts growing. The PD photocurrent is then

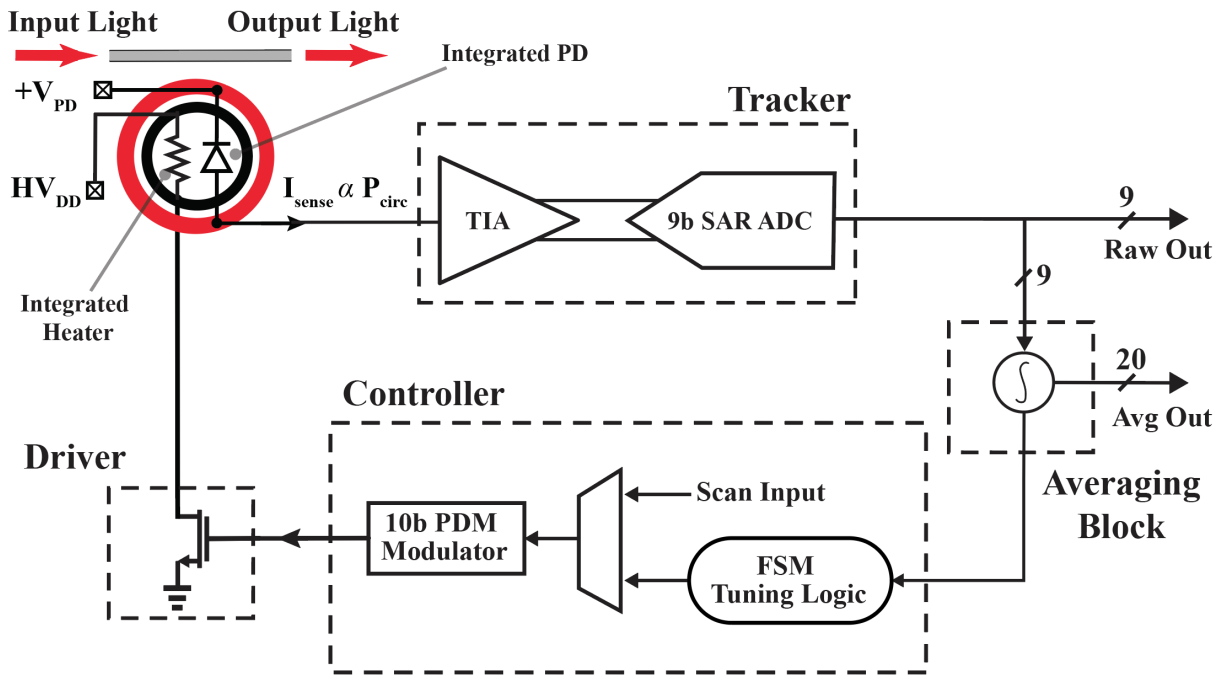

Figure 4.15: Architecture of a wavelength locking feedback loop comprised of an embedded PD, tracking and averaging circuits, digital control logic and driver of the integrated heater.

fed into a tracking circuit that converts it to an appropriate error feedback signal that serves as input to the controller. Here, the receiver analog front-end described in Section 4.3.1 is also used as a tracker. The output of the 9-b SAR ADC is averaged 512 times in order to reduce noise, and provide a smooth input signal to the controller. This averaged output is also monitored through scan for debugging purposes. The controller then uses the averaged signal to guide the search of a finite state machine (FSM) that produces a control signal proportional to the correction that needs to be applied to the resonance. This correction is finally fed into a 10-b pulse density modulator (PDM), comprised of an accumulator and an NMOS switch in series with an resistive heater embedded in the ring cavity. The carry-out of the accumulator controls the gate of the switch thus modulating the current flow through the heater and consequently the temperature of the ring. Alternatively, the 10-b PDM input can be externally set through scan, to ensure the heater can be programmed in case the controller does not work as intended.

Before describing the operation of the FSM a few important considerations should be mentioned:

- **Thermal tuning:** Alternative ways of controlling the ring resonance through carrier-depletion [107] or carrier-injection [108] have been proposed in literature, however they cannot provide the sufficient tuning range to correct for process variations which can be up to 1-2nm (180-360GHz). On the other hand, the strong thermo-optic coefficient of silicon, provides a wide tuning range up to almost half an FSR, ∼7nm (1.2THz). Hence, in our application, where apart from process variation corrections, additional tuning range may be required to align the WDM rings with fixed wavelength multi-λ sources, thermal control of λ_{res} is the only viable solution.

- **Feedback loop bandwidth:** To ensure that the controller will only be cancelling thermal variations and not the incoming ultrasound signal, all digital logic after the averaging block needs to be running at a frequency that is above the thermal time constant of the ring (30μs) but below the lowest end of the spectrum of the signal of interest (here 3MHz, assuming an 80% fractional BW around 5MHz). In our case the controller is updated at 1.56 MHz (averaged ADC rate).

- **Lock-to-maximum (LTM) vs Lock-to-reference (LTR):** Depending on whether we intend to use the ring as a power detector or as a sensor we need to lock the resonance either precisely onto the input wavelength, or slightly offset from it, such that the sensitivity is maximized. To achieve this we will have two different modes of operation for the controller, LTM and LTR.

  Controllers operating in an LTM mode [109] in conjunction with an averaging block, will lock the resonance to the maximum average power, and are hence a good candidate if locking the λ_{res} directly onto λ_{in} is desired. In case the ring drifts they will attempt a correction assuming a certain type of drift (blue or red) has occurred. If the choice of the correction sign was wrong they will flip the sign, otherwise they will retain it

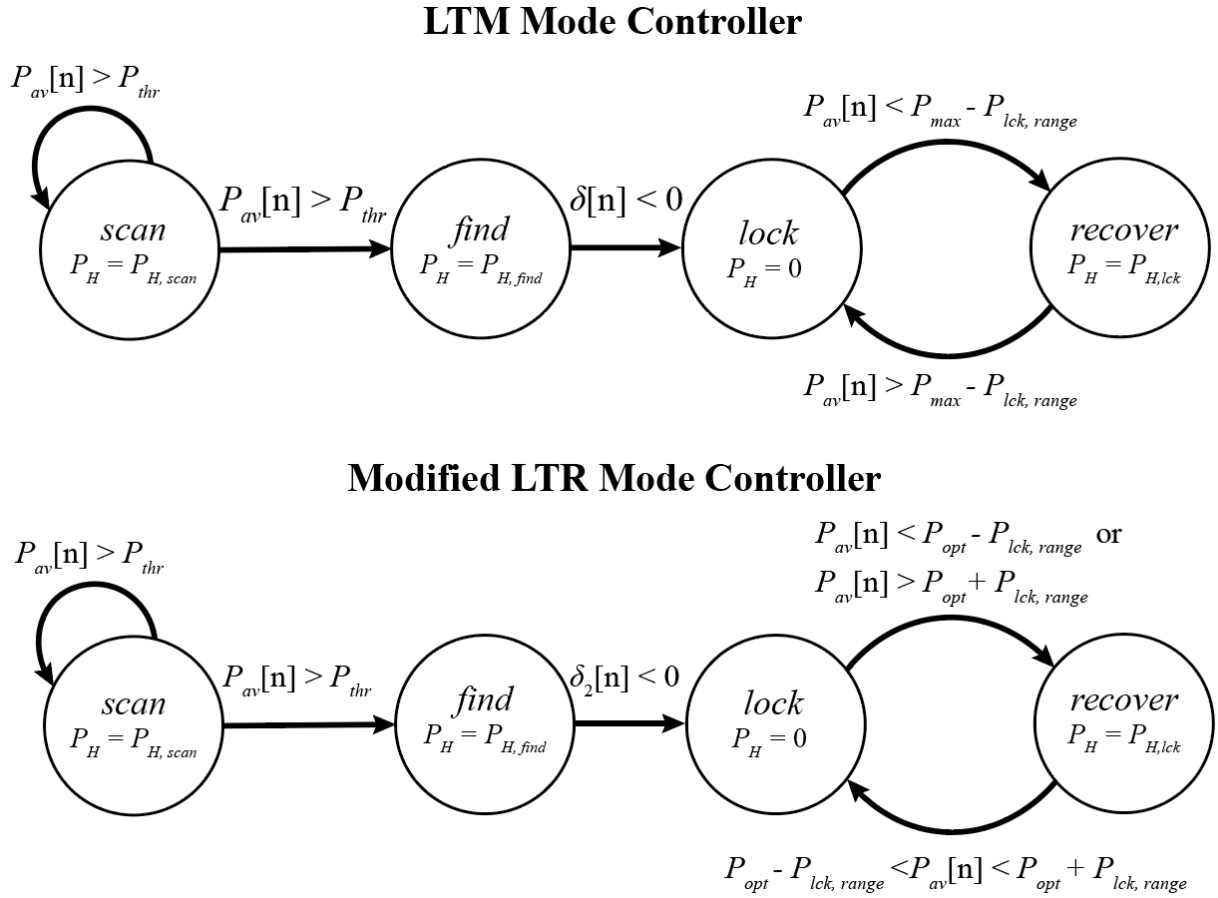

Figure 4.16: State-chart of the controller FSM in LTM and modified LTR modes.

until lock it regained. This lack of directional awareness will take up some time but the controller eventually recover.

When searching for an optimal slope point, as is the case when the MRR is operated as a sensor, simple LTR mode controllers [110] are not appropriate, since the optimal reference level to which we will be locking is not known a priori. Hence, we will implement a modified LTR controller, where the reference is selected while attempting to reach lock, by looking at the sign of the second derivative of the data from the tracker.

The controller, which can be programmed to operate either in an LTM or in a modified LTR mode, can be described by an FSM that has 4 different states: ***scan***, ***find***, ***lock***, and ***recover***. A state-chart diagram describing the decision process of the FSM is presented in Fig. 4.16. In both LTM and LTR modes it begins the search from the ***scan*** state, assuming

that $\lambda_{res,0} < \lambda_{in}$ [†]. In this state the light circulating in the ring is minimal, and the output of the ADC (and the averaging block) is low. The controller will keep incrementing the PDM by a coarse step, $P_{H,scan}$ until the averaged output, $P_{av}[n]$, crosses a certain threshold, P_{thr}, which will indicate that $\lambda_{res,h}$ is close to λ_{in}, and move the FSM into the ***find*** state where the PDM step is decremented to a finer value, $P_{H,find}$. In this state the difference between two consecutive readings of the averaging block is monitored. While $\lambda_{res,h} < \lambda_{in}$, it is expected that:

$$\delta[n] = P_{av}[n] - P_{av}[n-1] > 0, \tag{4.12}$$

since more and more power will be circulating the ring as the resonance moves closer to λ_{in}. A change of sign of $\delta[n]$ will indicate that the $\lambda_{res,h}$ became larger than λ_{in}.

In that case, if the controller operates in an LTM mode, we enter the ***lock*** state, set the desired lock power, P_{max}, equal to the current value of $P_{av}[n]$, and keep monitoring $P_{av}[n]$. If the ring drifts and $P_{av}[n] < P_{max} - P_{lck,range}$, the controller enters a ***recover*** state where it attempts to correct for the introduced error, using an even finer value for the PDM step, $P_{H,clk}$, until $P_{av}[n] > P_{max} - P_{lck,range}$ is satisfied. $P_{lck,range}$ is used to introduce a "dead-zone" where the ring is considered locked even if $P_{av}[n] < P_{lck}$ such that constant dithering of the PDM is avoided. Lastly, if the sign of the applied correction is wrong, the controller will change it in the next iteration.

However, if the controller operates in the modified LTR mode, we remain in the ***find*** state and start monitoring the second derivative of $P_{av}[n]$:

$$\delta_2[n] = \delta[n] - \delta[n-1] = P_{av}[n] - 2P_{av}[n-1] + P_{av}[n-2], \tag{4.13}$$

where now a change of sign of $\delta_2[n]$ indicates that we have found the P_H value that corresponds to the maximum slope. Subsequently, the ***lock*** state is entered and the reference point, P_{opt}, is set, while $P_{av}[n]$ is still monitored. In the case of a drift outside the dead-zone, $[P_{opt} - P_{lck,range},\ P_{opt} + P_{lck,range}]$, we enter the ***recover*** state, and the PDM step is set to $P_{H,lck}$. Since we are no longer locking to maximum, the controller has knowledge of the proper sign for the correction signal and can quickly recover.

Lastly, it should be mentioned that the values of P_{thr}, $P_{H,scan}$, $P_{H,find}$, $P_{H,lck}$, and $P_{lck,range}$ are all programmable through scan.

A simulation of the controller locking to the resonance (LTM mode) is shown in Fig. 4.17. In this case the selected value for $P_{H,find}$, is obviously too large, causing the controller to overshoot and essentially enter the recover state right after crossing the resonance. Having recorded the optimal max value, P_{max} though it is able to correct for that error, lock, and dither around the optimal value.

[†]It should be noted that this condition is by no means guaranteed to be true, especially in WDM rows with multi-λ combs where additionally we need to ensure that the each ring is locked onto to a different optical mode to avoid ISI. A solution to this problem is to run a "bring-up" calibration step per WDM row to chart the resonances with respect to the optical modes and subsequently properly initialize the PDM before letting the FSM take-over and run its locking algorithm.

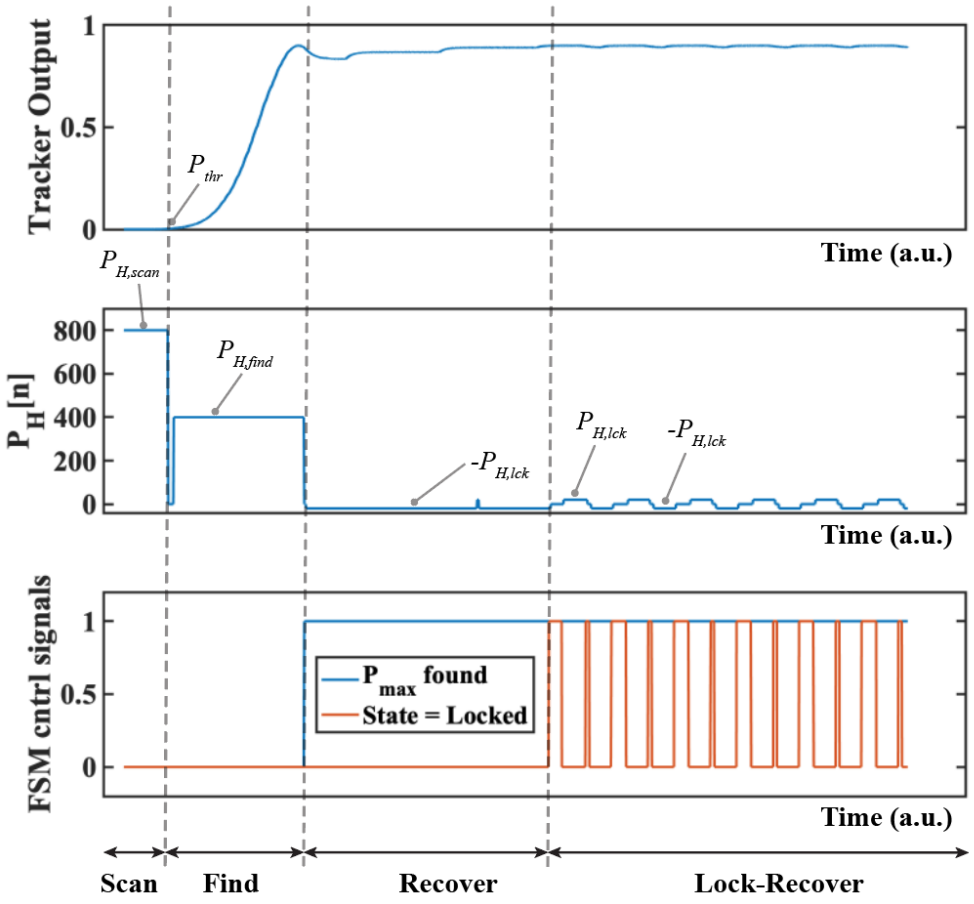

Figure 4.17: Controller lock-on simulation, showing the output of the tracker unit. The values of $P_H[n]$, and FSM control signals are monitored and as the state of the FSM evolves.

4.3.2.2 PDM Driver Modeling

The PDM driver circuit is shown in Fig. 4.18 a. It consists of an accumulator whose input, P_H is provided by the tuning controller, and uses the carry out to drive the gate of a switch transistor that turns the current through the MRR embedded heater ON and OFF. This carry out of the PDM driver has a periodic behavior with an average frequency f_{av} that is given by:

$$f_{av} = \frac{P_H}{2^b} f_{clk}, \tag{4.14}$$

where f_{clk} the frequency at which the PDM is run, and b the number of bits in the accumulator. To ensure that the average period of the PDM is well below the thermal time constant of the MRR, while sufficient randomization of the output pattern is achieved, and timing around the accumulator is comfortably closed, we have chosen $b = 10$, $f_{clk} = 800$MHz. At

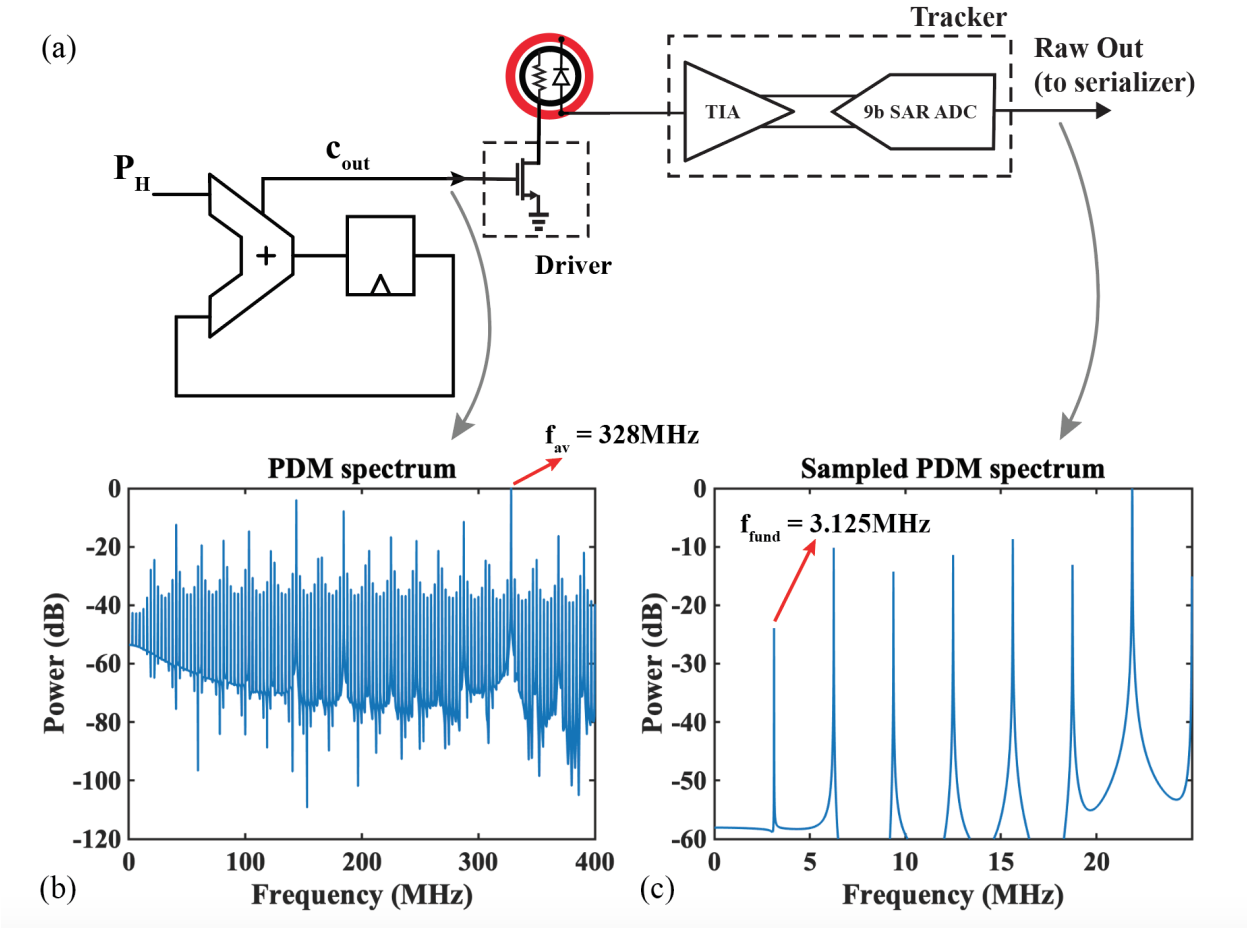

Figure 4.18: (a) Accumulator PDM circuit and simplified front-end schematic, (b) Spectrum of the carry out sequence for an input $P_H = 420$, (c) Sampled spectrum of the same sequence at the ADC output, indicating fundamental tones in the ultrasound band.

the same time, for the most often used heating codes, $P_H > 40$ the average frequency is, $f_{av} > 31.25$MHz above the bandwidth of interest for pulse-echo ultrasound experiments.

However, the pseudorandom carry out of the PDM actually has a fundamental period that is much longer that the average period, and can be calculated applying the theory developed in [111]:

$$f_{fund} = \frac{\gcd\left(P_H, 2^b\right)}{2^b} f_{clk}, \tag{4.15}$$

This practically means that the carry out spectra will have spurious content at f_{fund} intervals, even though most of the power will be around f_{av}. When P_H is not a power of 2, as is most often the case for realistic controller outputs, f_{fund}, will fall inside the frequency

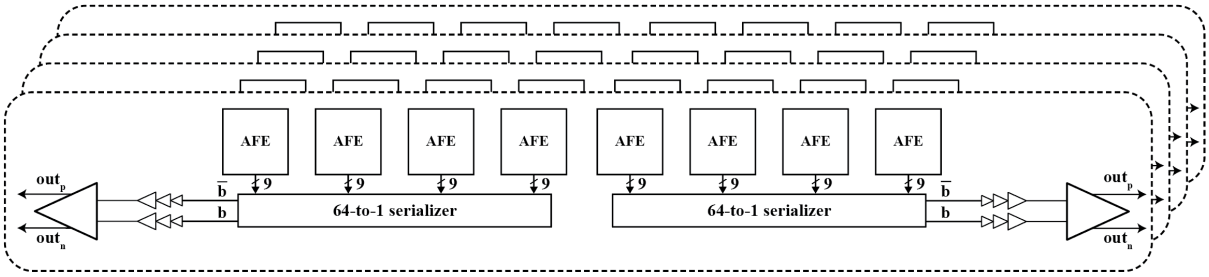

Figure 4.19: Grouping and serialization of the digital outputs of the 8x4 PD-MRR array.

range of the ultrasonic signal. A simulation of the PDM output spectrum for a midcode, non-power of 2 input of $P_H = 420$ validating this theory is shown in Figs. 4.18 b, c. Note that for that input Eq. 4.15 gives: $f_{fund} = \frac{4}{1024} \cdot 800\text{MHz} = 3.125\text{MHz}$, as indicated in Fig. 4.18 c.

In such cases it is possible for in-band tones that are capacitively coupled from the heater to the anode contact of the PD to be picked up and amplified by the TIA. This has been experimentally observed and leads to a degradation of the receiver SNDR. In future implementations this issue could be alleviated by the addition of a capacitor at the TIA input node, that would ensure the capacitive coupling is minimal, at the expense of higher noise from the TIA input differential pair (Eq. 4.6).

4.3.3 Serialization and Output Stage

Finally, the digitized signal from the AFE needs to be transmitted for post-processing and image reconstruction. To minimize the number of output bumps that are required we have arranged the 32 PD-MRR receiver units into groups of 4. 64-to-1 serialization is employed to bundle the 9-b ADC outputs of 4 receiver cells, while the remaining 28-b are hard-coded using a preamble pattern of 14 *1*s, followed by 14 *0*s to assist with data alignment during de-serialization. As shown in Fig. 4.19. 2-to-1 serializers have been implemented by using a 2:1 MUX and a latch on the even path.

A CML driver with load resistance R_L, is the final output stage. The transistors of this diff-pair are sized to provide sufficient differential swing for GTX receivers assuming 50Ω termination and speeds up to 6.4GHz, while abiding by electromigration reliability rules. To drive the large input capacitance of the CML output stage, digital buffers have been placed between the output of the serializer and the CML driver's input.

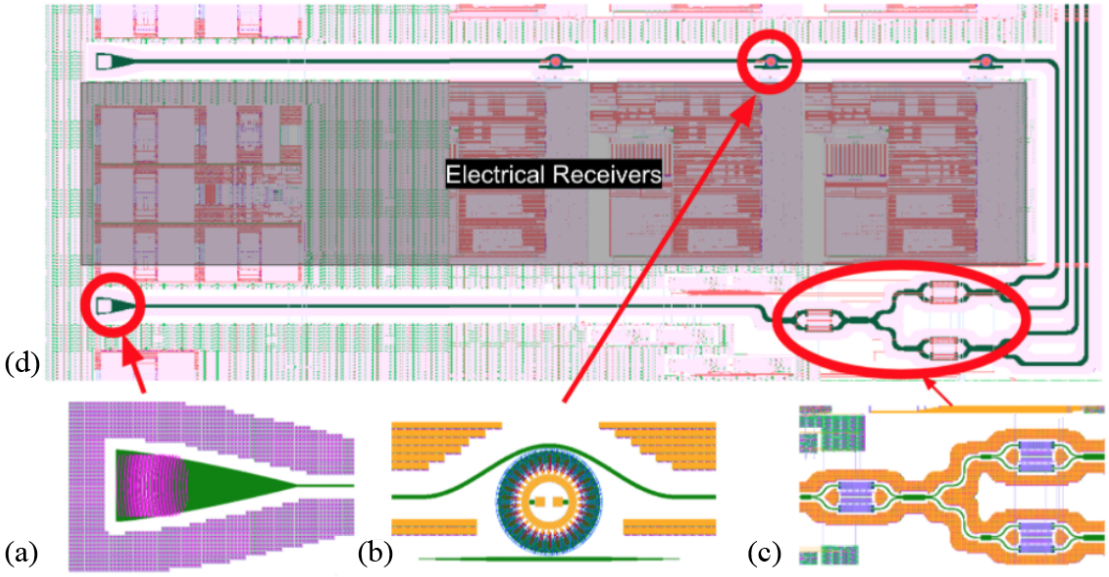

Figure 4.20: (a)-(c) Callouts of grating coupler, sense-MRR, and optical MMI splitter tree (d) Ring row utilizing primitives (a)-(c) and a waveguide loopback. From [91].

4.4 Electronic-Photonic SoC Implementation Strategy

4.4.1 Photonic Layout Generator

Having analyzed the design details of the individual sensing unit we will proceed to discuss the strategy followed to implement a large 2-D array based on that electrical sensing unit with the system attributes presented in Section 4.2.

We start by describing the generation of the photonic layout. This was implemented hierarchically using the Berkeley Photonics Generator (BPG) [72, 91], to build 3 different 8×4 WDM MRR arrays, 8 coherent sensing test-sites, and 8 high Q sense MRR experimental test-sites. BPG utilizes `PhotonicTemplateBase`, an abstract base class serving as a common interface, which is subclassed by photonic layout generators and gives them access to primary shape creation methods such as the addition of instances or shapes. This way we can generate photonic devices with programmable parameters, such as MRRs, grating couplers, or MMI splitters. These devices are the fundamental components that will be then pieced together to form entire MRR arrays, and are shown in Fig. 4.20 (a)-(c).

In the core of our layout is the ring row generator class, `RingRow`, which also subclasses `PhotonicTemplateBase`, and instantiates multiple MRRs that are connected using the waveguide router class. These rows can have different pitch between the rings, incre-

mented ring radii (a feature used for WDM rows), or even different ring types (a feature that allows a sense and PD ring to be instantiated in the same row). Arranging four rings rows of eight WDM rings in parallel, we created 2-D WDM MRR arrays. One of these arrays was comprised of PD-MRRs, which are expected to have lower Q due to the SiGe absorption region that enhances responsivity. The other two arrays were made up of slightly different flavors higher Q sense-MRRs. To save space and provide a single optical input to each sense MRR array we employed an MMI splitter tree and low loss Euler waveguide turns to loop back the input waveguide, as illustrated in Fig. 4.20 (d). This loopback structure will be very useful in aligning the fiber block assembly that will be attached on our EPSoC as described in Section 5.1. A photo of the entire fabricated 2-D WDM sense MRR array is shown in Fig. 4.21. The rest of the chip will be occupied by the coherent-sensing and high Q test-sites, as shown in Fig. 5.1.

Finally, to assemble a photonic top layout all of the array classes mentioned above are called in a top level script, that instantiates them at the desired locations in the chip. In summary, the hierarchy of our photonic generator is the following:

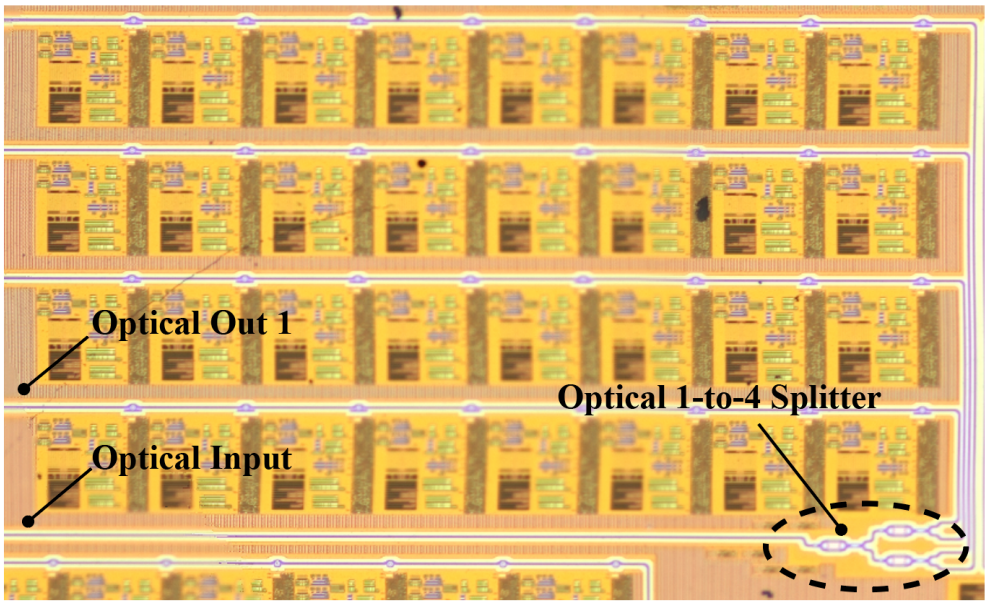

Figure 4.21: Zoom-in photo of the fabricated 2-D WDM sense MRR array, automatically generated using BPG, with call-outs of fundamental sublocks.

```
Top level generator
├── PD array
│   └── Grating couplers + WDM PD-MRR rows
├── Sense array
│   └── Grating couplers + MMI splitter tree + WDM sense-MRR rows
├── Coherent sensing test-site
│   └── Grating couplers + adiabatic coupler + WDM sense-MRR rows + WDM PD-MRR
│       rows
└── High-Q test rows
    └── Grating couplers + High Q WDM MRR rows + WDM PD-MRR rows
```

4.4.2 Mixed-Signal Electrical Sensing Unit

To build the mixed-signal electrical sensing unit, we first generated and connected (using BAG and Laygo) all the individual circuit blocks that comprise the AFE of Fig. 4.8, namely the I_{DAC}s, TIA, preamplifier and SAR ADC. A Library Exchange Format (LEF) file was extracted for that AFE, containing routing blockage and pin location information that can be used by Innovus during the place and route (PnR) procedure. A top level register transfer language (RTL) file includes both the digital logic block describing the tuning controller and digital back-end, specifying the connections that need to be made during PnR. The produced layout of the mixed-signal block is shown in Fig. 4.22.

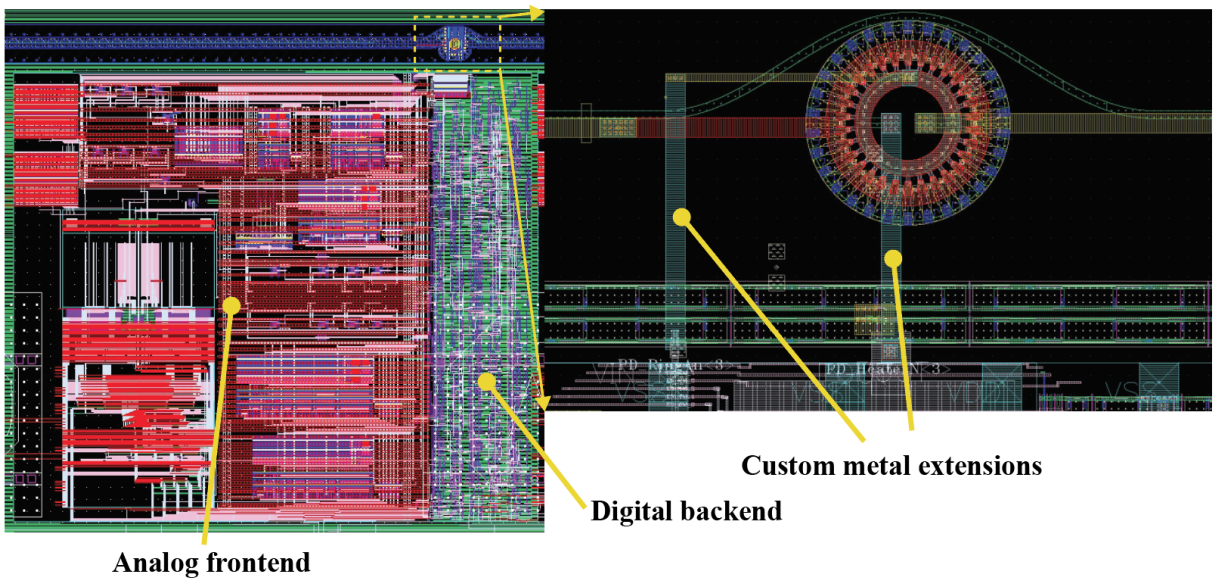

Figure 4.22: Layout of the mixed-signal electrical sensing unit (left), zoom-in of the metal extensions of the MRR port illustrating the connection by abutment (right).

4.4.3 Electronic-Photonic Top Level Integration

The last step was to instantiate the top level photonic layout together with multiple instances of the mixed signal sensing unit, current and clock distribution networks, serializers, CML output stages, ESD, decoupling capacitors, and I/O pad driver cells. This was done using an Innovus PnR flow similar to the one, where LEF files for each of the aforementioned circuit blocks were used by the digital routing tool for keep-out and port connectivity instructions. After adding custom metal extensions to all ring ports, a LEF file was extracted for the top level photonic layout as well. This was done to avoid any routing happening in the ring region and potentially causing shorts or interfering with the optical mode. The photonic top and mixed-signal blocks were then co-instantiated in a top level digital digital RTL script, while their exact locations on the chip were specified during floorplanning. These locations carefully selected to ensure the metal extensions of the ring ports would be connected by abutment to the respective ports of the mixed-signal electrical signal units. A layout of a PD-MRR with those custom extensions connected to the mixed-signal block is shown in Fig. 4.22.

To illustrate the end result of this electronic-photonic integration, a photo of the fabri-

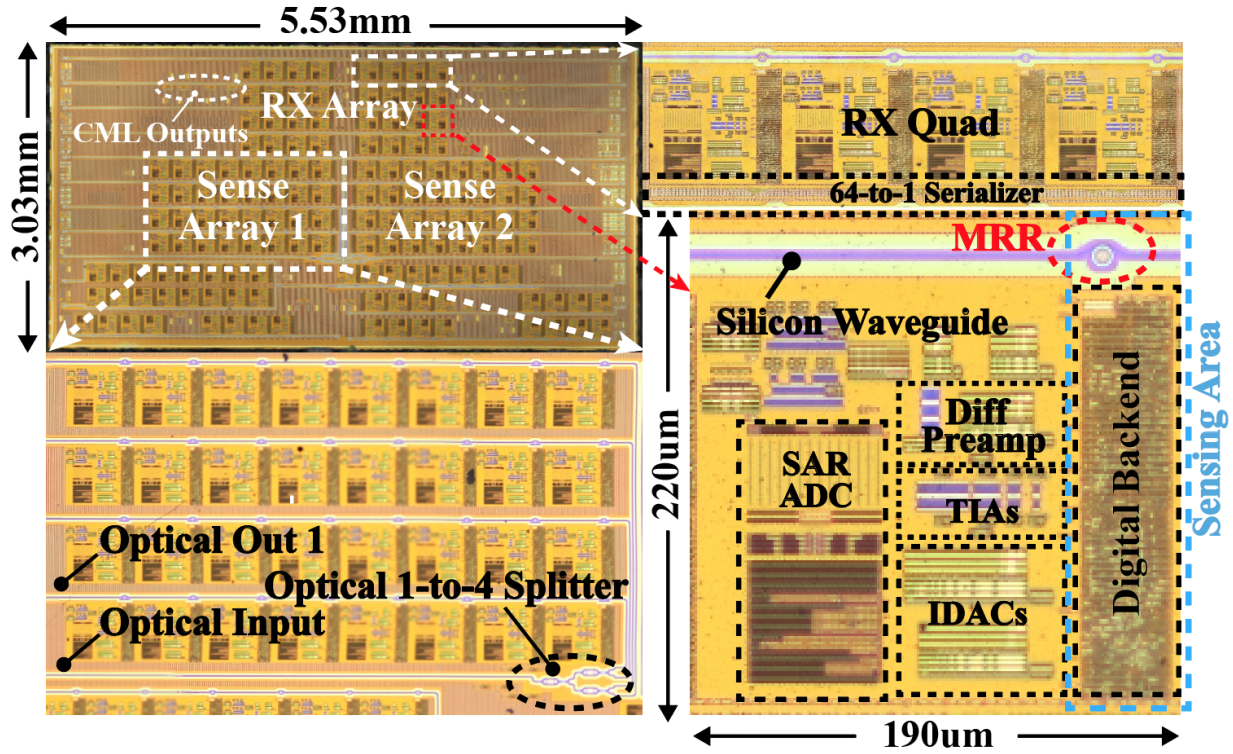

Figure 4.23: Photo of fabricated die, with insets of an 8x4 sensing MRR array, a receiver PD-MRR quad and a sensing unit.

cated die is shown Fig. 4.23, with insets of an 8x4 sensing MRR array, a receiver PD-MRR quad and a sensing unit.

4.5 Chapter Summary

In this chapter we initially derived the specifications for endoscopic ultrasound probes in terms of power, area, NEP, and DR. We followed this up by detailing the system architecture that will allow us to meet these specification, primarily from the standpoint of power and area consumption. Using optical MRR sensors in a remoted dual-chip sensor-receiver scheme, drastically lowers the power dissipated in the probe-head, while mitigating electrical cabling issues and enabling implementations with very high sensor density. Having relaxed the power specification of the receiver AFE, we explained the choice of a resistive feedback TIA topology, and performed a noise analysis to verify that our AFE design can in theory meet the target NEP and DR specifications. Subsequently, we outlined the design and requirements of a crucial system attribute, the thermal tuning controller, accompanied by simulation verifying the correct operation of the design. Modelling of the PDM driver used to tune the MRR resonance and explanation of how the digitized signal from the receiver array was grouped and serialized into high-speed serialized outputs was also provided. Finally, the methodology followed to co-integrate analog and mixed-signal blocks with digital circuitry and photonic devices in an Electronic-Photonic System-on-Chip was presented.

Chapter 5

Experimental Evaluation of Electronic-Photonic Ultrasound Receiver Array

Having extracted the target specifications for endoscopic ultrasound imaging and analyzed the design methodology for an electronic photonic system-on-chip (EPSoC) in Chapter 4, we will now experimentally evaluate the fabricated die. A photo of the taped-out EPSoC under test is shown in Fig. 5.1 with insets labeling the various subarrays presented in Section 4.4.

First, we will go over the packaging strategy and experimental setup that enabled us to

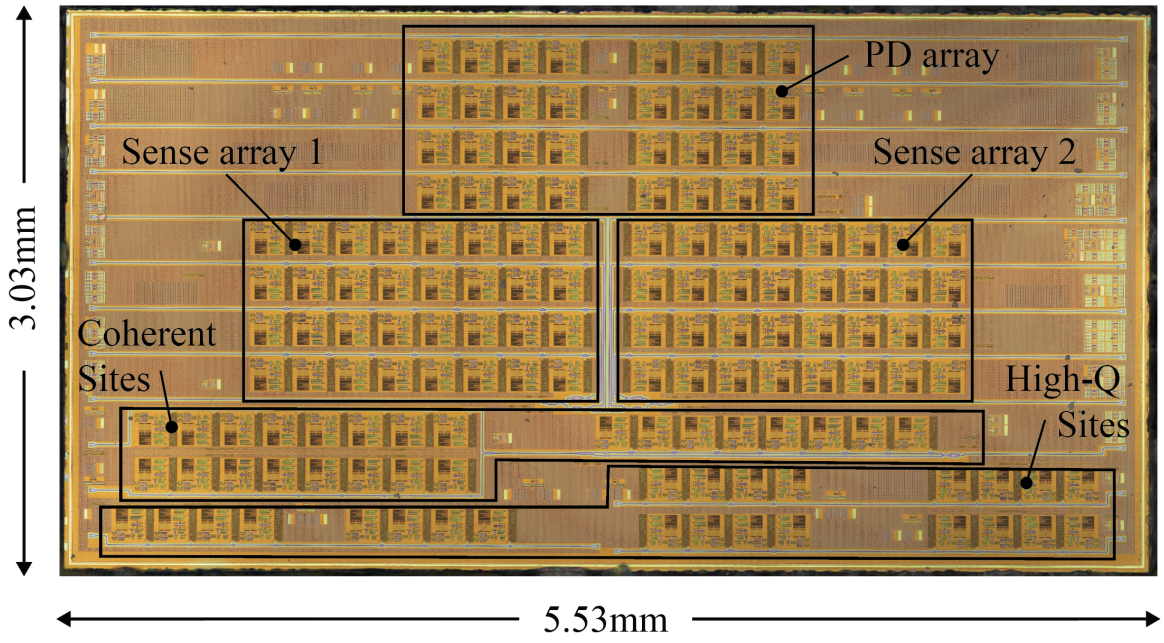

Figure 5.1: EPSoC die photo with insets into the various arrays discussed in Section 4.4.

perform electronic-photonic measurements under water. Then, we will validate functionality of the electrical front-end and the MRR WDM rows separately, with purely electrical and optical characterizations. A single sensing unit using a PD-MRR as both an ultrasound sensor and receiver will be extensively evaluated in terms of bandwidth, sensitivity, NEP and SNDR, before proving the concept of remote dual-chip sensor-receiver. Additionally, an 8 MRR WDM row will be simultaneously interrogated to acquire the first real-time optical ultrasound beamforming demonstration. Pulse-echo imaging experiments showing ultrasound reflection of 3 needle targets being detected will also be presented at the end of the chapter.

5.1 Electronic-Photonic Packaging & Experimental Setup

5.1.1 Electronic-Photonic Packaging

Packaging the first generation EPSoC in a way that would enable electro-optic measurements under water, was required for experimental verification. This included five-step procedure as outlined below, and illustrated in Figs. 5.2, 5.3:

- **Step 1. Flip-chip attach:** Initially the EPSoC is flip-chip attached onto a high density PCB that allows us to interface the die with the test equipment (fan-out digitized high speed outputs along with control and power signals). The attach was performed using Namics U8410-302SNS8 underfill epoxy.
- **Step 2. Substrate release:** To optically enable the chip a XeF_2 dry etch was performed to remove the 150μm thick substrate and expose the photonic devices, with the BOX effectively acting as an etch stop.
- **Step 3. Underfill sidewall etch:** Unfortunately, XeF_2 does not etch the Namics U8410-302SNS8 underfill epoxy used for flip chip attach. This meant that a 150μm tall sidewall prevented us from attaching the intended multi-channel fiber block to couple light onto the EPSoC. To remove the sidewall, a wet HNO_3 etch was performed on the assembled chip boards post substrate release. Note that the brownish mark is due to epoxy attacking the solder mask and has not been found to ruin the high-speed transmission lines. These first three steps are outlined graphically in Fig. 5.2.
- **Step 4. Fiber block attach:** To ensure stable coupling under water and insonification, we attached a 12-channel 250μm pitch fiber block using a UV-cured epoxy (NOA-61). An additional advantage of this multi-channel fiber block attach is the capability to assess multiple test sites at the same time, without having to realign fibers to the grating couplers. This step required μm precision alignment of the fiber-block, which was accomplished with a 6-axis nano-positioning stage. Extreme caution was

exercised to disperse a small amount of epoxy when performing the attach, such that the sensors remained exposed and not covered by NOA-61. This was accomplished by using a syringe to disburse the NOA-61. The loopback of the sensor array was used as a guide to align all channels of the fiber block.

- **Step 5. Protective water tank seal:** Given that ultrasound attenuation coefficient in air is 38 db/cm/MHz, we needed to submerge both the EPSoC and a PMUT transducer in a wet environment, while securely insulating the rest of the test equipment from water. To accomplish this we 3-D printed a tank that was sealed on the chipboard using RTV silicone, after the fiber block was attached. After sealing the tank onto the chipboard, the fiber block was glued onto the tank edge or a 3-D printed fiber holder

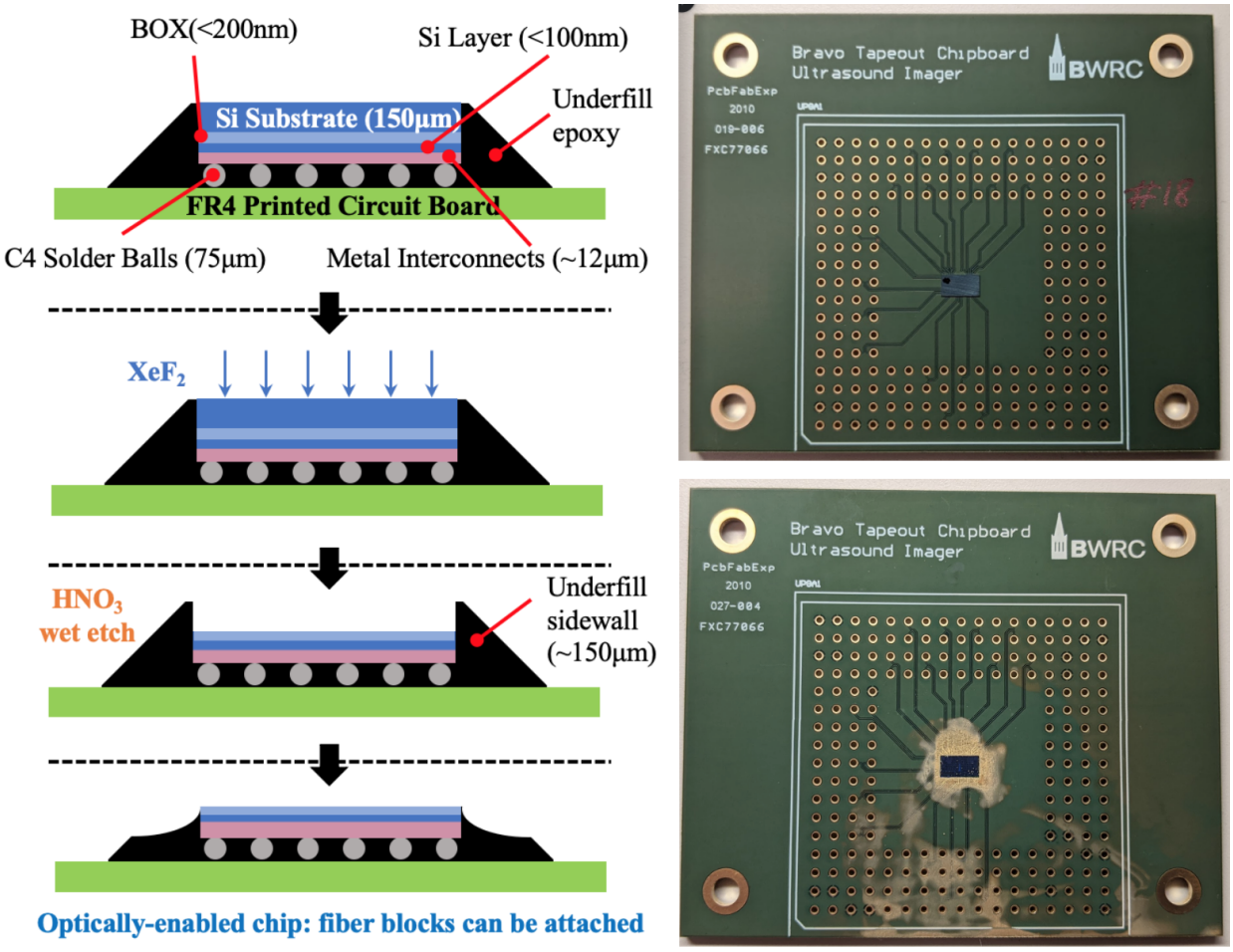

Figure 5.2: Illustration of the first three electronic-photonic packaging steps (left), and pictures of chipboard with die flip-chip attached before (top-right), and after substrate and underfill sidewall etching (bottom-right).

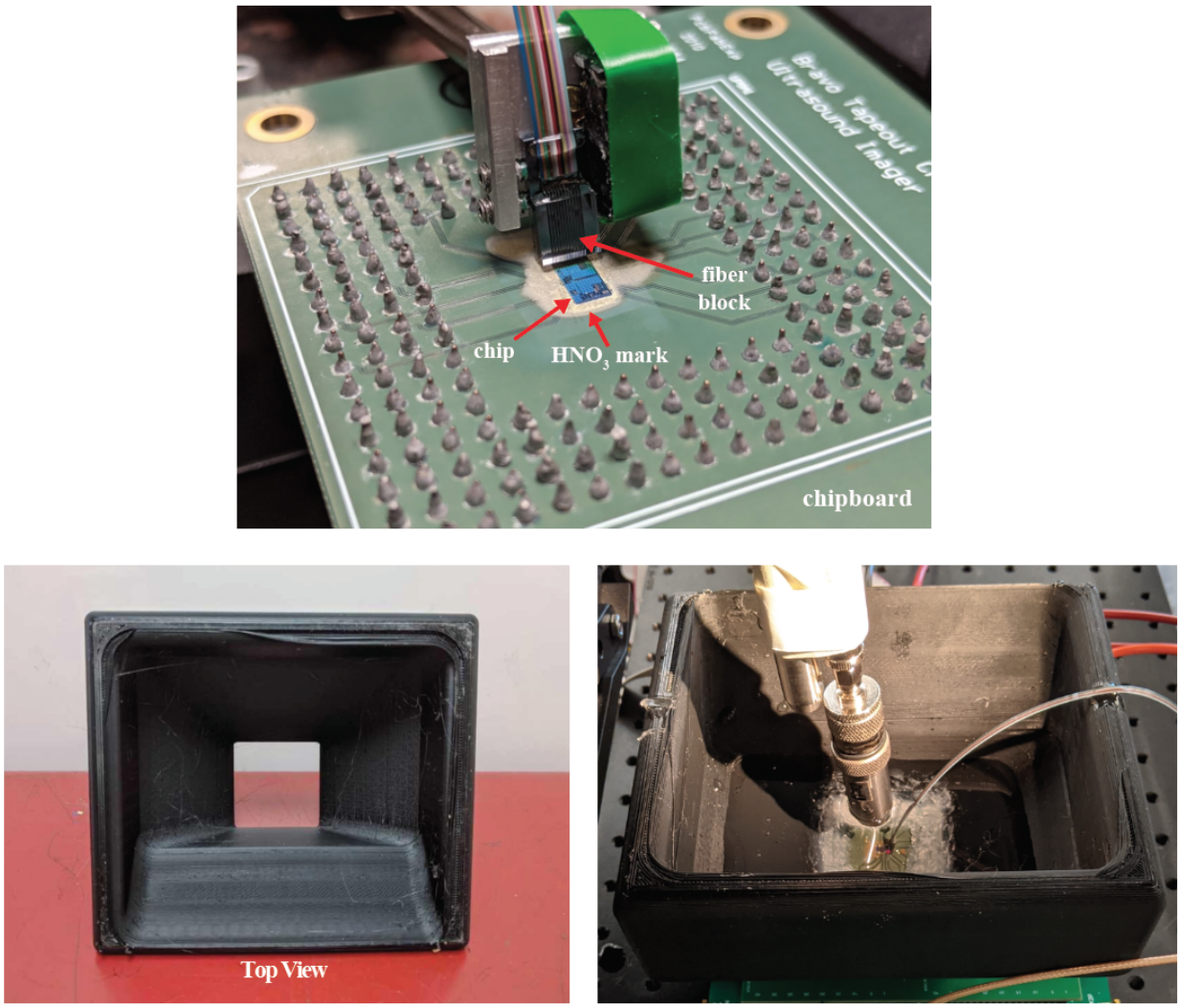

Figure 5.3: 12-channel fiber block mounted on a 6-axis nano-positioning stage ready to be aligned and attached on an EPSoC with substrate released and sidewall epoxy etched. (top) 3-D printed water tank (bottom-left). Assembly is ultrasound reception ready: Fiber block and water tank attached, PMUT transducer suspended above the chip under water (bottom-right).

that provided an anchoring point, to ensure the fiber block would remain attached to the chip. Finally, the chipboard pins were covered by silicone to ensure insulation. Steps 4 and 5 are depicted in Fig. 5.3.

5.1.2 Experimental Setup

To fanout signals from the chipboard, a pin-grid array (PGA) socket soldered on a hostboard was used. That hostboard also included LDOs that would set all power domains on the chip, decoupling capacitors, scan headers and banana power plugs. The chipboard is shown in Fig. 5.4, together with a zoom-in of the chipboard with the die attached and the pin headers soldered. A figure of this board setup with the chip-board in the socket, and power and scan connected is also illustrated in Fig. 5.4.

The entire experimental setup used to demonstrate our optical ultrasound receiver array is shown in Fig. 5.5. The chipboard is plugged in the PGA socket on the hostboard, the water-tank sealed on it, the fiber block attached, and a PMUT suspended over it. An innolume comb laser diode, and broadband optical amplifier used in the beamforming and remoted ultrasound experiments respectively, are also shown. An opal-kelly FPGA is used to configure the EPSoC through scan, while the Thorlabs PD-TIA module will be used for MRR bandwidth experiments in Section 5.2. Finally, a polarization controller is used to ensure maximum optical power is coupled into the EPSoC during each experiment, since single-mode fibers (SMF) were used in the fiber block assembly. Fig. 5.5 can also be used as

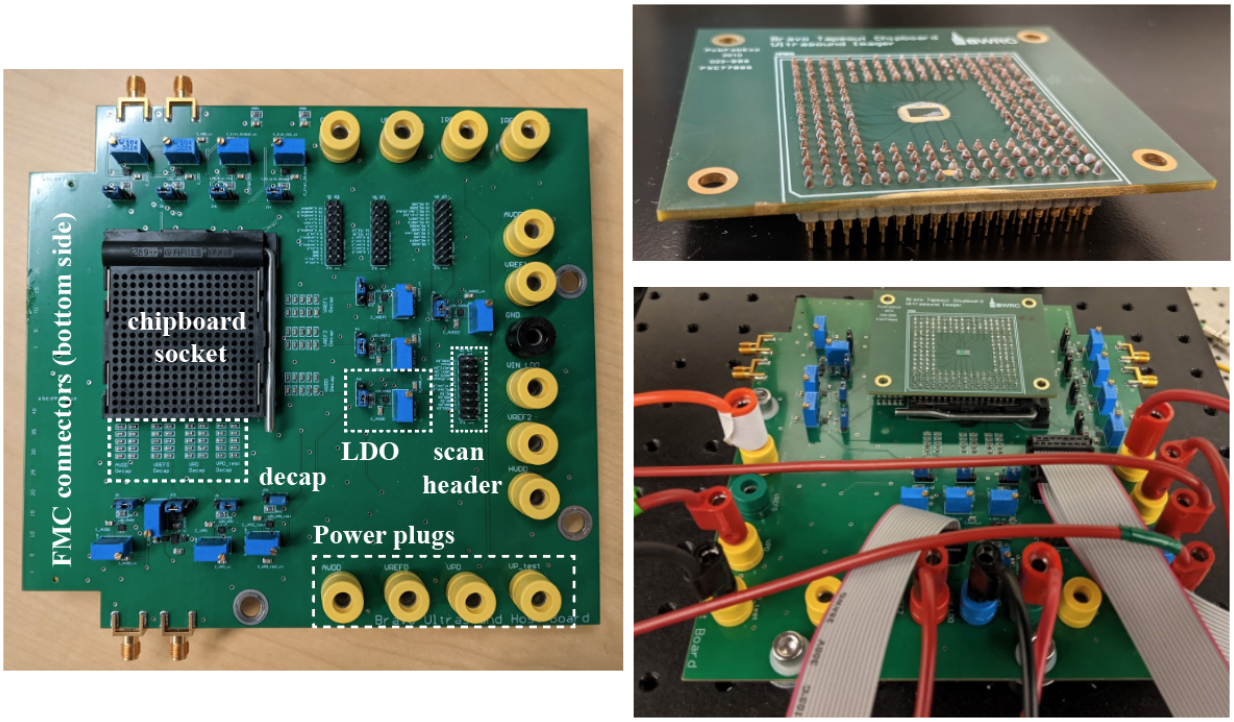

Figure 5.4: Hostboard design (left), Chipboard zoom-in with chip attached (top-right), Chipboard plugged onto the hostboard, with (bottom-right).

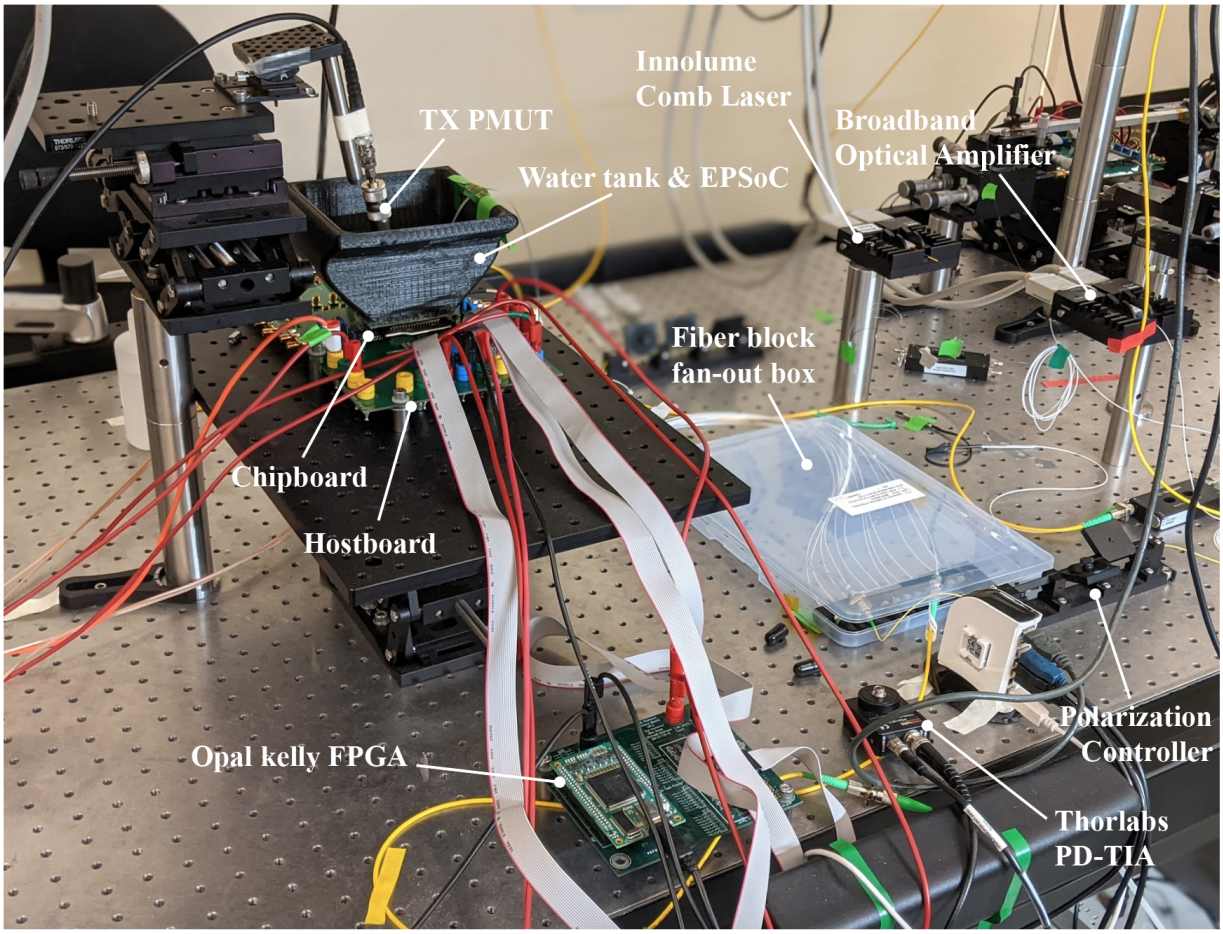

Figure 5.5: Experimental setup showing various components of the testing infrastructure.

a reference picture as we will be re-configuring the setup for various experiments performed in Section 5.3.

5.2 Fundamental Characterization of the Electronic-Photonic Sensing Unit

Before attempting to use our EPSoC to sense ultrasound, we wanted to evaluate the performance of the individual sub-blocks both in the electronic and the photonic domain. In this section, bring-up experiments validating the proper operation of the AFE, DBE, thermal resonance tuner, and PD-MRR are presented.

5.2.1 ADC Evaluation

To verify the correct operation of our AFE, we first attempted to capture the SAR ADC transfer function. To do so, we swept the current of the fine DAC at the lowest gain setting, $R_f = 50\text{k}\Omega$, as shown in Fig. 5.6. With a simulated fine I_{DAC} range of 4μA, and a preamp gain of 2, this gave us a swing of $\sim 50 \cdot 10^3 \cdot 2 \cdot 4 \cdot 10^{-6} = 0.4\text{V}$ at the input of the ADC. The DC transfer curve together with the extracted INL and DNL plots are shown in Fig. 5.6. An INL of ∼0.9 bits and a DNL of ±0.5 bits is recorded. Note that this is an extrapolated and not an actual INL/DNL curve since we only have 32 datapoints instead of the 512 required points from a 9-b ADC due to the lack of a direct test input. The expected SQNR degradation due

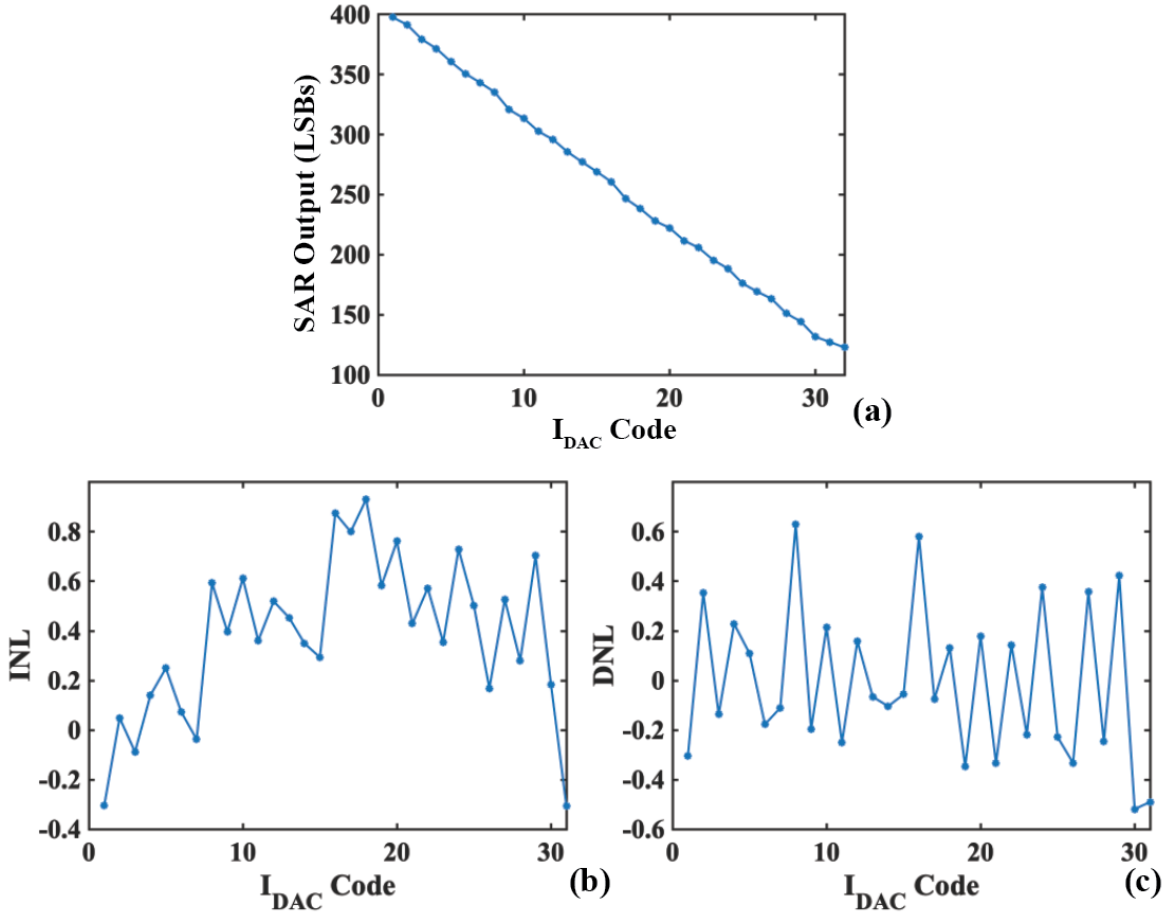

Figure 5.6: (a) SAR - ADC DC transfer curves as the fine I_{DAC} code is swept, and extrapolated (b) INL and (c) DNL metrics.

to the measured DNL can be found as:

$$SQNR_{deg} = 1.76 - 10\log\left(\frac{\frac{1}{8}}{\frac{1}{12} + \frac{DNL^2}{3}}\right) \simeq 3\text{dB}. \tag{5.1}$$

This will not be a limiting factor of the DR performance since the theoretical SQNR was ∼56dB meaning that the DR remains limited by shot noise at the frontend input.

5.2.2 Tuning Efficiency

To measure the tuning efficiency of the embedded ring heater in our die, we swept the heating code of the PDM at a fixed heater supply and recorded the resonant wavelength shift. At the same time we monitored the current drawn from the heater supply at each PDM code. As expected, the resonant shift varied linearly with the heater power, with a fitted slope of 0.68pm/µW shown in Fig. 5.7. This high tuning efficiency is a benefit of the monolithic integration of electronics and photonics, and will be a key system attribute in achieving ultra-low power consumption per sensing element.

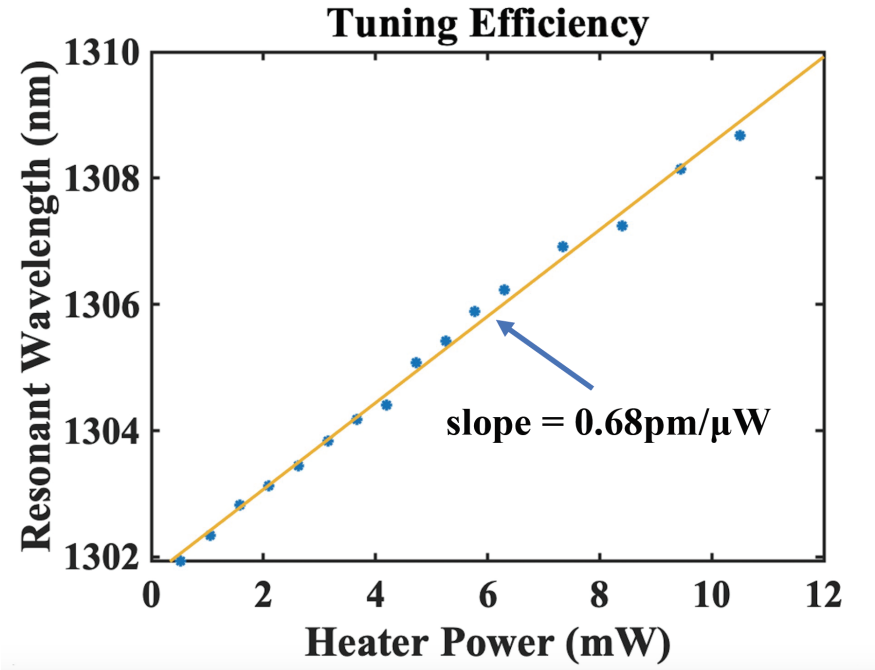

Figure 5.7: Tuning efficiency of the embedded ring heater extracted by sweeping the PDM driver code.

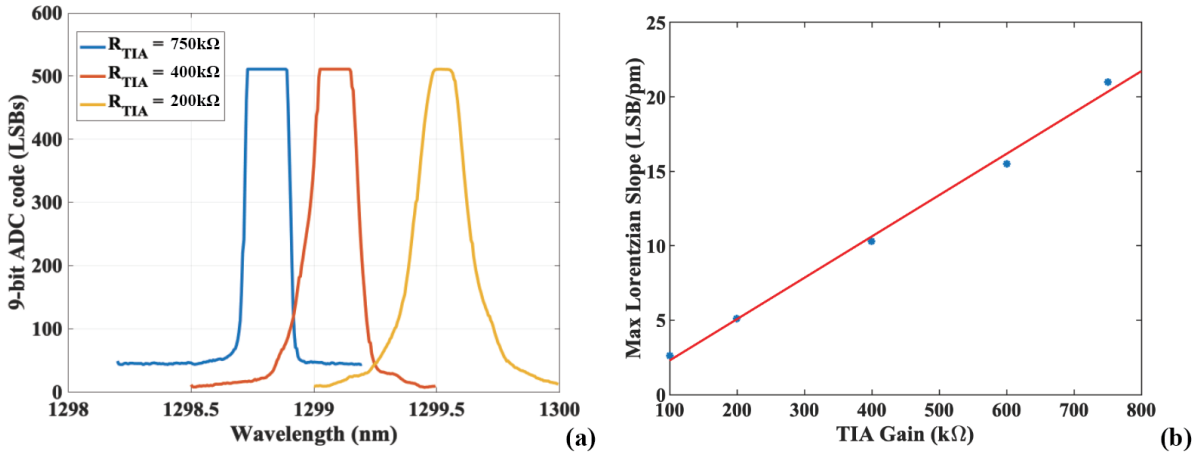

Figure 5.8: (a) Measured Lorentzian transfer functions of the same MRR at different gain and heater settings. Heater settings: blue:OFF, red:15% of tuning range, yellow:30% of tuning range, (b) Maximum ADC slope vs TIA gain.

5.2.3 Front-End Gain Linearity

The next verification step, was to perform an electro-optical experiment and attempt to capture a Lorentzian transfer function using the averaged ADC output of our electronic-photonic sensor-receiver. To this end, we swept the input wavelength of a tunable CW laser over a 2nm range, while varying both, the TIA heater resistance and the PDM heater settings. The acquired Lorentzians of Fig. 5.8 (a) validate our ability to tune both the resonant wavelength, and front-end gain (slope of the Lorentzian). Additionally, we have tracked the maximum slope at the ADC output for different R_f values, with the heater turned OFF. Fig. 5.8 (b) confirms the expected linear relationship between the TIA gain and Lorentzian slope.

5.2.4 Thermal Resonance Tuning Controller

Lastly, the operation of the resonance tuning controller will be examined. Initially, a CW laser input was parked slightly above the unheated ring resonance as assumed in Section 4.3.2.1. Then, the chip was brought up, and the thermal tuner was allowed to run and achieve lock. We observed that due to noise in the averaged ADC output, a flip of the sign of $\delta[n]$ in Eq. 4.12 occurred before the resonance, $\lambda_{res,h}$, crossed the input wavelength λ_{in}. The same holds true of the sign of $\delta_2[n]$, in Eq. 4.13. This meant that the controller would leave the ***find*** state and enter the ***lock*** state almost right after crossing the threshold, P_{thr}, regardless of the mode of operation, modified LTR or LTM. To circumvent this issue we run an initial calibration of the Lorentzian, and found the averaged ADC output value

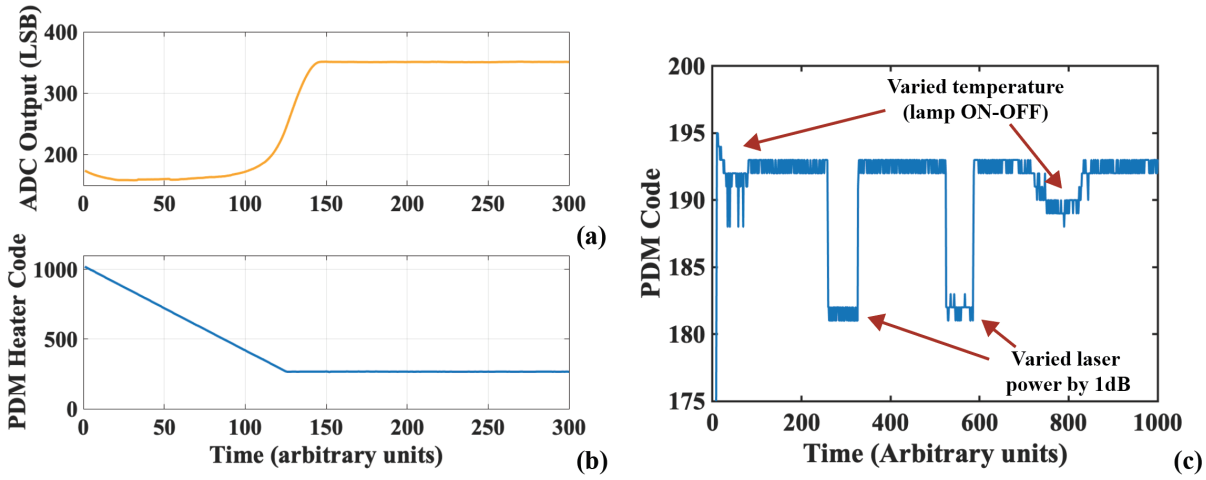

Figure 5.9: (a) ADC averaged output as the controller acquires lock, (b) PDM heater code adjusted by the controller to acquire lock, and (c) Lock maintained with variations in laser power and ambient temperature.

that corresponded to the maximum slope or the resonance. Then we set the threshold, P_{thr}, right on that spot and allowed the controller to run and acquire lock as shown in Fig. 5.9 (a), (b).

Having confirmed that lock can be acquired, we ensured that it can be maintained even under extreme disturbances, originating in temperature or power variations. Fig. 5.9 c, shows that the controller adjusts the PDM value when a microscope lamp is turned ON and OFF over the chip, resulting in mK changes in temperature, and when the input laser power is varied by 1dB.

5.3 Electronic-Photonic Ultrasound Receiver Demonstration

Having verified the operation of separate sublocks we will now proceed with ultrasound detection measurements. This will be done in a progression, first showing the fundamental electronic-photonic sensing unit, then proving the remote optical sensing concept and finally demonstrating beamformed WDM sensing and reflection imaging.

5.3.1 Single Sensing Element Characterization

To evaluate single sensor performance we first used a PD-MRR as both a sensor and a receiver. In this initial experiment, a CW laser was parked at the stable side of the PD-

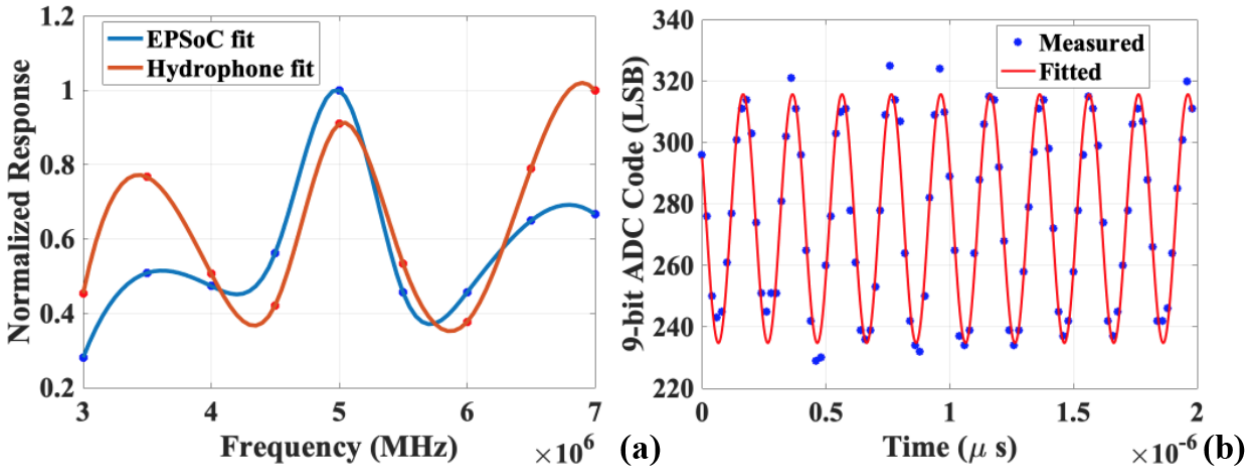

Figure 5.10: (a) Normalized amplitude vs frequency response of the EPSoC and a commercially available hydrophone (ONDA HGL-1000), (b) Received time-domain waveform corresponding to a 5MHz sinusoidal excitation

MRR Lorentzian, and the EPSoC was insonified. A piezoelectric transducer centered at 5MHz was used as a transmitter in these ultrasonic experiments. Fig. 5.10 a shows the normalized frequency response of our sensor and a commercial hydrophone, placed the same distance away from the transducer. Both responses follow the same trend, while their ratio remains within 6dB in the 3-7MHz range corresponding to an 80% fractional bandwidth.

A time-domain response of our sensor at the maximum gain setting without any heating applied is plotted in Fig. 5.10. It corresponds to a sinusoidal pressure excitation of 5MHz and a peak-peak amplitude of 12.1kPa. The unfitted measured waveform has a signal to noise and distortion ratio of 31dB and a fitted amplitude of 75 LSB codes. With the full scale of the 9-bit ADC corresponding to 0.6V we estimate the sensitivity of our sensor-receiver chain to be $S_{tot} = \frac{600\text{mV}}{512} \cdot 75 \cdot \frac{1}{12.1\text{kPa}} = 7.3\text{mV/kPa}$, comparable to the sensitivity of commercially available hydrophones.

To theoretically measure the NEP of our sensor, we parked the laser at the resonance flank and recorded the digital output of the chip without any ultrasonic excitation. We found that the noise standard deviation is 15 LSB codes without any averaging, while it drops down to 5 LSBs and 3 LSBs when 64 and 128 samples moving averages are used respectively. The ADC sampling rate was 50MHz, but can go up to 500MHz limited only by the on-chip 64-1 serialization. Defining as our NEP the point where SNR=1, and having experimentally verified the linearity of our detector, we can extrapolate the noise equivalent pressure to be $\text{NEP} = \frac{12.1\text{kPa}}{75/15} = 2.4\text{kPa}$, over a 25MHz BW, or equivalently $\text{NEP}_{\text{den}} = 0.48\ \text{Pa}/\sqrt{\text{Hz}}$.

To measure the SNDR at the ADC output we moved the transducer closer to the chip to get a response that was closer to full scale. The corresponding spectrum is shown in

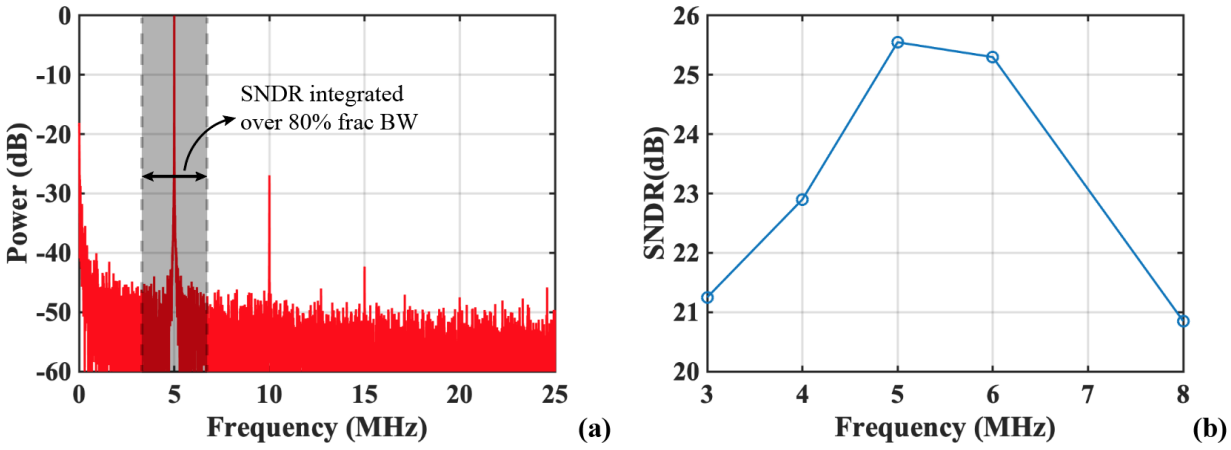

Figure 5.11: (a) Power spectrum of the PD-MRR -6dBFS response to a 5MHz tone input, (b) SNDR vs frequency.

Fig. 5.11(a). At the highest acquired amplitude, which was -6.7dBFS, we measured SNDR = 25.5dB. The SNDR was estimated by integrating the noise over an 80% fractional BW around 5MHz (i.e. 3-7MHz), where the signal of interest is expected to be. To estimate how our electronic photonic receiver behaves over frequency, we swept the PMUT excitation frequency seeing that the captured SNDR of Fig. 5.11(b) follows a trend similar to the amplitude response of Fig. 5.10(a).

An alternative way to estimate the NEP is through the SNDR. In the experiment of Fig. 5.11(a) the peak-peak amplitude of the response was 234 LSBs (-6.7dBFS). Using the extracted SNDR, we can estimate the integrated noise at the output of the ADC in LSBs:

$$SNDR = 20\log\left(\frac{\frac{1}{2\sqrt{2}}V_{amp,pp}}{N}\right)$$

$$N = \frac{V_{amp,pp}}{2\sqrt{2}\cdot 10^{SNDR/20}} = 4.4 \text{ LSBs}.$$

This noise can be referred to the input, to calculate both $I_{n,tot}$ and NEP. The gain used in this experiment was $R_f = 700\text{k}\Omega$, while the measured parameters relevant for S_{phot} calculation were $Q = 6000$, $P_{opt} = 100\mu\text{W}$, and $R_{PD} = 0.2\text{A/W}$. These values yield:

$$I_{n,tot} = N\cdot\Delta_{SAR,LSB}\cdot\frac{1}{G_{preamp}R_f} = 4.6\cdot\frac{0.6}{512}\cdot\frac{1}{2\cdot 700\text{k}} = 3.68 \text{ nA},$$

$$NEP = \frac{I_{n,tot}}{S_{int}S_{phot}R_{PD}} = 996 \text{ Pa}.$$

The NEP density can be estimated as $\text{NEP}_{\text{den}} = 0.498\ \text{Pa}/\sqrt{\text{Hz}}$, in close agreement with the previous experiment which was conducted on a different day and a different chip.

Note that the discrepancy between these values and the theoretically estimated values for $I_{n,tot}$, and NEP provided in Chapter 4, are due to the measured values for R_{PD} and Q-factor being lower than the ones assumed at design time. This results in a decreased $I_{n,tot}$, but also decreases S_{phot}, leading to a slightly worse NEP than the theoretically expected one. As expected from simulation and analysis, shot noise from the PD diode, and I_{DAC} noise are the limiting factors of the NEP performance of the MRR-AFE sensing element.

5.3.2 Remoted Optical Ultrasound

In order to prove the remoted ultrasound sensing principle that was proposed in Section 4.2.1, we have put together the setup of Fig. 5.12. A PD and sense MRR pair with similar unheated resonant wavelengths $\lambda_{res,0}$ were selected for this experiment. The resonant wavelength of the PD-MRR was first locked onto a CW laser input, parked at a fixed wavelength, λ_{in}, using the tuning controller. Subsequently, the heater of the sensor-MRR was swept, producing the Lorentzian response of Fig. 5.13 (a) that was captured on the ADC output through scan. Finally, the chip was insonified by the PMUT transducer and the time-domain waveform acquired is plotted in Fig. 5.13 (b).

To overcome the high grating coupler loss of ~5dB, which in this architecture has to be suffered thrice (in & out of sensing chip and in of the receiver chip), we pre-amplified the CW laser tone with a broadband optical amplifier (BOA). The self heating of the ring due

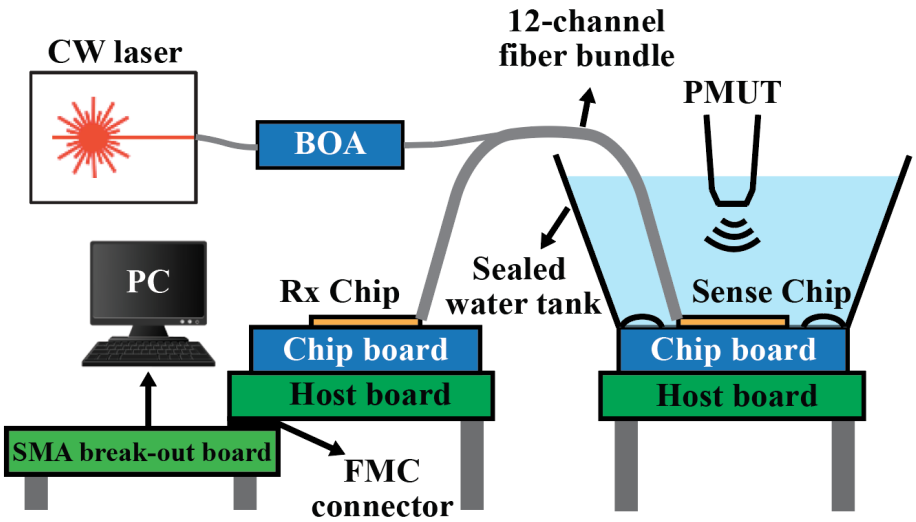

Figure 5.12: Illustration of the remoted optical ultrasound sensing setup.

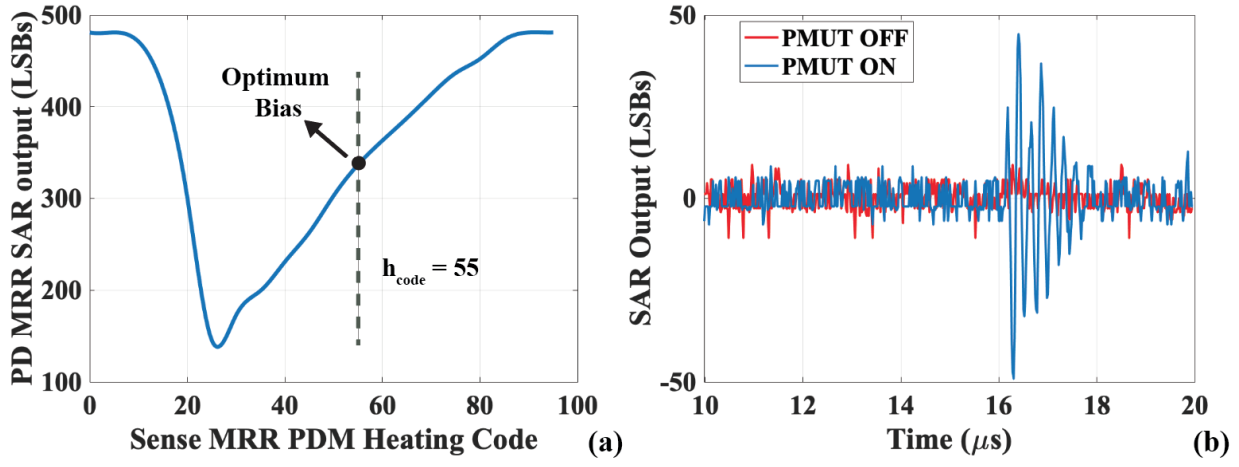

Figure 5.13: Remote sense-receive optical ultrasound sensing demonstration: (a) Sense MRR Lorentzian measured at the output of the PD MRR. (b) Time-domain received waveform with and without insonification.

to the high optical input power is obvious in the slope mismatch of the two sides of the Lorentzian in Fig. 5.13 (a).

The dual-chip scheme outlined in Section 4.2.2, was not possible to be demonstrated for the full sensor-receiver array primarily due to (a) a 7nm (∼1.26THz) mismatch between the nominal values of the central wavelengths, λ_c, of the available comb-laser diode, and the unheated sensor-MRR WDM row, and (b) a 4nm (∼720GHz) mismatch between the central resonant wavelengths of the unheated sensor-MRR and PD-MRR WDM rows. Specifically, it was: $\lambda_{c,\text{comb}} = 1310\text{nm}$, $\lambda_{c,\text{WDM}-\text{sense}} = 1303\text{nm}$, $\lambda_{c,\text{WDM}-\text{PD}} = 1299\text{nm}$. Even though the thermal tuner has a sufficient range to adjust the mismatch between the PD and sense MRR arrays, it cannot bridge the gap between the PD array and the comb laser. To do so, we attempted tweaking $\lambda_{c,\text{comb}}$ by changing the temperature and bias voltage of the laser diode, but this was also insufficient. This issue will be corrected in future tape-outs by properly sizing the MRRs using the data-points from this first prototype to achieve better resonance matching.

A second obstacle for the full array demonstration is the aforementioned grating coupler loss of ∼5dB in conjunction with the relatively low available input power from the comb laser used. The high loss, is primarily attributed to the manual in-house attach which did not allow alignment of the fiber block to the couplers with sufficient precision. It is not expected to be an issue in future implementations, since grating couplers with sub-dB loss have been reported in our technology [112], and can be incorporated in the next-generation ultrasound receiver EPSoC, together with a more precise fiber-attach method using automated equipment such as a FiConTec.

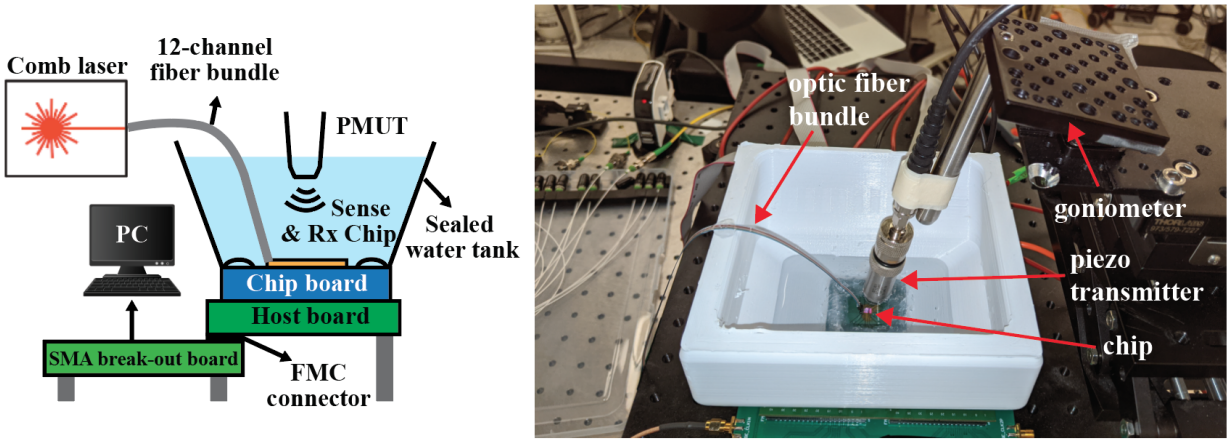

Figure 5.14: WDM RX beamforming setup: cartoon illustrating various components of the experimental setup (left), picture of the EPSoC and the PMUT transmitter submerged in water. The PMUT is attached to a goniometer that sets the transmission angle (right).

5.3.3 Optical WDM RX Beamforming

Given the bottlenecks discussed in the previous section, we will be using the PD-MRR array as both sensor and receiver to demonstrate the WDM RX beamformer concept. A comb laser diode was used to simultaneously interrogate 8 MRRs in this experiment, while a PMUT mounted on a goniometer was insonifying the EPSoC, as shown in Fig. 5.14. In a one-shot

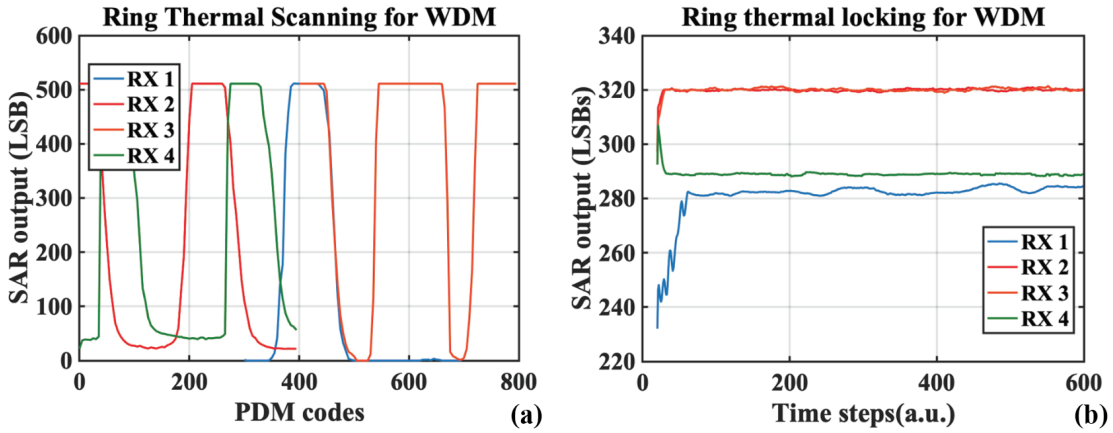

Figure 5.15: (a) Lorentzian characteristics of 4 of the 8 WDM MRRs captured by sweeping the PDM heater code, (b) Thermal tuning loop locking each ring to the maximum sensitivity point.

calibration step, the PDM codes of the heaters of all 8 rings used in this experiment were swept. The corresponding Lorentzians of 4 of them are captured in Fig. 5.15 (a). Due to the high TIA gain used, the ADC outputs shown here, are saturated. This is not an issue since the on-chip thermal tuning controller was subsequently used to ensure the rings were locked onto the optimal slope point of separate optical channels, well within the linear region of operation as shown in Fig. 5.15 (b). Finally, the chip was insonified and the bandpass filtered time-domain responses of the 8 rings are presented in Fig. 5.16. This experiment

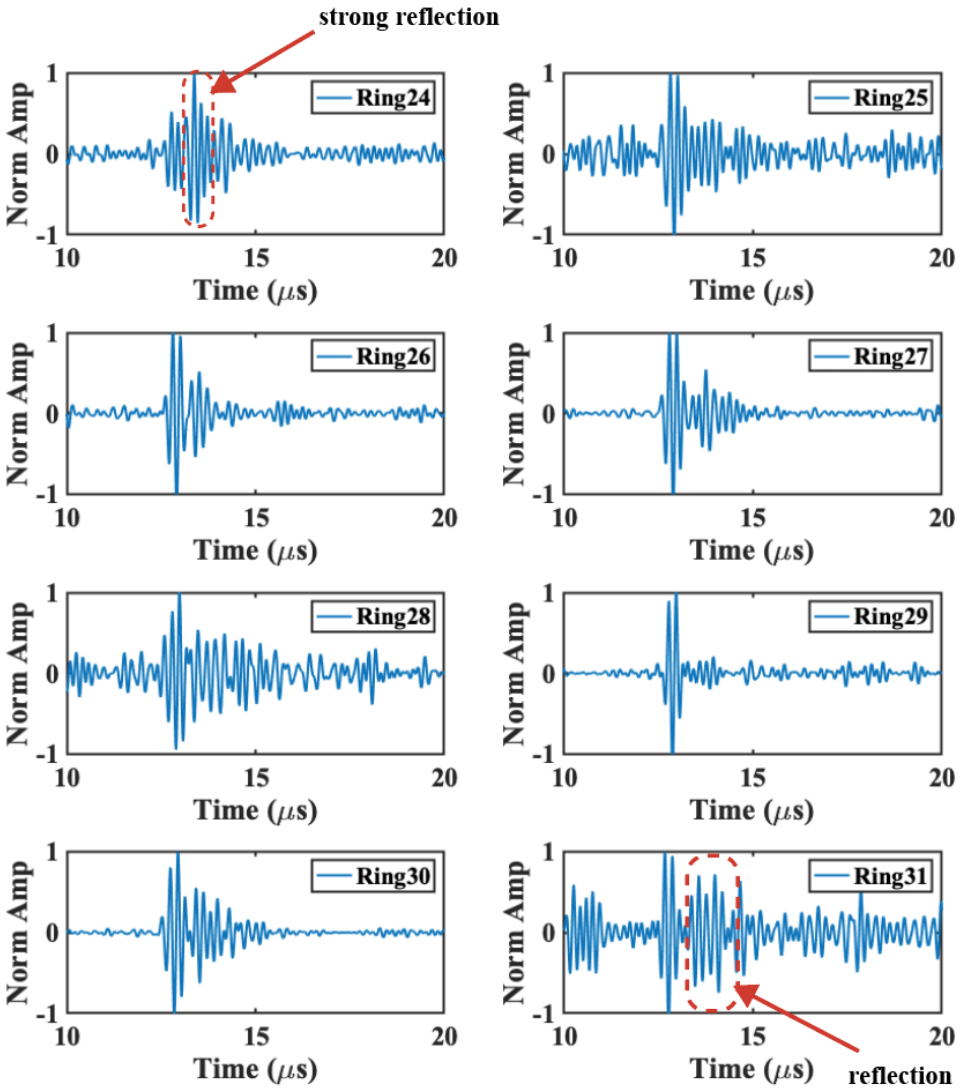

Figure 5.16: Filtered (BPF: 2.5MHz – 7.5MHz) time-domain responses of resonance locked MRRs to a pulsed excitation centered around 5MHz.

constitutes the first demonstration of a real-time, multi-channel WDM optical ultrasound receiver [23, 24, 26].

It can be seen that some of the acquired waveforms are rather irregular compared to the usual N-shaped ultrasonic pulse behavior, an artefact that can be attributed to multi-path interference (e.g. reflections off of the fiber block). Even though more complicated reconstruction algorithms could be applied to recover the signal from those cells [113], here we will completely exclude them from the delay and sum beamforming process. To acquire a beam profile we summed the bandpass filtered time-domain outputs of all 8 rings while sweeping the delay settings. The ADC sample rate of 50MHz translates to a delay resolution of 20ns, which for a 5MHz ultrasonic frequencies corresponds to a steering resolution of:

$$\theta_{res} = \sin^{-1} \frac{\tau_{res} c}{d} \simeq 7.5^{\circ} \tag{5.2}$$

where τ_{res} is the delay resolution, $c = 1500$m/s the speed of sound in water, and $d = 220\mu$m the sensor pitch of the array.

To validate this steering resolution we repeated the same beamforming experiment, using the goniometer of Fig. 5.14 to change the angle of transmission. Three beam profiles corresponding to the PMUT transmitting at angles of 0°, 7.5°, and 15° are shown in Fig. 5.17 (a). There it can also be seen that without excluding the signals with strong reflections from the delay and sum process we get much wider beam profiles with significant sidelobes. This is due to the reflected parts of the signals experiencing multi-path interference correlating with the main reception parts of the rest of the signals. Excluding the two signals with the strongest interference from the delay and sum, we get the improved beam profile of Fig. 5.17 (b). On

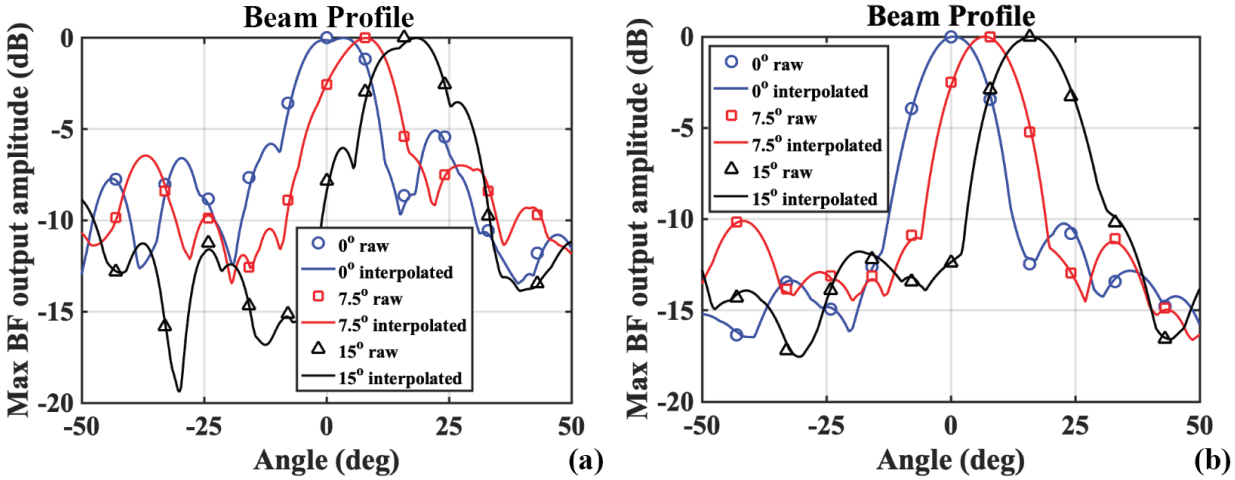

Figure 5.17: (a) Beam profiles using the time-domain responses of all 8 MRRs, (b) and only the 6 MRRs with the smallest reflections.

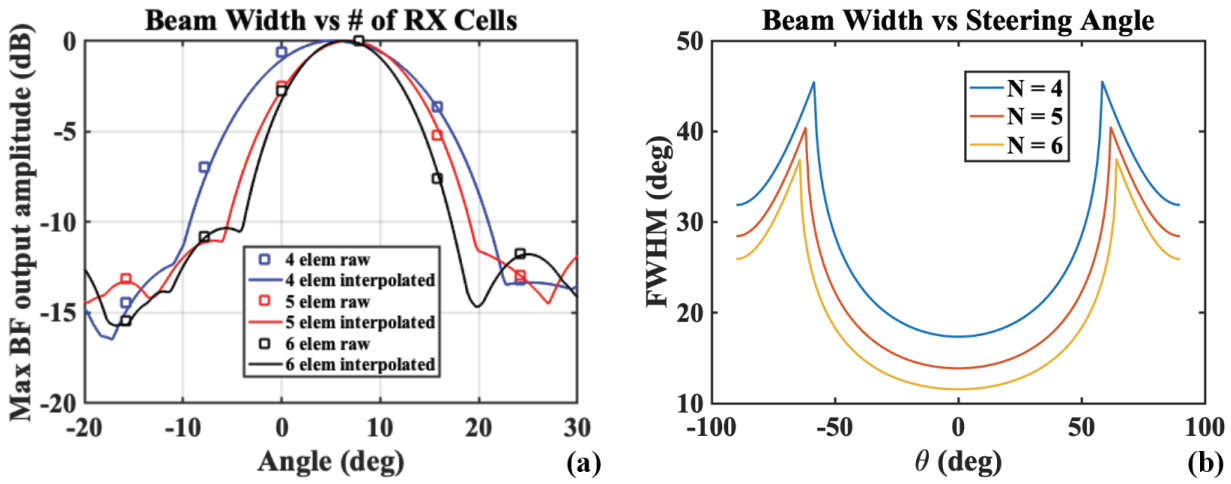

Figure 5.18: (a) Measured beam profiles acquired using 4, 5, and 6 MRRs at a 7° PMUT transmission angle. (b) Theoretical beam width vs steering angle.

both waveforms the peaks of the beam profiles correspond well with the transmitter angle. The "interpolated" profiles are acquired by interpolating the filtered time-domain signals of Fig. 5.16 and then applying the same delay and sum algorithm, and they provide a smoother delay (or equivalently angular) resolution.

Finally, we validated that the lateral resolution ($\text{FWHM}_{\text{beam}}$) of the beam profiles is close to what is theoretically expected when only the cleanest signals are used. Fig. 5.18, shows zoom-ins of the beam profiles obtained with 4, 5, and 6 receiving MRRs, as well as theoretical beam widths for the same number of elements, frequency and sensor pitch. The theoretical $\text{FWHM}_{\text{beam}}$ can be found as [114]:

$$\text{FWHM}_{\text{beam}} = \cos^{-1}\left(\sin\theta - \frac{2.78}{kNd}\right) - \cos^{-1}\left(\sin\theta + \frac{2.78}{kNd}\right) \tag{5.3}$$

where θ is the steering angle, k the wavenumber of ultrasound, and N the number of elements in the array. Table 5.1 shows the expected and theoretical beam width values for a transmission angle of 7°, where good agreement between measurement and theory is observed.

This experiment has not yet been expanded to the whole PD-MRR array, since the grating coupler loss combined with the available optical power per mode of the comb laser result in very low receiver sensitivity. However, it is not expected to be very challenging to expand to 2-D by simply increasing the available optical power (e.g through the use of a BOA) and applying the same locking algorithm to all the rings in the array. At the same time, this beamforming experiment, combined with the remoted ultrasound sensing demonstration of Section 5.3.2, opens the path towards a full 2-D dual-chip architecture, once the coupling losses and resonance misalignment issues are corrected.

5.3.4 Reflection Imaging Experiment

The last experimental demonstration was a reflection imaging experiment. To create a reflection off a 3-needle target that is commonly used as an ultrasound imaging phantom, we modified the water tank design such that a PMUT could be screwed on its side. Then we taped 3 needles to a rod that was suspended over the EPSoC taking the place of the piezo transducer in the previous experiments. The needles were spaced approximately 3mm and 5mm to one another. A PD-MRR with the heater turned fully ON to enhance the responsivity was interrogated by a CW laser parked on the blue side of the Lorentzian.

The bandpass filtered time-domain received waveform as well as the experimental setup are shown in Fig. 5.19. The difference in the time-of-arrival between the received reflections can be used a sanity check for this experiment and is consistent what is expected given the needle spacing and assuming the speed of ultrasound in water is $c = 1500$m/s.

Table 5.1: Measured and theoretical beam FWHM (transmission angle: 7°)

# of Elements	Measured (deg)	Theoretical (deg)
4	12.8	11.5
5	14.2	14
6	18.1	17.5

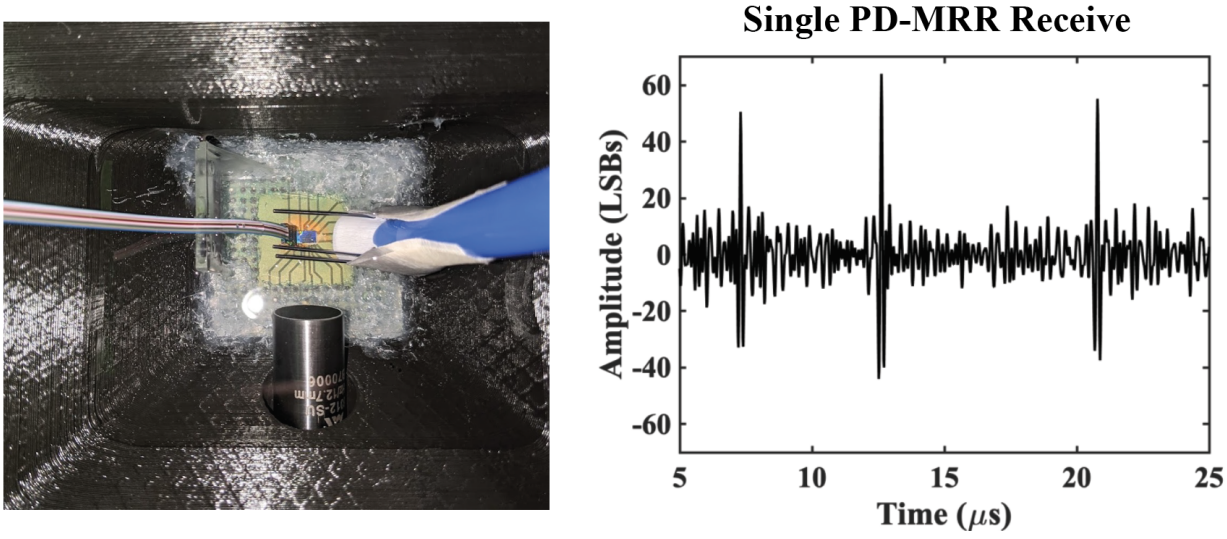

Figure 5.19: Reflection imaging experimental setup (left), Single PD-MRR filtered (BPF 2.5-7.5MHz) time-domain responses (right).

5.4 Discussion

5.4.1 Power and Area Breakdowns

Having demonstrated both remote and real-time WDM ultrasound sensing we will now revisit the power and area specifications. Fig. 5.20 presents a power and area breakdown for both the receiver and sensing elements.

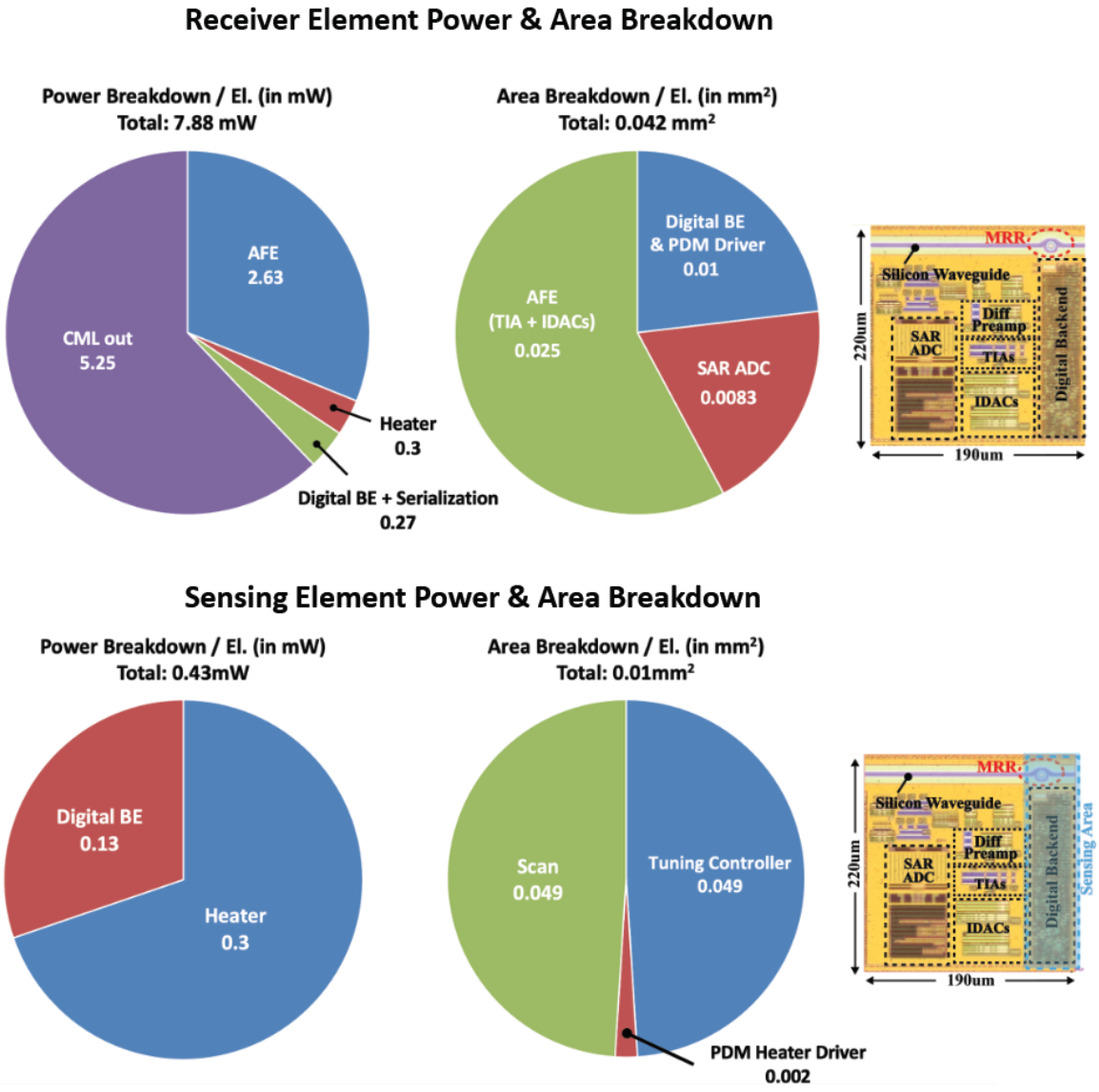

Figure 5.20: Power and area breakdowns for the receiver (top) and sensing (bottom) elements.

The receiver element area is dominated by the TIA and I_{DAC}s, while the power consumption by the CML output stages. Even though the power budget of those cells does not have a strict restriction, they can conceivably be replaced by low power LVDS transmitters [115] in future implementations, to further reduce the overall system dissipation. It should be noted that the receiver area is comparable to that of pitch-matched PMUT and CMUT endoscopic ultrasound implementations [32, 116].

More importantly though, the remote sensing operation allows us to extrapolate the power and area numbers for a minimized sensing unit, which would only require the resonance control digital logic area indicated in Fig. 5.20, leading to a record low $\mathbf{0.01mm^2}$. The power consumption of such an element would be dominated by the embedded heaters used to tune the MRR resonance. The 0.68pm/μW tuning efficiency of the platform allows to shift the MRRs by 0.2nm (half of the comb laser spacing) consuming only 0.3 mW of power per MRR, while the digital tuning circuitry consumes another 0.13 mW per MRR. The total power consumption of **0.43 mW** allows us to implement arrays that require less than the 0.5W specification set in Section 4.1.

5.4.2 Comparison with the State of the Art

Table 5.2 compares our work with the state of the art. It can be seen that our EPSoC achieves record high power efficiency and area density, while being the first optical ultrasound receiver implementation that offers an 8 channel reduction through real-time WDM. It also constitutes a unique single chip solution in a commercially available CMOS-SOI process, requiring no 3-D integration of the transducer on top of the ASIC. The measured SNDR is 25.5dB at -6.7dBFS at a transimpedance gain of 700kΩ, meaning that at the lowest gain setting, the electronic dynamic range will be $DR_{el} = 25.5+6.7+20\log(700k/50k) = 55.12dB$. This value is higher than the 46.2dB calculated in Chapter 4 due to the reduced Q-factor and R_{PD} values, which imply that the same excitation will result in a lower sense current, making the output harder to saturate. The SNDR remains limited by shot noise from the PD-MRR diode and I_{DAC} thermal noise at the input of the AFE as was discussed in Chapter 4. At the same time, the increased sensor density of our EPSoC can further improve the SNDR. Seeing as the noise sources are uncorrelated, the SNDR is expected to improve $\propto \sqrt{N}$, where N is the total number of sensors used to form an ultrasonic image. Thus, an array comprised of 1000 sensors, can get 10dB SNDR benefit, making for >30dB instantaneous SNDR, even at the highest gain settings. Combined with the gain tunability and operation mode switching offered by the R_f and I_{DAC}s respectively, the goal of >80dB SNDR set in Section 4.1 can be met. At the same time, it can be seen that the NEP of our implementation is rather high compared to state of the art, which can be attributed primarily to the high current noise at the TIA input. This drawback can also be alleviated through increasing the element count in the array, as well as improving the sensitivity of the detector, since $NEP = \frac{I_{n,tot}}{S_{int}S_{phot}}$. Improving the detector sensitivity will be discussed in Chapter 6.

Table 5.2: Comparison with the state of the art

Reference	JLT '15 [18]	JSSC '17 [41]	VLSI '19 [36]	**This Work**
Process [nm]	Custom MEMS	28 SOI	180LV	45 SOI
Transducer	MRR	CMUT	PMUT	MRR
Transducer Size [μm]	60	250	250	**10**
Integration Method	Passive	Flip-Chip	3-D Direct	**Monolithic**
Transducer BW [MHz]	350	10	5	>30
Delay Resolution [ns]	NA	8.33	30	20
NEP [kPa]	0.1	0.12	-	2.4
NEP density [Pa/$\sqrt{\text{Hz}}$]	0.006	0.037	-	0.48
SNDR [dB]	NA	58.9†	49.8‡	25.5††
Channel Reduction	Single Sensor	16	2	8
Power / Sense el. [mW]	NA (off-chip detection)	17.5	1.54	**0.43**
Power / Rx el. [mW]				7.88
Area / Sense el. [mm^2]	NA (off-chip detection)	0.041	0.023	**0.01**
Area / Rx el. [mm^2]				0.042

† Peak, measured at 64-ch beamformer output, ‡ Peak, †† Measured at -6.7dBFS.

5.5 Chapter Summary

Electro-optical MRR-based ultrasound sensing experiments utilizing a fully integrated electronic-photonic system-on-chip (EPSoC) have been presented in this chapter. Electronic-photonic packaging has been a non-trivial part of enabling these experiments, since a 5-step procedure was required before the chip could be incorporated in our measurement setup. A NEP of 2.4kPa, close to the set target was achieved, combined with a record low area and a power consumption that is the second best reported in literature. The sensing element power consumption of 0.43mW, allows integration of >1000 elements in the sensor, meeting the specification set in Chapter 4.

Ultrasound sensing experiments proving the concepts introduced in Section 4.2 have also been demonstrated. We have thus showcased the feasibility of real-time 2-D array remoted optical ultrasound sensing with local channel reduction performed at zero area and power cost through WDM MRR rows. The sensitivity of the remoted optical ultrasound scheme has been severely degraded due to the coupling losses coming with in-house alignment of the fiber blocks. Additionally, a reflection imaging experiment was carried out despite the moderately low SNDR of 25.5dB at -6.7dBFS. To improve upon this number we need to lower the input noise floor of our system (i.e. the NEP), while maintaining the same output swing. One way to achieve this, is through the design of a lower noise AFE in the next implementation. Another, which will be explored in the next chapter, is to increase the sensitivity of our sensor.

Chapter 6

High Sensitivity Architectures

This chapter explores avenues to improve the sensitivity of our EPSoC system in a future implementation. Three different alternatives, namely coherent sensing, high-Q MRRs, and the addition of a sensitivity enhancement membrane are discussed. Coherent sensing takes advantage of the steeper slope of the phase transfer function of the MRR, while MRRs with higher Q factors increasing the photonic sensitivity, S_{phot}, have been designed and measured. Finally, post-processing of the EPSoC to add a membrane that could enhance the interaction of the ultrasound field with the optical mode is a promising option, already successfully presented in literature with remarkable results [20]. Incorporating these techniques, we anticipate our EPSoC 2.0 implementation to be $\sim$100 times better in terms of sensitivity, making it competitive with state of the art MRR-based sensors, while retaining the advantages of high bandwidth, area and power density, and real-time 2-D array interrogation capability.

6.1 Coherent Detection

Using the phase information of the optical EM wave in addition to the amplitude information in order to enhance the detector sensitivity has been proposed in [117]. The ring assisted Mach-Zender Interferometer (RAMZI) that will be utilized in this coherent sensing scheme is shown in Fig. 6.1. An insonified MRR on the sense chip will modulate the input light, which will then be beat against a phase offset replica of the original laser input using a 2x2 adiabatic coupler. Subtracting the two outputs of the coupler after detection will give us the desired signal I_{sense}, containing the ultrasound modulation information. Even though Fig. 6.1 shows a single pair of sensor-PD MRRs, this architecture can be extended to a WDM row of MRRs interrogated by a comb laser, and is also compatible with remoted optical ultrasound sensing. One such WDM row has been implemented in our first generation EPSoC and its characterization is pending.

To theoretically understand the expected benefit consider the electric field transfer func-

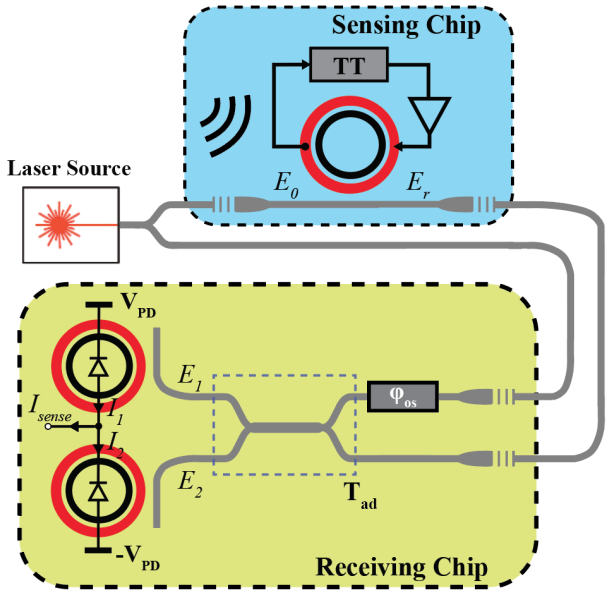

Figure 6.1: RAMZI coherent sensing scheme.

tion of an APF ring [69]:

$$\frac{E_r}{E_0} = \frac{\alpha - te^{-j\phi}}{1 - t\alpha e^{j\phi}} \cdot e^{j(\pi+\phi)} = A_r e^{j\theta_r}, \tag{6.1}$$

where α, t, ϕ, are the single-pass amplitude transmission, self-coupling coefficient, and round-trip phase-shift of the ring as defined in Section 3.1, and we have defined A_r and θ_r as the magnitude and phase of the APF E-field transfer function respectively. The adiabatic coupler transfer function is:

$$\mathbf{T_{ad}} = \begin{bmatrix} \frac{1}{\sqrt{2}} & \frac{j}{\sqrt{2}} \\ -\frac{j}{\sqrt{2}} & \frac{1}{\sqrt{2}} \end{bmatrix}, \tag{6.2}$$

Combining equations 6.1, 6.2, while normalizing with respect to the laser power and PD responsivity, and neglecting any waveguide losses we get that the sensor output, I_{sense}, will be: *

$$I_{sense} \propto \frac{|E_1|^2 - |E_2|^2}{|E_0|^2} = A_r \sin(\theta_r - \phi_{os}), \tag{6.3}$$

*Coupler losses are neglected as well since they equally mix through the adiabatic coupler. Also note, that the remoted sense-PD MRR pair sensor, has to pay the same penalty of 3× the coupling losses. Laser forwarding increases the available power at the detector, thus providing additional sensitivity benefit to the one outlined in this analysis. The exact benefit depends on the exact number of the grating coupler loss.

where ϕ_{os} is the phase offset added by the reference arm of the RAMZI. The normalized sensitivity of this architecture, will thus be:

$$S_{\text{norm}} = \frac{\partial(|E_1|^2 - |E_2|^2)}{|E_0|^2 \partial\phi} = A'_r \sin(\theta_r - \phi_{os}) + A_r \cos(\theta_r - \phi_{os})\theta'_r. \tag{6.4}$$

For this device to be optimally operated, we need to ensure that for any given pair of A_r, θ_r, which depend on the self-coupling coefficient t, we pick the value of ϕ_{os} that maximizes S_{norm}. To obtain the optimal ϕ_{os} we differentiate S_{norm} once more and get:

$$\phi_{os,opt} = \theta_r - \tan^{-1}\left(\frac{C}{B}\right), \tag{6.5}$$

where $B = A'_r - A_r\theta'$, $C = 2A'_r\theta'_r$.

Plugging the value of $\phi_{os,opt}$, from Eq. 6.5 into Eq. 6.3 we can compute the S_{norm} while sweeping the coupling coefficient of the sensing ring. In Fig. 6.3 we plot the result of that sweep together with the optimal sensitivity of a simple APF from Fig. 3.2 (d). We can observe that the difference in peak sensitivity is 30% in agreement to the analysis performed in [117], and that optimal occurs at critical coupling compared to the half-critical coupling condition that optimized an APF ring. This extra sensitivity also offers an extra degree of freedom in our design, since it can alternatively be traded of for power. It has been shown in [117] that the power circulating in the sensor-MRR of the optimized RAMZI can be reduced by 25% while maintaining the same sensitivity as an APF sensor-PD MRR.

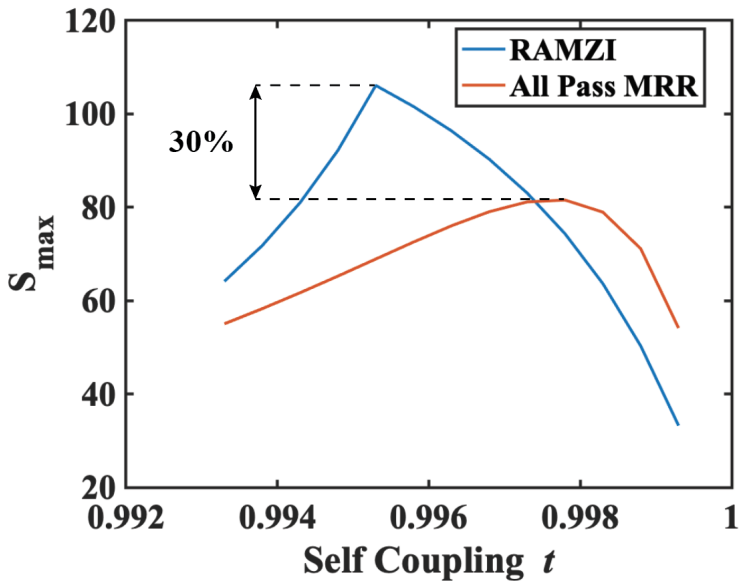

Figure 6.2: Maximum sensitivity vs coupling coefficient of a RAMZI and a single all-pass sense-MRR showing the superiority of the first.

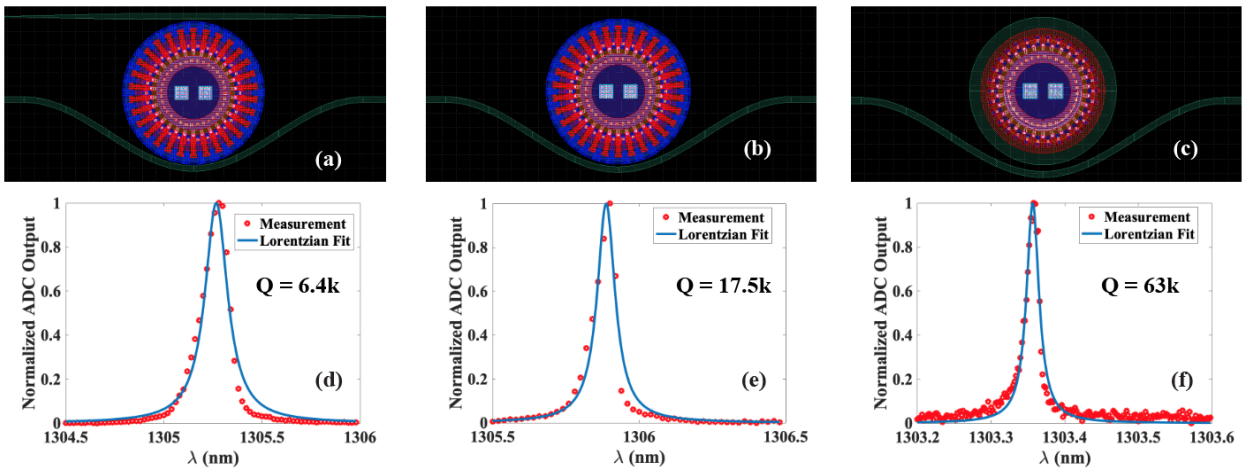

Figure 6.3: High-Q MRRs: (a)-(c): Layouts of MRRs with different doping variants (d)-(e): Corresponding Lorentzians with Q-factors of 6.4k, 17.5k, and 63k respectively.

6.2 High-Q Rings

Another means of further boosting receiver sensitivity and reducing NEP is the use of higher quality factor rings. Passive ring resonators with Q = 200k have been measured in this platform. Note that an increase in the ring quality factor translates to a proportional increase in sensitivity (Eq. 3.11). However, stabilization of these rings is one of the biggest challenges, since high probing power can cause them to oscillate due to free carrier absorption effects. Thus, we have experimented with hybrid MRR variants, between the currently used sensor which has interdigitated p-n doped spokes that deplete the waveguide region of generated carriers and the passive, high-Q MRRs, to ensure high sensitivity and stable operation are achieved. The photocurrent collected from the p-n junction can also be used to tune the ring resonance. The layouts of three ring variants with different doping variants are shown in Fig. 6.3, along with their measured responses. As a measure of comparison, the Q-factors of the MRRs in our EPSoC demonstration in Chapter 5 was 6k for the PD-MRR ring and 10k for the sensor-MRR, while the Q-factor of the improved MRRs was measured to be more than 60k. Once integrated in the EPSoC 2.0 sensor, these MRRs would increase the sensitivity up to 10x.

6.3 Sensitivity Enhancement Membrane

Increasing the evanescent field can significantly increase detector sensitivity as shown by measurement and simulation in this platform for purposes of label-free biosensing [118]. In order to do so we plan to investigate three different avenues:

(a) Controllably etch through the buried oxide (BOX) of the silicon die. This will make sure that the optical mode is more exposed and any difference in the waveguide thickness can cause a higher change in the refractive index and consequently a higher resonant shift. As shown in [118], the sensitivity of dies in this platform is improved by 7x when a partial, 100nm etch of the BOX is performed.

(b) Coat the exposed waveguides with a polymer type material that will have a Young's modulus of ∼2GPa [119] compared to the ∼64GPa of SiO_2 [120]. This is expected to allow for a ∼32x higher modulation of the evanescent field than the one currently observed with BOX on top of the silicon waveguides since the BOX thickness modulation is proportional to the resonant wavelength shift.

(c) Other groups have experimented with 3-D integrating an SiO_2 membrane on top of the MRR sensors leaving a tiny air gap in-between [57]. Using the modulation of the air gap rather than the waveguide height to detect ultrasound is expected in simulation to increase sensitivity by 2 orders of magnitude compared to the current state-of-the-art [65]. This method, though expected to have very large sensitivity is also relying on a mechanical resonance of a membrane and will therefore be susceptible to the sensitivity bandwidth trade-off existing in the PMUT and CMUT approaches. Nonetheless, it will have superb sensitivity and all of the benefits of an optical implementation.

6.4 Chapter Summary

Quantifying the sensitivity enhancement techniques above, combining high-Q MRRs in a coherent sensing scheme, with sensor chips having partially etched BOX could **boost sensitivity by up to almost 2 orders of magnitude** (up to $1.3 * 10 * 7$), with **zero overhead in die area and system complexity of the sensor chip** and minimal overhead on the receiver chip. Such an implementation would be on par with current state-of-the-art MRR based approaches [65] in terms of sensitivity, while maintaining much higher BW. Additionally, adopting the polymer coating or MEMS membrane in generations beyond EPSoC 2.0 could further increase intrinsic sensitivity by 10-100x making for the most sensitive MRR ultrasound sensor by today's standards. It should be noted though that the MEMS membrane approach is expected to come with BW degradation and increased complexity.

Chapter 7

Conclusions

In this chapter the key contributions of this thesis will be summarized, followed by future research directions that can improve upon the shortcomings of this first electronic-photonic integrated system-on-chip (EPSoC) implementation. Finally, some conclusions regarding the potential of optical imaging systems in endoscopic and photoacoustic ultrasound will be drawn.

7.1 Key Contributions

Next generation 3-D endoscopic ultrasound imaging requires high sensor density and ultra-low power consumption per sensing element to ensure maximum lateral resolution and SNR are achieved without violating safety regulations regarding probe heat-up inside the body. This thesis has presented a novel, alternative approach towards building dense ultrasound beamforming receiver arrays, capable of tackling miniaturized endoscopic probe specifications. The fabricated EPSoC uses microring resonator ultrasound sensors instead of the traditional piezoelectric or capacitive micromachined ultrasound transducers. This work has outlined the process of building a proof-of-concept electronic-photonic SoC, focusing on multiple system aspects from platform choice and device operation to circuit design and system architecture.

The main contributions of this thesis can be organized as follows:

- The fundamental transduction mechanisms involved in optical MRR-based ultrasound sensing have been analyzed, and sensitivity metrics to evaluate the performance of MRR ultrasound sensors have been introduced. Among waveguide deformation, ring elongation and opto-elastic modulation, preliminary experimental results and theoretical analysis have shown the first effect to dominate the MRR response.

- The design procedure for the implementation of a first-of-its-kind EPSoC that will be able to meet the stringent power, area, NEP, and DR specifications of miniaturized

endoscopes has been outlined. This was achieved through a combination of architectural and circuit design choices. On the system architecture side, a dual-chip sensor receiver scheme has been chosen to enable dense, low power 2-D sensor arrays. On the circuit design side, a mixed-signal block comprised of a resistive feedback TIA with programmable gain was employed to achieve low NEP, and high overall sensitivity, with moderate DR. Additionally, an on-chip digital resonance tuning controller was designed to enable WDM ultrasound sensing. A methodology for the co-integration of electronics and photonics in our zero-change monolithic process has also been presented.

- Demonstration of optical ultrasound sensing in both remoted sensor-receiver and real-time multi-ring WDM modes has been carried out. These experiments have proven the feasibility of a dense, low power 2-D multi-MRR array based on a dual-chip sensor-receiver architecture. A single sensor cell using a PD-MRR detector has also been characterized, verifying the target NEP is met, and accomplishing competitive sensitivity in terms of [mV/kPa]. The moderately low SNDR can be offset by averaging the responses of the multiple sensing elements in the beamforming array.

- Avenues towards improving the sensitivity of this first generation EPSoC have been proposed and theoretically analyzed. Using coherent ultrasound sensing, and optimizing the Q-factors of the MRRs, combined with a partial etch of the buried oxide can lead to a two orders of magnitude boost of the currently measured system sensitivity.

In summary, we have demonstrated the first optical ultrasound receiver array based on MRRs that is fully integrated with receiver circuitry on the same die. The high area and power efficiency it achieves, prove MRR-based ultrasound reception using a dual-chip sense-RX architecture to be a competitive alternative for modern endoscopic applications.

7.2 Future Directions

Given that this is the first implementation of a fully integrated EPSoC there are still plenty of research directions to explore in future realizations of this optical MRR-based ultrasound imaging system. The most impactful ones are listed below:

- **Increased Sensitivity Schemes:** Incorporating the sensitivity enhancement techniques discussed in Chapter 6, in our EPSoC 2.0 implementation will have a tremendous impact on the sensitivity of the system. Also, given that shot noise at the TIA input is the dominant noise source, increasing the sensitivity will not affect the output referred noise, thus proportionally reducing the NEP. A two orders of magnitude improvement in the NEP would bring it in the Pa range, in par with the current state-of-the-art MRR sensors.

- **Lower Noise & Higher Dynamic Range Receiver:** On-chip averaging is a technique that can be used to lower thermal noise impact. This can be achieved by running the ADC at a higher rate, while decoupling the rate of the ADC from that of the serialized output. A more sophisticated on-chip clock distribution scheme that will include multiplexing can be used for that purpose.

  Additionally, replacing the resistive feedback TIA with capacitive feedback topologies [102, 103] can potentially increase the DR of our receiver, at the expense of additional area. This area penalty can be afforded due to the remote nature of the receiver.

- **Increased Sensor Density:** Figure 7.1 shows the layout of a denser, 128-element 2-D array comprised of high-Q sensing rings spaced at a 50µm pitch. Since the first EPSoC was meant to be a proof of concept, the same mixed-signal block is used to interface with both the sense and PD MRRs, in order to streamline the design, constraining the pitch to 220µm. In future implementations, however, the sensing chip only requires the thermal tuning circuitry and the sense MRR which, in EPSoC 1.0, take up $< 0.01\text{mm}^2$ of area. Here, a somewhat conservative pitch of 50µm (resulting in 0.0025mm^2 sensing element area) is selected to make sure that there is no thermal cross-talk between adjacent sensing rings. This layout is generated using the python-based Berkeley Photonic Generator (BPG) [72], an open-source photonic design framework developed by our group, which allows quick iteration and flexibility at design time.

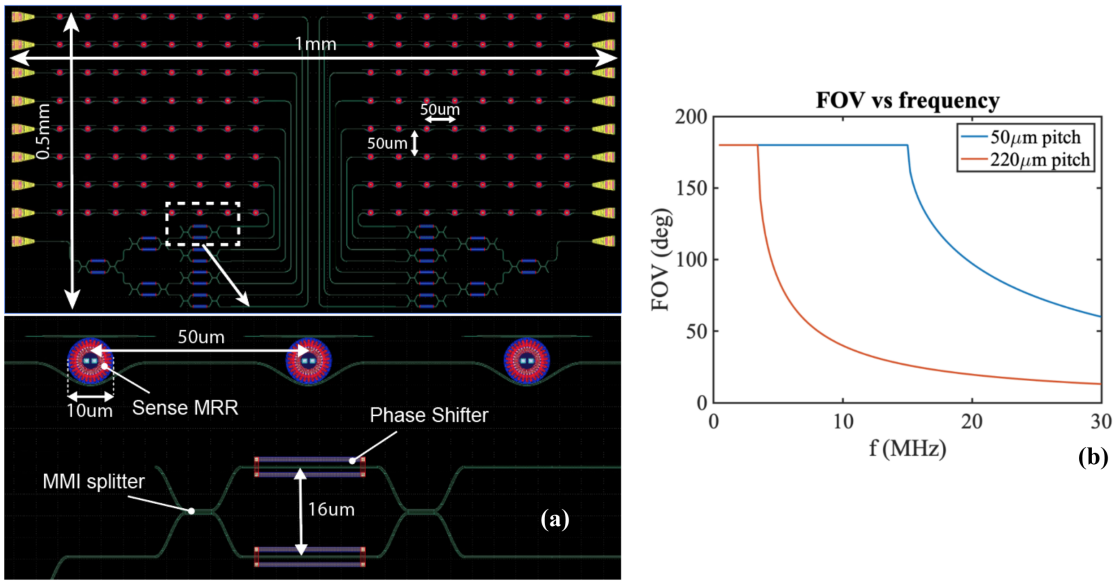

Figure 7.1: (a) Compact BPG generated layout with 50µm MRR pitch, corresponding to $\frac{\lambda}{2}$ of 15MHz ultrasonic signals and a record low sensing element area of 0.025mm^2, (b) Field-of-view vs ultrasound frequency.

With respect to beamforming, reducing the sensor pitch comes with the benefit of improved field of view. Fig. 7.1 (b), illustrates that the proposed denser array can steer the beam across entire hemisphere for frequencies up to 15MHz compared to the 3.4MHz of the current implementation. Thus, the proposed denser array is expected to significantly improve the axial resolution due to the ability to fully steer the beam at much higher frequencies.

With respect to noise, averaging the responses of N array elements will lead to an improvement $\propto N$ given the white profile of the dominant noise sources.

- **Photoacoustic Imaging:** Photoacoustic (PA) imaging has been gaining popularity in the fields of vascular biology, oncology, dermatology, ophthalmology and cardiology with applications ranging from breast cancer screening, and interventional cardiac procedures, to monitoring of metabolic and genetic functions. This technique uses optically generated ultrasonic waves to form an image and takes advantage of the absorption coefficient gradient in the object imaged [121, 122, 123]. In the case of cancer this can be healthy and cancerous tissue, in the case of genetic process monitoring it can be different biomolecules. Compared to purely optical techniques, PA imaging has the advantage that it receives the much less scattered acoustic waves, so it can penetrate deeper into tissue. It is also ideally suited to image evolving breast cancer where micro-vascularization and high blood concentration is a characteristic trait, and therefore, big optical absorption contrast between regular tissue and cancerous tissue is expected. Consequently, malignancies can be detected by direct measurements of hemoglobin concentration and blood oxygenation. This method is minimally invasive since the patients are not exposed to radiation or injected with contrast agents [124, 125]. The development of an optical ultrasound receiver will be very useful for this application for several reasons: a) the bandwidth of interest in PA imaging is usually in the hundreds of MHz which requires multiple piezo-electric transducers of different central frequencies to be combined, b) increased sensitivity is particularly useful for PA imaging receivers since the attenuation of ultrasound is proportional to $\frac{1}{f^2}$ and as we move to higher bandwidth and higher axial resolutions the received signal is expected to be significantly lower, c) it greatly simplifies the system by getting rid of all electrical connections and interfaces that the conventional receivers need.

- **Multi-Modal All-Optical Ultrasound:** The next natural step to investigate is combining PA imaging with traditional ultrasound and exploiting the benefits of both modalities to render a high-quality 3-D volumetric image. Since ultrasonic imaging can capture structural details and has higher imaging depth, it can enhance the PA based image which will use the high optical absorption contrast to capture the finer features. One proposed way to achieve this multi-modal imaging is through the use of a dichroic filter that absorbs in a certain wavelength and is transparent at another one [74]. Using two separate pulsed laser sources in each mode can enable switching between conventional ultrasound and photoacoustics. Working towards that direction,

improved efficiency photoacoustic ultrasound generation has been demonstrated in the past decade with two parameters being the key: a) use of materials with strong optical absorption, high thermal conductivity, and low optical reflectivity, and b) design the film thickness to equal the optical absorption length [126, 127, 128]. In [126] ultrasonic pulses of ∼12MPa peak-peak have been generated using carbon nanofibers coated with a PDMS thin film under a laser fluence of 3.71mJ/cm^2. Integrating that technology in a transmitter with a 250x250μm^2 aperture and a 1kHz pulse repetition rate, 12MPa ultrasound pulses can be generated while dissipating only 2.3mW. Combining such a transmitter pressure range with a receiver achieving NEP in the Pa range, would allow an imaging depth of > 5cm for 5MHz ultrasonic pulses (given that ultrasound attenuation in tissue is approximately 1dB/(MHz·cm)). We believe that MRR-based receiver arrays, 3-D integrated with efficient PA ultrasound generation structures in implementations beyond EPSoC 2.0 will be great candidates for next-generation all-optical multi-modal ultrasound imaging probes, targeting endoscopic and whole-body POC imaging applications alike.

7.3 Conclusions

In conclusion, this thesis has demonstrated the feasibility of using optical MRR sensor arrays in high density and ultra-low power ultrasound imaging systems. Such systems are suitable for both endoscopic and photoacoustic imaging environments, where the conventional ultrasound transducer technologies are facing insurmountable obstacles in terms of area, power, and congestion of electrical interconnects. Moving ultrasound sensing from the electrical to the optical domain, allows utilization of miniaturized, sensitive detectors that can be elegantly interfaced with the image processing units through optic fiber bundles. Additionally, the use of a commercially available CMOS process, enables co-integration of the sensors with CMOS receiver circuitry on a single chip solution, compatible with POC diagnostic standards. A first prototype of this research vision has been successfully demonstrated, paving the path towards a portable and compact ultrasonic probe that would constitute a vital tool in the treatment of very important diseases.

Bibliography

[1] Sherry L Murphy et al. "Mortality in the united states, 2017". In: (2018).

[2] Ivan S Salgo. "Three-dimensional echocardiographic technology". In: *Cardiology clinics* 25.2 (2007), pp. 231–239.

[3] Neslihan Ozmen et al. "Comparing different ultrasound imaging methods for breast cancer detection". In: *IEEE transactions on ultrasonics, ferroelectrics, and frequency control* 62.4 (2015), pp. 637–646.

[4] Tomoo Inoue et al. "Three-dimensional ultrasound imaging of breast cancer by a real-time intraoperative navigation system". In: *Breast Cancer* 12.2 (2005), pp. 122–129.

[5] Freddie Bray et al. "Global cancer statistics 2018: GLOBOCAN estimates of incidence and mortality worldwide for 36 cancers in 185 countries". In: *CA: a cancer journal for clinicians* 68.6 (2018), pp. 394–424.

[6] Arif Hussain et al. "Multi-organ point-of-care ultrasound for COVID-19 (PoCUS4COVID): international expert consensus". In: *Critical Care* 24.1 (2020), pp. 1–18.

[7] Emanuele Pivetta et al. "Self-Performed Lung Ultrasound for Home Monitoring of a Patient Positive for Coronavirus Disease 2019". In: *Chest* 158.3 (2020), e93–e97.

[8] Hamid Shokoohi et al. "Lung ultrasound monitoring in patients with COVID-19 on home isolation". In: *The American Journal of Emergency Medicine* 38.12 (2020), 2759–e5.

[9] Joseph R Pare et al. "Point-of-care lung ultrasound is more sensitive than chest radiograph for evaluation of COVID-19". In: *Western Journal of Emergency Medicine* 21.4 (2020), p. 771.

[10] Yanick Baribeau et al. "Hand-held point of care ultrasound probes–the new generation of POCUS". In: *Journal of Cardiothoracic and Vascular Anesthesia* (2020).

[11] Jan G Laufer et al. "In vivo preclinical photoacoustic imaging of tumor vasculature development and therapy". In: *Journal of biomedical optics* 17.5 (2012), p. 056016.

[12] *Medmovie TEE webpage*. `https://medmovie.com/library_id/3255/topic/ahaw_0186i/`. Accessed: 2021-03-02.

[13] Sung-Jin Hong et al. "Effect of intravascular ultrasound–guided vs angiography-guided everolimus-eluting stent implantation: the IVUS-XPL randomized clinical trial". In: *Jama* 314.20 (2015), pp. 2155–2163.

[14] Kyoko Otani et al. "Assessment of the aortic root using real-time 3D transesophageal echocardiography". In: *Circulation Journal* 74.12 (2010), pp. 2649–2657.

[15] PC Beard and TN Mills. "Extrinsic optical-fiber ultrasound sensor using a thin polymer film as a low-finesse Fabry–Perot interferometer". In: *Applied optics* 35.4 (1996), pp. 663–675.

[16] Rehman Ansari et al. "All-optical forward-viewing photoacoustic probe for high-resolution 3D endoscopy". In: *Light: Science & Applications* 7.1 (2018), pp. 1–9.

[17] Huibo Fan et al. "Ultrasound sensing based on an in-fiber dual-cavity Fabry–Perot interferometer". In: *Optics letters* 44.15 (2019), pp. 3606–3609.

[18] Cheng Zhang et al. "Imprinted polymer microrings as high-performance ultrasound detectors in photoacoustic imaging". In: *Journal of Lightwave Technology* 33.20 (2015), pp. 4318–4328.

[19] Wouter Jan Westerveld. "Silicon photonic micro-ring resonators to sense strain and ultrasound". In: (2014).

[20] Wouter J Westerveld et al. "Sensitive, small, broadband and scalable optomechanical ultrasound sensor in silicon photonics". In: *Nature Photonics* 15.5 (2021), pp. 341–345.

[21] U. S. Food and Drug Administration (FDA). *Marketing Clearance of Diagnostic Ultrasound Systems and Transducers*. Ed. by Windows Phone Central. URL: `https://www.fda.gov/media/71100/download`.

[22] Panagiotis Zarkos, Olivia Hsu, and Vladimir Stojanović. "Ring resonator based ultrasound detection in a zero-change advanced cmos-soi process". In: *CLEO: QELS Fundamental Science*. JW2A–78. Optical Society of America. 2019.

[23] Christos Adamopoulos et al. "Lab-on-Chip for Everyone: Introducing an Electronic-Photonic Platform for Multiparametric Biosensing Using Standard CMOS Processes". In: *IEEE Open Journal of the Solid-State Circuits Society* (2021).

[24] Panagiotis Zarkos et al. "Fully Integrated Electronic-Photonic Ultrasound Receiver Array for Endoscopic Imaging Applications in a Zero-Change 45nm CMOS-SOI Process". In: *2021 Symposium on VLSI Circuits*. IEEE. 2021, pp. 1–2.

[25] Panagiotis Zarkos et al. "Monolithically Integrated Electronic-Photonic Ultrasound Receiver Using Microring Resonator". In: *CLEO: Science and Innovations*. Optical Society of America. 2021, STh1H–2.

[26] Panagiotis Zarkos et al. "Fully Integrated Electronic-Photonic Ultrasound Receiver Array for Endoscopic Applications in a Zero-Change 45nm CMOS-SOI Process". In: *IEEE Journal of Solid-State Circuits* (2022), in press.

[27] Ira O Wygant et al. "An integrated circuit with transmit beamforming flip-chip bonded to a 2-D CMUT array for 3-D ultrasound imaging". In: *IEEE transactions on ultrasonics, ferroelectrics, and frequency control* 56.10 (2009), pp. 2145–2156.

[28] Azadeh Moini et al. "Fully integrated 2D CMUT ring arrays for endoscopic ultrasound". In: *2016 IEEE International Ultrasonics Symposium (IUS)*. IEEE. 2016, pp. 1–4.

[29] Anshuman Bhuyan et al. "Integrated circuits for volumetric ultrasound imaging with 2-D CMUT arrays". In: *IEEE transactions on biomedical circuits and systems* 7.6 (2013), pp. 796–804.

[30] Ian Donald, John Macvicar, and TG Brown. "Investigation of abdominal masses by pulsed ultrasound". In: *The Lancet* 271.7032 (1958), pp. 1188–1195.

[31] Matthew I Haller and Butrus T Khuri-Yakub. "A surface micromachined electrostatic ultrasonic air transducer". In: *IEEE transactions on ultrasonics, ferroelectrics, and frequency control* 43.1 (1996), pp. 1–6.

[32] Chao Chen et al. "A Front-End ASIC With Receive Sub-array Beamforming Integrated With a 32×32 PZT Matrix Transducer for 3-D Transesophageal Echocardiography". In: *IEEE Journal of Solid-State Circuits* 52.4 (2017), pp. 994–1006.

[33] Thierry V Scohy et al. "A new transesophageal probe for newborns". In: *Ultrasound in medicine & biology* 35.10 (2009), pp. 1686–1689.

[34] S Blaak et al. "Design of a micro-beamformer for a 2D piezoelectric ultrasound transducer". In: *2009 IEEE International Ultrasonics Symposium*. IEEE. 2009, pp. 1338–1341.

[35] Deep Bera et al. "Three-dimensional beamforming combining micro-beamformed RF datasets". In: *2016 IEEE International Ultrasonics Symposium (IUS)*. IEEE. 2016, pp. 1–4.

[36] Jing Li et al. "A 1.54 mW/element 150μm-pitch-matched receiver ASIC with element-level SAR/shared-single-slope hybrid ADCs for miniature 3D ultrasound probes". In: *2019 Symposium on VLSI Circuits*. IEEE. 2019, pp. C220–C221.

[37] Qilong Liu et al. "A mixed-signal multiplexing system for cable-count reduction in ultrasound probes". In: *2015 IEEE International Ultrasonics Symposium (IUS)*. IEEE. 2015, pp. 1–4.

[38] Thomas M Carpenter et al. "Direct digital demultiplexing of analog TDM signals for cable reduction in ultrasound imaging catheters". In: *IEEE transactions on ultrasonics, ferroelectrics, and frequency control* 63.8 (2016), pp. 1078–1085.

[39] Thomas Lehrmann Christiansen et al. "Row-column addressed 2-D CMUT arrays with integrated apodization". In: *2014 IEEE International Ultrasonics Symposium*. IEEE. 2014, pp. 600–603.

[40] Kailiang Chen, Hae-Seung Lee, and Charles G Sodini. "A column-row-parallel ASIC architecture for 3-D portable medical ultrasonic imaging". In: *IEEE Journal of Solid-State Circuits* 51.3 (2015), pp. 738–751.

[41] Man-Chia Chen et al. "A pixel pitch-matched ultrasound receiver for 3-D photoacoustic imaging with integrated delta-sigma beamformer in 28-nm UTBB FD-SOI". In: *IEEE journal of solid-state circuits* 52.11 (2017), pp. 2843–2856.

[42] Kailiang Chen, Hae-Seung Lee, and Charles G Sodini. "A column-row-parallel ASIC architecture for 3-D portable medical ultrasonic imaging". In: *IEEE Journal of Solid-State Circuits* 51.3 (2015), pp. 738–751.

[43] Eberhard Brunner. "Ultrasound system considerations and their impact on front-end components". In: *Analog Devices* 36 (2002), pp. 1–19.

[44] Erwin J Alles et al. "A reconfigurable all-optical ultrasound transducer array for 3D endoscopic imaging". In: *Scientific reports* 7.1 (2017), pp. 1–9.

[45] Joseph A Bucaro, Henry D Dardy, and Edward F Carome. "Optical fiber acoustic sensor". In: *Applied optics* 16.7 (1977), pp. 1761–1762.

[46] Georg Wissmeyer et al. "Looking at sound: optoacoustics with all-optical ultrasound detection". In: *Light: Science & Applications* 7.1 (2018), pp. 1–16.

[47] PC Beard and TN Mills. "A 2D optical ultrasound array using a polymer film sensing interferometer". In: *2000 IEEE Ultrasonics Symposium. Proceedings. An International Symposium (Cat. No. 00CH37121)*. Vol. 2. IEEE. 2000, pp. 1183–1186.

[48] Edward Z Zhang and Paul C Beard. "A miniature all-optical photoacoustic imaging probe". In: *Photons plus ultrasound: imaging and sensing 2011*. Vol. 7899. International Society for Optics and Photonics. 2011, 78991F.

[49] Amir Rosenthal, Daniel Razansky, and Vasilis Ntziachristos. "High-sensitivity compact ultrasonic detector based on a pi-phase-shifted fiber Bragg grating". In: *Optics letters* 36.10 (2011), pp. 1833–1835.

[50] Georg Wissmeyer et al. "All-optical optoacoustic microscope based on wideband pulse interferometry". In: *Optics letters* 41.9 (2016), pp. 1953–1956.

[51] Tianxiong Wang et al. "All-optical photoacoustic microscopy based on plasmonic detection of broadband ultrasound". In: *Applied Physics Letters* 107.15 (2015), p. 153702.

[52] A Rostami et al. "A proposal for design of high-resolution and integrated 2-D array of ultrasound detector for imaging purposes based on optical MEMS". In: *Optomechatronic Systems Control III*. Vol. 6719. International Society for Optics and Photonics. 2007, 67190F.

[53] Saher M Maswadi et al. "All-optical optoacoustic microscopy based on probe beam deflection technique". In: *Photoacoustics* 4.3 (2016), pp. 91–101.

[54] Jorge J Alcoz, CE Lee, and Henry F Taylor. "Embedded fiber-optic Fabry-Perot ultrasound sensor". In: *IEEE transactions on ultrasonics, ferroelectrics, and frequency control* 37.4 (1990), pp. 302–306.

[55] Xiaoyi Zhu et al. "Ultrasonic detection based on polarization-dependent optical reflection". In: *Optics letters* 42.3 (2017), pp. 439–441.

[56] Claudio I Zanelli and Samuel M Howard. "Schlieren metrology for high frequency medical ultrasound". In: *Ultrasonics* 44 (2006), e105–e107.

[57] Wouter J Westerveld et al. "Opto-Mechanical Ultrasound Sensor based on Sensitive Silicon-Photonic Split Rib-type Waveguide". In: *2019 Conference on Lasers and Electro-Optics Europe & European Quantum Electronics Conference (CLEO/Europe-EQEC)*. IEEE. 2019, pp. 1–1.

[58] Edward Zhang, Jan Laufer, and Paul Beard. "Backward-mode multiwavelength photoacoustic scanner using a planar Fabry-Perot polymer film ultrasound sensor for high-resolution three-dimensional imaging of biological tissues". In: *Applied optics* 47.4 (2008), pp. 561–577.

[59] Turan Erdogan. "Fiber grating spectra". In: *Journal of lightwave technology* 15.8 (1997), pp. 1277–1294.

[60] Shai Tsesses et al. "Modeling the sensitivity dependence of silicon-photonics-based ultrasound detectors". In: *Optics letters* 42.24 (2017), pp. 5262–5265.

[61] Robert Nuster, Paul Slezak, and Guenther Paltauf. "High resolution three-dimensional photoacoustic tomography with CCD-camera based ultrasound detection". In: *Biomedical optics express* 5.8 (2014), pp. 2635–2647.

[62] J.S. Orcutt et al. "An Open Foundry Platform for High-Performance Electronic-Photonic Integration". In: *Opt. Express* 20 (2012), pp. 12222–12232.

[63] Tao Ling, Sung-Liang Chen, and L Jay Guo. "Fabrication and characterization of high Q polymer micro-ring resonator and its application as a sensitive ultrasonic detector". In: *Optics express* 19.2 (2011), pp. 861–869.

[64] S-L Chen et al. "Polymer microring resonators for high-sensitivity and wideband photoacoustic imaging". In: *IEEE transactions on ultrasonics, ferroelectrics, and frequency control* 56.11 (2009), pp. 2482–2491.

[65] SM Leinders et al. "A sensitive optical micro-machined ultrasound sensor (OMUS) based on a silicon photonic ring resonator on an acoustical membrane". In: *Scientific reports* 5 (2015), p. 14328.

[66] Cheng Zhang et al. "Review of imprinted polymer microrings as ultrasound detectors: Design, fabrication, and characterization". In: *IEEE Sensors Journal* 15.6 (2015), pp. 3241–3248.

[67] Lihong V Wang and Song Hu. "Photoacoustic tomography: in vivo imaging from organelles to organs". In: *science* 335.6075 (2012), pp. 1458–1462.

[68] Adam Maxwell et al. "Polymer microring resonators for high-frequency ultrasound detection and imaging". In: *IEEE Journal of Selected Topics in Quantum Electronics* 14.1 (2008), pp. 191–197.

[69] Wim Bogaerts et al. "Silicon microring resonators". In: *Laser & Photonics Reviews* 6.1 (2012), pp. 47–73.

[70] Chen Sun et al. "A 45 nm CMOS-SOI monolithic photonics platform with bit-statistics-based resonant microring thermal tuning". In: *IEEE Journal of Solid-State Circuits* 51.4 (2016), pp. 893–907.

[71] Vladimir Stojanović et al. "Monolithic silicon-photonic platforms in state-of-the-art CMOS SOI processes". In: *Optics express* 26.10 (2018), pp. 13106–13121.

[72] *BPG github repo webpage*. `https://github.com/BerkeleyPhotonicsGenerator`. Accessed: 2021-03-02.

[73] Chao Chen et al. "A prototype PZT matrix transducer with low-power integrated receive ASIC for 3-D transesophageal echocardiography". In: *IEEE transactions on ultrasonics, ferroelectrics, and frequency control* 63.1 (2015), pp. 47–59.

[74] Bao-Yu Hsieh et al. "All-optical scanhead for ultrasound and photoacoustic imaging—Imaging mode switching by dichroic filtering". In: *Photoacoustics* 2.1 (2014), pp. 39–46.

[75] Heming Wei and Sridhar Krishnaswamy. "Polymer micro-ring resonator integrated with a fiber ring laser for ultrasound detection". In: *Optics letters* 42.13 (2017), pp. 2655–2658.

[76] ChengMei Zhang and ChaoYing Zhao. "Sensitive label-free and compact ultrasonic sensor based on double silicon-on-insulator slot micro-ring resonators". In: *Optik* 178 (2019), pp. 1029–1034.

[77] Amnon Yariv. "Universal relations for coupling of optical power between microresonators and dielectric waveguides". In: *Electronics letters* 36.4 (2000), pp. 321–322.

[78] Dominik G Rabus. *Integrated ring resonators*. Springer, 2007.

[79] M Sumetsky. "Optimization of optical ring resonator devices for sensing applications". In: *Optics letters* 32.17 (2007), pp. 2577–2579.

[80] Lukas Chrostowski and Michael Hochberg. *Silicon photonics design: from devices to systems*. Cambridge University Press, 2015.

[81] Paul C Beard, Frederic Perennes, and Tim N Mills. "Transduction mechanisms of the Fabry-Perot polymer film sensing concept for wideband ultrasound detection". In: *ieee transactions on ultrasonics, ferroelectrics, and frequency control* 46.6 (1999), pp. 1575–1582.

[82] J Capilla et al. "Characterization of amorphous tantalum oxide for insulating acoustic mirrors". In: *2011 Joint Conference of the IEEE International Frequency Control and the European Frequency and Time Forum (FCS) Proceedings*. IEEE. 2011, pp. 1–6.

[83] Cheng Zhang et al. "Ultrabroad bandwidth and highly sensitive optical ultrasonic detector for photoacoustic imaging". In: *Acs Photonics* 1.11 (2014), pp. 1093–1098.

[84] Arthur W Leissa. *Vibration of plates*. Vol. 160. Scientific and Technical Information Division, National Aeronautics and ..., 1969.

[85] Stephen Timoshenko and Sergius Woinowsky-Krieger. "Theory of plates and shells". In: (1959).

[86] Chin-Lin Chen. *Foundations for guided-wave optics*. John Wiley & Sons, 2006.

[87] D Donadio, M Bernasconi, and F Tassone. "Photoelasticity of crystalline and amorphous silica from first principles". In: *Physical Review B* 68.13 (2003), p. 134202.

[88] Chung-Yen Chao et al. "High-frequency ultrasound sensors using polymer microring resonators". In: *ieee transactions on ultrasonics, ferroelectrics, and frequency control* 54.5 (2007), pp. 957–965.

[89] Chen Sun et al. "Single-chip microprocessor that communicates directly using light". In: *Nature* 528.7583 (2015), pp. 534–538.

[90] M. T. Wade and M. A. Popović. "Efficient wavelength multiplexers based on asymmetric response filters". In: *Opt. Express* 21 (2013), pp. 10903–10916.

[91] Sidney Buchbinder et al. "BPG: An Open-Source, Technology Agnostic Framework for Generator-Based Photonic Design, Layout, and Simulation". In: *2021 International Conference On Computer Aided Design (ICCAD)*. IEEE. Submitted.

[92] Minghua Xu and Lihong V Wang. "Photoacoustic imaging in biomedicine". In: *Review of scientific instruments* 77.4 (2006), p. 041101.

[93] Peter R Hoskins, Kevin Martin, and Abigail Thrush. *Diagnostic ultrasound: physics and equipment*. CRC Press, 2019.

[94] Sajjad Moazeni et al. "A 40-Gb/s PAM-4 transmitter based on a ring-resonator optical DAC in 45-nm SOI CMOS". In: *IEEE Journal of Solid-State Circuits* 52.12 (2017), pp. 3503–3516.

[95] Nandish Mehta, Sidney Buchbinder, and Vladimir Stojanović. "Design and Characterization of Monolithic Microring Resonator based Photodetector in 45nm SOI CMOS". In: *ESSDERC 2019-49th European Solid-State Device Research Conference (ESSDERC)*. IEEE. 2019, pp. 206–209.

[96] M Wade et al. "An error-free 1 Tbps WDM optical I/O chiplet and multi-wavelength multi-port laser". In: *Optical Fiber Communication Conference*. Optical Society of America. 2021, F3C–6.

[97] Yuechun Shi et al. "High channel count and high precision channel spacing multi-wavelength laser array for future PICs". In: *Scientific reports* 4.1 (2014), pp. 1–6.

[98] Tae Joon Seok et al. "High density optical packaging of high radix silicon photonic switches". In: *Optical Fiber Communication Conference*. Optical Society of America. 2017, Th5D–7.

[99] *Hitachi micro-coax cables datasheet*. `http://www.elimec.co.il/_Uploads/dbsAttachedFiles/HCA_Med.pdf`. Accessed: 2021-08-02.

[100] Sung Min Park and C Toumazou. "A packaged low-noise high-speed regulated cascode transimpedance amplifier using a 0.6 μm N-well CMOS technology". In: *Proceedings of the 26th European Solid-State Circuits Conference*. IEEE. 2000, pp. 431–434.

[101] Christian Kromer et al. "A low-power 20-GHz 52-dB/spl Omega/transimpedance amplifier in 80-nm CMOS". In: *IEEE Journal of Solid-State Circuits* 39.6 (2004), pp. 885–894.

[102] Behzad Razavi. "A 622 Mb/s 4.5 pA//spl radic/Hz CMOS transimpedance amplifier [for optical receiver front-end]". In: *2000 IEEE International Solid-State Circuits Conference. Digest of Technical Papers (Cat. No. 00CH37056)*. IEEE. 2000, pp. 162–163.

[103] Carmine Ciofi et al. "A new circuit topology for the realization of very low-noise wide-bandwidth transimpedance amplifier". In: *IEEE Transactions on Instrumentation and Measurement* 56.5 (2007), pp. 1626–1631.

[104] *BAG github repo webpage*. `https://github.com/ucb-art/BAG_framework`. Accessed: 2021-08-02.

[105] *J. Han. LAYGO Repository*. `http://github.com/ucb-art/laygo`. Accessed: 2018-11-02.

[106] Jaeduk Han et al. "LAYGO: A Template-and-Grid-Based Layout Generation Engine for Advanced CMOS Technologies". In: *IEEE Transactions on Circuits and Systems I: Regular Papers* 68.3 (2021), pp. 1012–1022.

[107] Erman Timurdogan et al. "An ultralow power athermal silicon modulator". In: *Nature communications* 5.1 (2014), pp. 1–11.

[108] Cheng Li et al. "Silicon photonic transceiver circuits with microring resonator bias-based wavelength stabilization in 65 nm CMOS". In: *IEEE journal of solid-state circuits* 49.6 (2014), pp. 1419–1436.

[109] Erman Timurdogan et al. "Automated wavelength recovery for microring resonators". In: *CLEO: Science and Innovations*. Optical Society of America. 2012, pp. CM2M–1.

[110] Hao Li et al. "A 25 Gb/s, 4.4 V-swing, AC-coupled ring modulator-based WDM transmitter with wavelength stabilization in 65 nm CMOS". In: *IEEE Journal of Solid-State Circuits* 50.12 (2015), pp. 3145–3159.

[111] Paul P Sotiriadis. "Theory of flying-adder frequency synthesizers—Part I: modeling, signals' periods and output average frequency". In: *IEEE Transactions on Circuits and Systems I: Regular Papers* 57.8 (2010), pp. 1935–1948.

[112] Jelena Notaros et al. "Ultra-efficient CMOS fiber-to-chip grating couplers". In: *2016 Optical Fiber Communications Conference and Exhibition (OFC)*. IEEE. 2016, pp. 1–3.

[113] Gonzalo Seco-Granados, Juan A Fernández-Rubio, and Carles Fernández-Prades. "ML estimator and hybrid beamformer for multipath and interference mitigation in GNSS receivers". In: *IEEE Transactions on Signal Processing* 53.3 (2005), pp. 1194–1208.

[114] Robert J Mailloux. *Phased array antenna handbook*. Artech house, 2017.

[115] Chao Chen et al. "A 0.91 mW/element pitch-matched front-end ASIC with integrated subarray beamforming ADC for miniature 3D ultrasound probes". In: *2018 IEEE International Solid-State Circuits Conference-(ISSCC)*. IEEE. 2018, pp. 186–188.

[116] Chao Chen et al. "A pitch-matched front-end ASIC with integrated subarray beamforming ADC for miniature 3-D ultrasound probes". In: *IEEE Journal of Solid-State Circuits* 53.11 (2018), pp. 3050–3064.

[117] Matthew Terrel, Michel JF Digonnet, and Shanhui Fan. "Ring-coupled Mach-Zehnder interferometer optimized for sensing". In: *Applied optics* 48.26 (2009), pp. 4874–4879.

[118] Christos Adamopoulos et al. "Electronic-Photonic Platform for Label-Free Biophotonic Sensing in Advanced Zero-Change CMOS-SOI Process". In: *CLEO: QELS Fundamental Science*. Optical Society of America. 2019, JW2A–81.

[119] Joseph C Salamone. *Polymeric Materials Encyclopedia, Twelve Volume Set*. CRC press, 1996.

[120] William D Nix. "Mechanical properties of thin films". In: *Metallurgical transactions A* 20.11 (1989), p. 2217.

[121] Minghua Xu and Lihong V Wang. "Photoacoustic imaging in biomedicine". In: *Review of scientific instruments* 77.4 (2006), p. 041101.

[122] Lihong V Wang. *Photoacoustic imaging and spectroscopy*. CRC press, 2017.

[123] Paul Beard. "Biomedical photoacoustic imaging". In: *Interface focus* 1.4 (2011), pp. 602–631.

[124] Song Hu and Lihong V Wang. "Photoacoustic imaging and characterization of the microvasculature". In: *Journal of biomedical optics* 15.1 (2010), p. 011101.

[125] Srivalleesha Mallidi, Geoffrey P Luke, and Stanislav Emelianov. "Photoacoustic imaging in cancer detection, diagnosis, and treatment guidance". In: *Trends in biotechnology* 29.5 (2011), pp. 213–221.

[126] Bao-Yu Hsieh et al. "A laser ultrasound transducer using carbon nanofibers polydimethylsiloxane composite thin film". In: *Applied Physics Letters* 106.2 (2015), p. 021902.

[127] Elena Biagi, Fabrizio Margheri, and David Menichelli. "Efficient laser-ultrasound generation by using heavily absorbing films as targets". In: *ieee transactions on ultrasonics, ferroelectrics, and frequency control* 48.6 (2001), pp. 1669–1680.

[128] Hyoung Won Baac et al. "Carbon-nanotube optoacoustic lens for focused ultrasound generation and high-precision targeted therapy". In: *Scientific reports* 2.1 (2012), pp. 1–8.